

Proton Modulation of Residue E1784 and its Regulation of Fast Inactivation

**by
Colin Peters**

B.Sc., Simon Fraser University, 2013

Thesis Submitted in Partial Fulfillment of the
Requirements for the Degree of
Doctor of Philosophy

in the
Department of Biomedical Physiology and Kinesiology
Faculty of Science

© Colin Peters 2018
SIMON FRASER UNIVERSITY
Spring 2018

Copyright in this work rests with the author. Please ensure that any reproduction or re-use is done in accordance with the relevant national copyright legislation.

Approval

Name: Colin Peters
Degree: Doctor of Philosophy
Title: Proton Modulation of Residue E1784 and its Regulation of Fast Inactivation

Examining Committee: **Chair:** William Cupples
Professor

Peter Ruben
Senior Supervisor
Professor

Damon Poburko
Supervisor
Assistant Professor

Thomas Claydon
Supervisor
Associate Professor

Nadine Wicks
Internal Examiner
Lecturer

Colleen E. Clancy
External Examiner
Professor
Department of Pharmacology-Medicine
University of California - Davis

Date Defended/Approved: December 14, 2017

Ethics Statement

The author, whose name appears on the title page of this work, has obtained, for the research described in this work, either:

- a. human research ethics approval from the Simon Fraser University Office of Research Ethics

or

- b. advance approval of the animal care protocol from the University Animal Care Committee of Simon Fraser University

or has conducted the research

- c. as a co-investigator, collaborator, or research assistant in a research project approved in advance.

A copy of the approval letter has been filed with the Theses Office of the University Library at the time of submission of this thesis or project.

The original application for approval and letter of approval are filed with the relevant offices. Inquiries may be directed to those authorities.

Simon Fraser University Library
Burnaby, British Columbia, Canada

Update Spring 2016

Abstract

The cardiac voltage-gated sodium channel, Nav1.5, is responsible for the phase 0 depolarization of the ventricular cardiomyocyte action potential. Nav1.5 activates in response to depolarization, passes a transient inward sodium current, and then inactivates within milliseconds. Mutants in Nav1.5 that decrease the peak sodium transient cause Brugada syndrome and those that increase the fraction of channels that fail to inactivate cause long QT syndrome type 3 (LQT3). Some mutants both decrease the peak current and increase the non-inactivating current, leading to an overlapping phenotype of Brugada syndrome and LQT3. Of these mutants, E1784K in the proximal C-terminus is the most prevalent. The E1784K mutant alters channel opening, fast inactivation, and slow inactivation, but the exact mechanism by which it does so is unknown. Nor is it known why patients may experience normal heart function for many years before appearance of an arrhythmia.

In these studies, the cut-open voltage-clamp technique is used to record Nav1.5 currents and voltage-sensor fluorescence from residue 1784 mutants expressed in *Xenopus laevis* oocytes. Experiments are conducted with extracellular pH between 7.4 and 4.0. Based on these data, a novel model of the voltage-gated sodium channel is constructed. The following data show that: (1) the E1784K mutant-dependent loss-of-function and gain-of-function effects are preferentially exacerbated by decreases in extracellular pH; (2) the E1784K mutant disrupts channel fast inactivation; (3) the mutant-dependent effects on channel conductance and the preferential effects of decreasing extracellular pH are due to altered channel fast inactivation; (4) Non-inactivating sodium current is conferred by a positive charge at residue 1784. These data provide mechanistic insight into how a single mutant may cause multiple disease phenotypes, paving the way for future therapeutic research.

Keywords: Sodium channel; Long QT Syndrome; Brugada Syndrome; Acidaemia; Inactivation

To my friends and family who helped me when I was at my weakest.

Acknowledgements

Thank you first and foremost to my family and friends for your love, friendship, and support. Thank you to Dr. Tom Claydon, not only for your support and guidance, but also for teaching me what “real cheddar cheese” is. Thank you to Dr. Damon Poburko, for your input on my projects and brightening the lab with your whistling. Thank you to Mena Abdelsayed and Reza Ghovanloo for many trips to Club Ilia. Thank you to Madeline Angus for all the ridiculous things you did that made me smile. Thank you Dr. Yury Vilin and Dr. Stan Sokolov, two post-doctoral researchers who taught me much about patch-clamp and life.

Thank you to my 3 brilliant undergraduates, Kristina Collins, Alec Yu, and Olivia Poirier. Kristina, you taught me how to work with a new student. Alec, you taught me that there is always someone better than me, his name is Alec Yu. Olivia, you taught me that a person need not be overly serious to also be brilliant. Having the opportunity to work with wonderful students like you is the part of research I love most.

Thank you to David Jones for teaching me how to be a grad student. From you I learned how to voltage-clamp oocytes and how to swing on a rope over an ice-cold waterfall. Thank you to my close friends Vera-Ellen Lucci and Christina Hull. You kept me sane throughout grad school.

A special thanks to my mentor and supervisor, Peter. Being a member of the Ruben lab has shaped the past 8 years of my life. You helped me find my true passion for research and I don't think words can express my gratitude.

I'll leave off by saying that the best nights of grad school were the late nights. The nights where I held David's infant son so Dave could finish his experiments. The nights Alec and I stayed late to collect data. The nights with Reza that were spent half in the patch-clamp room and half at the SFU pub. The night in Philadelphia where Peter and I followed up a Reel Big Fish concert with a beer at the Trestle Inn. And even the nights where it was just me and an electrophysiology rig. Looking back, I cannot think of a way I would rather have spent those evenings.

Table of Contents

Approval	ii
Ethics Statement.....	iii
Abstract.....	iv
Dedication.....	v
Acknowledgements.....	vi
Table of Contents.....	vii
List of Tables	x
List of Figures.....	xi
List of Acronyms	xiii
Glossary	xiv
Preface.....	xv
Chapter 1. Introduction to Sodium Channels	1
1.1. Sodium Channel Diversity.....	2
1.2. Structure and Function of Sodium Channels	3
1.2.1. Sodium Channel Conductance.....	5
1.2.2. Sodium Channel Fast Inactivation.....	9
1.2.3. Sodium Channel Slow Inactivation	13
1.2.4. Modulation of Sodium Gating by Accessory Proteins and Molecules.....	14
1.3. Sodium Channels and Disease.....	16
1.3.1. The Cardiac Action Potential	17
1.3.2. Long QT Syndrome	20
1.3.3. Brugada Syndrome	21
1.4. Environmental Regulators of Electrical Signalling	26
1.4.1. pH and Sudden Cardiac Death.....	26
1.4.2. Proton Modulation of Cardiac Channel Gating.....	27
1.5. The E1784K mutant.....	29
1.6. Conclusion	33
Chapter 2. Proton Modulation of E1784K Ionic and Gating Currents	35
2.1. Introduction.....	35
2.2. Methods	37
2.2.1. DNA Constructs	37
2.2.2. Oocyte preparation	37
2.2.3. Data acquisition	38
2.2.4. Protocols.....	39
2.2.5. Data analysis.....	42
2.3. Results.....	42
2.3.1. Intracellular pH does not Change Along with Extracellular pH in Oocytes ..	43

2.3.2.	E1784K Depolarizes the Conductance-Voltage Relationship and Hyperpolarizes Gating Charge Activation	44
2.3.3.	E1784K Hyperpolarizes and Accelerates Fast Inactivation	47
2.3.4.	E1784K Increases Non-Inactivating Current	49
2.3.5.	E1784K Depolarizes Voltage-Sensor Deactivation	51
2.3.6.	E1784K does not Impact Slow Inactivation Voltage-Dependence	52
2.3.7.	E1784K Accelerates Slow Inactivation Onset and Recovery	52
2.4.	Discussion.....	54
Chapter 3. Chapter 3: E1784K Regulates Channel Fast Inactivation		59
3.1.	Introduction.....	59
3.2.	Materials and Methods:	62
3.2.1.	Modeling.....	62
3.2.2.	Experimental.....	65
3.2.3.	Statistical Analysis	67
3.3.	Results.....	67
3.3.1.	The Peters-Ruben Model Accurately Recapitulates Experimental Gating and Ionic Currents	68
3.3.2.	The E1784K Mutant Can be Modelled with Shifts to Fast Inactivation	70
3.3.3.	DIVS4 movement is shifted to more hyperpolarized potentials in E1784K ..	72
3.3.4.	Removal of FI removes E1784K-Dependent shifts in conductance.....	74
3.4.	Discussion.....	75
3.4.1.	The Peters-Ruben Model.....	76
3.4.2.	The E1784K Mutant Primarily Modifies Fast Inactivation.....	79
3.4.3.	Advantages of the Peters-Ruben Model	80
3.4.4.	Limitations of the Peters-Ruben Model.....	81
3.5.	Conclusion	82
Chapter 4. Residue 1784 Mutants Disrupt Fast Inactivation Through Two Separate Mechanisms		83
4.1.	Introduction.....	83
4.2.	Methods	85
4.2.1.	DNA Constructs	85
4.2.2.	Oocyte Preparation	85
4.2.3.	Data Acquisition and Protocols	85
4.2.4.	Data Analysis.....	85
4.2.5.	Homology Models	86
4.3.	Results.....	86
4.3.1.	Conductance	86
4.3.2.	Fast Inactivation	87
4.3.3.	Gating Charge Activation and Deactivation.....	91
4.3.4.	Non-inactivating Current.....	93

4.3.5.	Correlations	94
4.4.	Discussion.....	96
4.4.1.	E1784 Mutants Destabilize Two Fast Inactivation Interactions.....	96
4.4.2.	Rapid Fast Inactivation Increases Proton Block of Conductance.....	98
4.4.3.	E1784 May Interact with K1493 in the DIII-DIV linker.....	101
4.4.4.	Conclusion.....	102
Chapter 5.	Conclusion	103
5.1.	Interactions of Residue 1784 in NaV1.5.....	103
5.2.	Role of Protons in E1784K Arrhythmia	108
5.3.	Future Directions	109
5.4.	Limitations	111
5.5.	Clinical Significance.....	114
5.6.	Concluding Remarks.....	115
References.....		116
Appendix A.	Data for Chapter 2.....	146
Appendix B.	Peters-Ruben Model Parameters.....	154
Appendix C.	Data for Chapter 3.....	155
Appendix D.	Data for Chapter 4.....	157

List of Tables

Table 1.1.	Sodium Channel Isoforms.....	1
------------	------------------------------	---

List of Figures

Figure 1.1.	Structure of Eukaryotic Voltage-Gated Sodium Channels	4
Figure 1.2.	Voltage-sensing Domain of NavPaS	6
Figure 1.3.	The Selectivity Filter of Eukaryotic Voltage-Gated Sodium Channels.....	8
Figure 1.4.	C-Terminal Interactions with the DIII-DIV linker	12
Figure 1.5	The Ventricular Cardiomyocyte Action Potential and its Underlying Currents.....	19
Figure 1.6.	The Repolarization Hypothesis for Brugada Syndrome	23
Figure 1.7.	The Depolarization Hypothesis for Brugada Syndrome.....	24
Figure 1.8.	Maximal Conductance in the E1784K Mutant is Preferentially Blocked by Protons	31
Figure 1.9.	Protons Preferentially Depolarize the Conductance Curve in E1784K Nav1.5	32
Figure 1.10.	Lowered Extracellular pH Preferentially Increases Non-Inactivating Currents in E1784K Nav1.5.....	33
Figure 2.1.	Intracellular pH is not Decreased by Decreases in Extracellular pH.....	43
Figure 2.2.	The E1784K Mutant Depolarizes the Conductance-Voltage Relationship and Hyperpolarizes Gating Charge Activation	44
Figure 2.3.	The E1784K Mutant does not Alter the Rate of Outward Gating Charge Movement at Depolarized Membrane Potentials.....	46
Figure 2.4.	The E1784K Mutant Hyperpolarizes the Voltage-Dependence of Fast Inactivation	48
Figure 2.5.	The E1784K Mutant Increases Non-Inactivating Current and Depolarizes the Voltage-Dependence of Gating Charge Deactivation.....	50
Figure 2.6.	The E1784K Mutant Accelerates a Slow Time Component of Slow Inactivation	53
Figure 3.1.	The Peters-Ruben Model of Voltage-Gated Sodium Channel Gating.....	61
Figure 3.2.	The Peters-Ruben Model Accurately Simulates Sodium Channel Ionic and Gating Currents.....	68
Figure 3.3.	The Peters-Ruben Model Accurately Simulates Channel Activation, Fast Inactivation, and Slow Inactivation	69
Figure 3.4.	The Peters-Ruben Model Accurately Simulates E1784K Nav1.5 at pH 7.4 and pH 6.0.....	71
Figure 3.5.	The Movement of DIVS4 is Hyperpolarized by the E1784K Mutant.....	73
Figure 3.6.	The E1784K Mutant Depolarizes the Conductance-Voltage Relationship Through Altered Fast Inactivation	75
Figure 3.7.	Limitations of the Peters-Ruben Model.....	77

Figure 4.1.	Mutants at Residue 1784 in Nav1.5 Alter the Voltage-dependence of Conductance and Proton Block of Maximal Conductance	88
Figure 4.2.	Mutants at Residue 1784 in Nav1.5 Alter the Rates and Voltage-Dependence of Fast Inactivation.....	89
Figure 4.3.	Mutants at Residue 1784 Alter Gating Current Voltage-Dependence.....	92
Figure 4.4.	Positively Charged Mutants at Residue 1784 Increase Non-Inactivating Current	94
Figure 4.5.	The Voltage-Dependence of Gating Charge Movement Correlates to the Voltage-Dependence of Fast Inactivation but not Conductance.....	95
Figure 4.6	A Homology model of Nav1.5 Suggests E1784 Associates With K1493 in the DIII-DIV Linker.....	100
Figure 5.1.	A Homology Model of the Nav1.5 C-Terminus Interacting with the DIVS4-S5 linker	104
Figure 5.2.	Predicted Interactions Between the C-Terminus and the DIII-DIV Linker.	106
Figure 5.3	Non-Inactivating Current of the K1493E/E1784K Nav1.5 Mutant.....	111
Figure 5.4.	Hyperpolarizing DIIS4 Movement in the Peters-Ruben Model Improves the Fit to Experimental Data.	113

List of Acronyms

CNS	central nervous system
DIS1	domain I segment 1
ECG	electrocardiogram
FV	fluorescence-voltage
GV	conductance-voltage
IgOn	on (outward) gating charge
IgOff	off (inward) gating charge
LQT3	long QT syndrome type 3
PNS	parasympathetic nervous system
QV	charge-voltage
TTX	tetrodotoxin

Glossary

Action Potential	An all-or-none electrical signal characterized by a depolarization of the cell membrane followed by repolarization
Activation	The outward motion of the channel voltage-sensors following depolarization of the membrane
Deactivation	The inward motion of the channel voltage-sensors following repolarization of the membrane
Depolarization	A change in membrane potential towards 0 mV, often used to describe any change to more positive membrane potentials
Gating Current	Currents caused by the movement of charged residues within the electrical field of the membrane
Inactivation	The process of current cessation at depolarized membrane potentials. It is distinct from deactivation.
Ionic Current	Currents caused by the flow of ions across the membrane through the channel pore
Nav1.5	The voltage-gated sodium channel most highly expressed in ventricular tissue
Non-inactivating Current	Current that does not fast inactivate and continues to flow after the initial peak sodium transient
Repolarization	Changes in the membrane potential towards the resting membrane potential. Often used to describe any change to more negative membrane potentials

Preface

Much of the work presented here has been published previously. Chapter 1 represents 100 % my own work and includes excerpts and adaptations of previous work (1,2). Chapters 2 and 3 are approximately 90 % my own work and much of these two chapters has been published previously (3). Chapter 4 represents 100 % my own work and is currently a manuscript in progress. Chapter 5 represents 100 % my own work.

Chapter 1. Introduction to Sodium Channels

The voltage-gated sodium channel (Nav) family consists of 10 members, Nav1.1-1.9 and Nav2.1, encoded by the genes SCN1A-SCN11A (Table 1.1) (4). Voltage-gated sodium channels are found in the nervous system, heart, and skeletal muscle fibers, where they allow movement of sodium across the cell membrane. The inward movement of sodium, is responsible for the initial depolarization of the action potential waveform in each of these tissues. This sodium current is transient, ceasing within milliseconds as the channels undergo a process termed inactivation (5). Genetic mutations in the genes encoding voltage-gated sodium channels can result in channels with altered opening and inactivation or render the channel non-functional. Similar effects are exerted by drugs which target sodium channels, altering channel gating or blocking the channel. Altered sodium channel function underlies potentially fatal electrical diseases including epilepsy disorders, paroxysmal pain, paralysis, myotonia, long QT syndrome type 3 (LQT3) and Brugada syndrome.

Table 1.1. Sodium Channel Isoforms

Gene	Chromosome	Protein
SCN1A	2q24.3	Nav1.1
SCN2A	2q24.3	Nav1.2
SCN3A	2q24.3	Nav1.3
SCN4A	17q23.3	Nav1.4
SCN5A	3p22.2	Nav1.5
SCN6A/SCN7A	2q24.3	Nav2.1
SCN8A	12q13.13	Nav1.6
SCN9A	2q24.3	Nav1.7
SCN10A	3p22.2	Nav1.8
SCN11A	3p22.2	Nav1.9

Sodium channel gene and protein names as well as chromosomal location of the gene.

From the original quantification of the sodium current, which won Sir Alan Hodgkin, Sir Bernard Katz, and Sir Andrew Huxley the Nobel prize, to the recent crystal structures of eukaryotic sodium channels, our understanding of the voltage-gated sodium channel has grown (5–10). Equipped with Bernstein's theory of action potential generation and results from Cole and Curtis, Hodgkin, Huxley, and Katz recorded action

potentials and currents from *Loligo forbesii* and provided a mathematical model of how the sodium and potassium currents alter the membrane potential across an axon (5–8,11–14). Hodgkin and Huxley proposed that sodium currents and potassium currents each have four gates. For the sodium current, three of these gates control channel activation and one controls inactivation, while in the potassium current all four gates control activation. Work by Clay Armstrong and Francisco Benzanilla later measured the gating currents that precede channel opening (15,16). It is now understood that these gating currents are due to the movement of channel segments containing positively charged lysine and arginine residues. In response to changes in membrane potential these segments move across the membrane and, in doing so, lead to opening, closing, and inactivation of the channel (17–20). The four gates predicted by Hodgkin and Huxley correspond to these four voltage-sensors, of which the first three control channel activation and the voltage-sensor in domain four controls the fast inactivation.

The following chapters review the current understanding of the structure and function of sodium channels, particularly the cardiac Nav1.5. The role of cardiac sodium channel mutants in disease and how changes to the body's internal environment impact their pathophysiology is discussed. Finally, the following chapters present data on the role of the E1784K mutant in altered gating of Nav1.5.

1.1. Sodium Channel Diversity

One classification of voltage-gated sodium channel isoforms is based on sensitivity to the sodium channel specific blocker tetrodotoxin, (TTX). The TTX-sensitive channels, Nav1.1-1.4, Nav1.6, and Nav1.7, are blocked by nanomolar concentrations of TTX, while the TTX-resistant channels, Nav1.5, Nav1.8, and Nav1.9, are blocked by millimolar concentrations (4). When residue C373 in the first domain of Nav1.5 is mutated to phenylalanine or tyrosine, the corresponding amino acid in Nav1.2 and Nav1.4, respectively, TTX-sensitivity is restored (21–24).

A simple, but not all encompassing, classification of sodium channel based on location is the split between central nervous system (CNS), peripheral nervous system

(PNS), skeletal muscle, and cardiac expression. The sodium channels expressed most highly in the CNS are Nav1.1-1.3, and Nav1.6. Dorsal root ganglion neurons and other peripheral neurons express Nav1.6-1.9. Nav1.4 is the skeletal muscle sodium channel and Nav1.5 is the cardiac sodium channel (4). This is an over-simplification. mRNA transcripts from Nav1.1 through Nav1.8 have been identified in the heart, albeit in some cases at a low level (25,26). Nav1.5 represents only 77 % of the total sodium channel protein levels in mouse ventricular myocytes and show lower levels of staining in T-tubules than do Nav1.1 and Nav1.3 (27,28). Nav1.8 may play a particularly important role in regulating cardiac conduction. SCN10A, the gene which encodes Nav1.8, and SCN5A, the gene which encodes Nav1.5, are located in the same region of chromosome 3. Not only is Nav1.8 expressed in cardiac neurons, but mutations in SCN10A can downregulate expression of Nav1.5 leading to decreased sodium currents (26,29–31). Sodium channel expression patterns are also dependent on other factors, including injury. Following damage to the nervous system, Nav1.3 and Nav1.7 are upregulated, which may play a role in neuropathic pain following injury (32,33). Following heart failure Nav1.1 and Nav1.3 are upregulated in the sino-atrial node (34). These small changes may play important roles in clinical settings as sodium channel isoforms show differences in activation, inactivation, and fraction of non-inactivating sodium current (4).

1.2. Structure and Function of Sodium Channels

Although the voltage-gated sodium channel isoforms differ in location, drug sensitivity, and gating, they share a common structure. Voltage-gated sodium channels are formed by 24 alpha-helical, transmembrane segments arranged in four domains (DI-DIV) (4,35) (Figure 1.1A). Unlike potassium channels which are composed of four identical subunits, the four domains of voltage-gated sodium channels are encoded by a single mRNA transcript, approximately 2,000 amino acids in length (36). Therefore, the sequences of the 4 domains in sodium channels are not identical, nor are the intracellular segments connecting the domains.

Each of the four domains of the voltage-gated sodium channel consists of a voltage-sensing domain formed by the first four transmembrane segments (S1-S4) and a

pore domain consisting of S5, S6, and the extracellular linker between these two segments (37,38). The S4s contain positively charged arginine and lysine residues spaced approximately every 3 amino acids. The movement of these charges across the electrical field of the membrane can be measured as a small current (39–42). As the movement of the S4s controls the activation and inactivation of the sodium channel, this current is called a gating current.

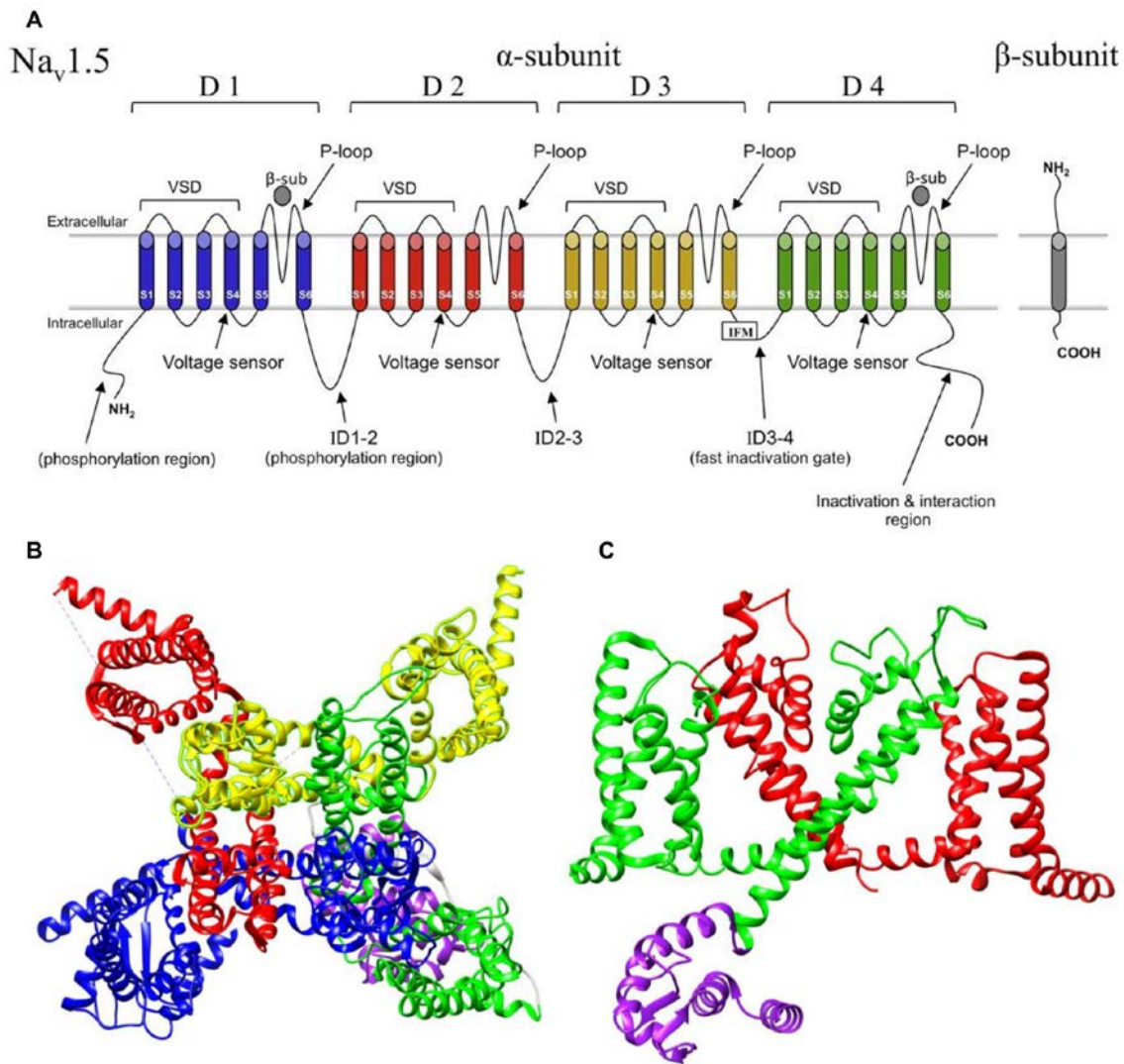


Figure 1.1. Structure of Eukaryotic Voltage-Gated Sodium Channels

A: Primary structure of the mammalian cardiac voltage-gated sodium channel. The α -subunit is formed by a single transcript with 24 alpha-helical transmembrane segments split into 4 domains. The α -subunit associates with 1 or more β -subunits. From Detta *et al.*, 2015 (CC BY-NC-ND 4.0) (43). **B:** NavPaS structure viewed from the extracellular side, colored by domain as in **A**. The C-terminus is colored purple. The voltage-sensors are clustered around the central pore domain. **C:** NavPaS structure viewed from the side with D1 and DIII removed for clarity (PDB ID: 5X0M) (9). Molecular graphics and analyses were

performed with the UCSF Chimera package. Chimera is developed by the Resource for Biocomputing, Visualization, and Informatics at the University of California, San Francisco (supported by NIGMS P41-GM103311) (44)

NMR and crystal structures of the C-terminus and DIII-DIV linker segment of human sodium channels are available; however, the full structure of a mammalian sodium channel has not been solved (45–47). Prior to 2017, the only full voltage-gated sodium channel structures were of homotetrameric sodium channels from bacteria and a chimera of the outer Nav1.7 voltage-sensor and the *Arcobacter butzleri* sodium channel (38,48,49). The first eukaryotic voltage-gated sodium channel structures were released earlier this year and are from the American cockroach, *Periplaneta Americana* (NavPaS), and the electric eel, *Electrophorus electricus* (Figure 1.1B) (9,10).

1.2.1. Sodium Channel Conductance

Activation of the voltage-sensors and opening of the sodium channel pore during depolarization allows for the flow of sodium through the channel pore. Upon depolarization, the S4 transmembrane segments move toward the extracellular surface (17,41). During this movement, the positive gating charges form paired interactions with negatively charged residues in S1-S3, stabilizing translocation of gating charges across the membrane (Figure 1.2) (50). The voltage-sensing domains are physically coupled to the pore domains by the S4-S5 linkers. The outward movement of the voltage-sensors exerts a torque on the S4-S5 linker that in turn causes rearrangement and opening of the pore (51,52). Upon repolarization, the pore closes and the S4 segments return to their resting positions; this process is called deactivation. The outward movements of the DIS4 (S4 segment of domain I), DIIS4, and DIIS4 cause opening of the sodium channel pore, seemingly confirming the existence of 3 activation gates suggested by Hodgkin and Huxley (18,50,53). In contrast, much of the movement of DIVS4 occurs after channel opening suggesting less involvement in channel activation (20,53).

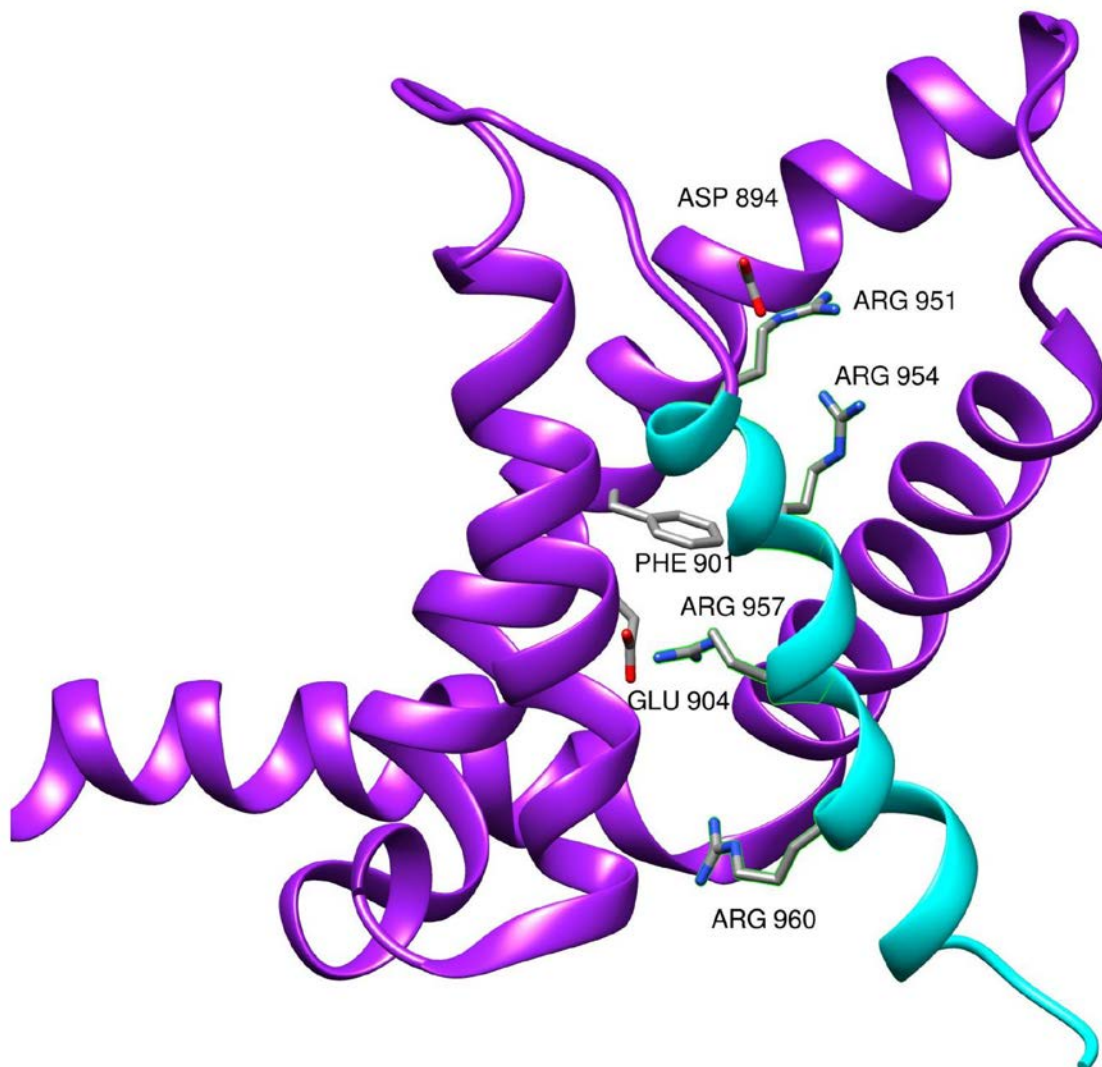


Figure 1.2. Voltage-sensing Domain of NavPaS

A voltage-sensing domain from the NavPaS structure shown from the side. The S4 voltage-sensor is colored cyan. Atoms for the gating charges R2, R3, R4, and R5, basic residues on S2, and the highly conserved phenylalanine charge-transfer center are shown (PDB ID: 5X0M) (9).

Pore opening is followed by hydration of the channel pore, after which sodium is selectively conducted through the channel (54). Sodium channels are highly selective for sodium entry into the cell with a potassium permeability to sodium permeability ratio of less than 0.10 (55–57). The selectivity filter in eukaryotic sodium channels is formed by the asymmetric DEKA ring: D372 in domain I, E898 in domain II, K1419 in domain III, and A1710 in domain IV (Figure 1.3) (57,58). K1419 is required to maintain sodium selectivity. Even the charge conserving K1419R mutant abolishes sodium selectivity and

allows potassium permeation (56). Conversely, if the DEKA ring in mammalian channels is mutated to EEEE the sodium channel can be converted into a calcium selective channel (58). Lipkind and Fozzard proposed a model of the mammalian DEKA selectivity where K1419 forms interactions with D372 and E898 that occlude the selectivity filter. Being a stronger Lewis acid than potassium, sodium is capable of displacing this interaction and permeating through the selectivity filter (57). The rate of sodium channel permeation is further determined by the outer charged ring of carboxylate residues E375, E901, D1423, and D1714. Although these outer charged ring residues do not play a large role in determining sodium channel selectivity, mutating E375, E901, and D1714 drastically decrease single channel conductance (59).

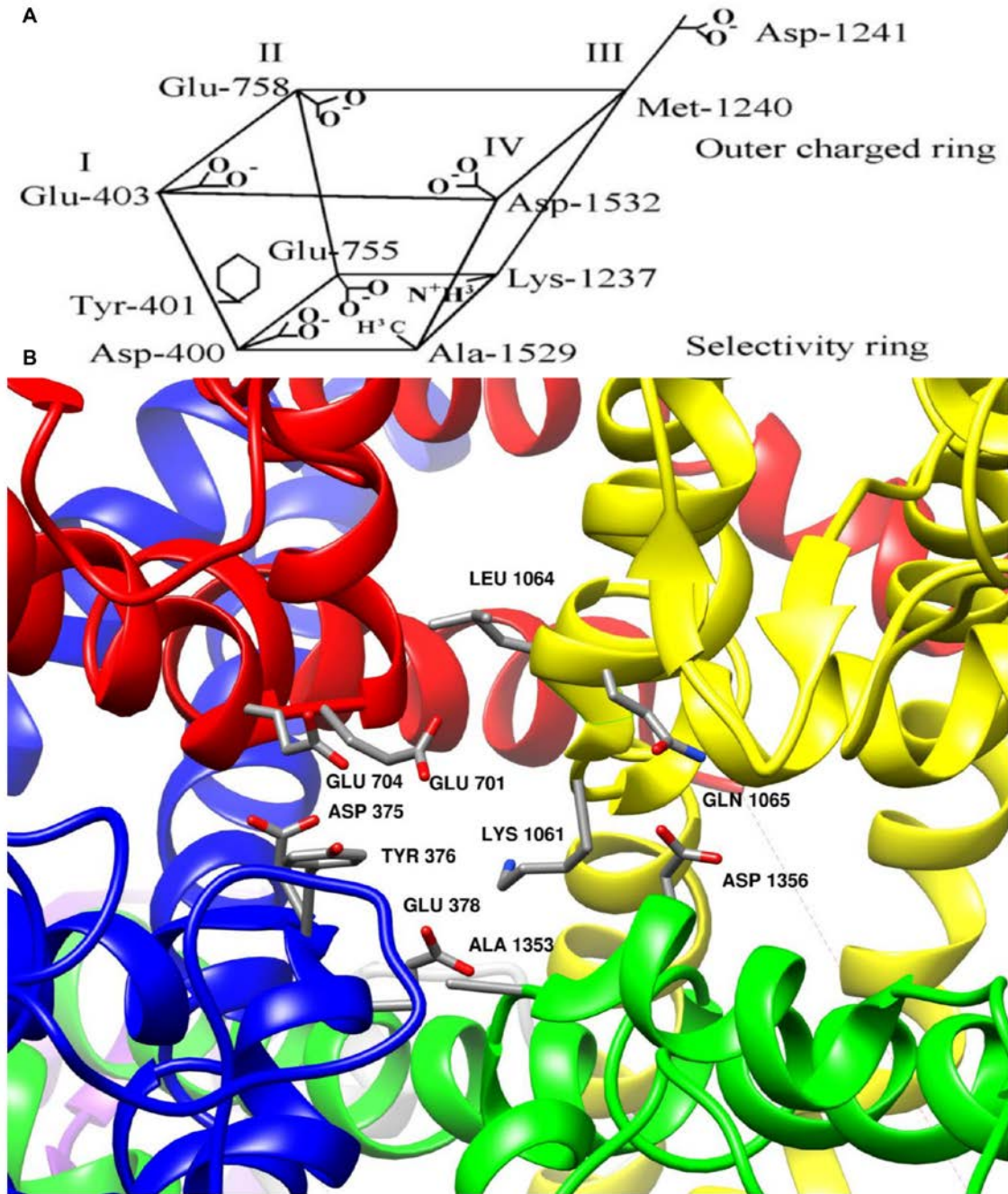


Figure 1.3. The Selectivity Filter of Eukaryotic Voltage-Gated Sodium Channels

A: Schematic of the selectivity filter and outer charged ring of Nav_v1.4. The lower DEKA ring forms a selectivity filter and the upper EEDD forms the outer charged ring. Y401 is critical for block of sodium channels by tetrodotoxin. From Fozzard and Lipkind, 2010 (CC BY 3.0) (60). **B:** Structure of the Nav_vPaS selectivity filter and outer charged ring. Residues homologous to those in Nav_v1.4 are labelled (PDB ID: 5X0M) (9).

1.2.2. Sodium Channel Fast Inactivation

Following activation, voltage-gated sodium channels remain in a conductive state for only a few milliseconds. The cessation of current is due not to channel deactivation, but rather a process termed fast inactivation (5). During fast inactivation, an intracellular particle binds and occludes the channel pore. The fast inactivation particle is formed by four residues in the linker between domains three and four of the sodium channel: I1485, F1486, M1487, and T1488. Removal of the IFMT motif removes channel fast inactivation (61,62). When the cytosol is depolarized, this linker binds to residues on the intracellular side of domains III and IV, either occluding the channel pore directly or causing rearrangement sufficient to close the pore (9,63,64). The particle, therefore, acts like a hinged lid, preventing sodium from moving through the channel (65).

The binding of the IFMT particle is voltage-independent, but the entire fast inactivation process is voltage-dependent (5,66,67). The voltage-dependence of fast inactivation is conferred by a prior step, the movement of DIVS4, that makes the binding site for IFMT available (20). The voltage-dependence of DIVS4 movement matches the voltage-dependence of fast inactivation (68). The movement of DIVS4 is also rate-limiting in fast inactivation and is sufficient to allow binding of the IFMT particle (20). The stability of the fast-inactivated state can be altered by mutants. Destabilization of this state allows for a small fraction of channels that fail to fast inactivate (69,70). These channels pass a non-inactivating current that is also termed persistent or late sodium current.

After the cell repolarizes, the voltage-sensors deactivate and the inactivation particle unbinds from the channel. Interestingly, approximately half of the inward gating charge movement is slowed following fast inactivation (71). Intracellular pronase, which digests the fast inactivation particle, removes this charge immobilization (71). The immobilized charge is the gating charges of DIIS4 and DIVS4, which are locked in their activated states by the bound fast inactivation particle and recover on the same time scale as fast inactivation recovery (71,72). Since disruptions of fast inactivation decrease

immobilized charge, immobilized charge can be used as a measure of the stability of sodium channel fast inactivation (71,73).

The C-terminus plays an important role in modulating the voltage-dependence and completeness of fast inactivation as well as acting as a sensor for intracellular calcium. Multiple functional and structural studies of the sodium channel C-terminus highlight the ability of sodium channels to respond to changes in the intracellular calcium concentration (46,74–79). The consensus of these studies is that the C-terminus forms an EF-hand like domain, followed by an IQ motif (80,81). Generally, EF-hand domains act as calcium binding domains, while IQ motifs allow binding of calmodulin. The exact role of the EF-hand like domain in sodium channels is controversial with some data suggesting direct calcium binding in a physiologically relevant range, while other studies suggest a structural role with low calcium affinity (47,77). Conversely, the IQ motif in sodium channels is believed to bind calmodulin as does a site in the DIII-DIV linker (46,47,82). One model suggests that calmodulin forms a bridge between the C-terminus and the DIII-DIV linker allowing the C-terminus to regulate fast inactivation in a calcium-dependent manner (46). In this model, at low calcium concentrations the C-lobe of calmodulin is bound to the C-terminal IQ motif. When the intracellular calcium concentration increases the C-lobe of calmodulin binds calcium and then binds to the DIII-DIV linker. The N-lobe of calmodulin is then free to bind the IQ motif in the C-terminus forming a calmodulin bridge between the C-terminus and the DIII-DIV linker (Figure 1.4). Interaction between the C-terminus and DIII-DIV linker may also occur in the absence of calmodulin (83). The structure of NavPas from the American Cockroach shows direct interactions between the C-terminus and DIII-DIV linker as well as between the C-terminus and the intracellular loops of DIV (9).

Functionally, the C-terminus, calcium, and calmodulin are important in determining the voltage-dependence, rate, and stability of fast inactivation. Increases in intracellular calcium depolarize the voltage-dependence of fast inactivation (74,77). Mutants in the EF hand-like domain and IQ motif decrease the sensitivity to calcium and calmodulin while increasing the fraction of non-inactivating channels (77,84). Interestingly, increasing the intracellular calcium concentration decreases non-

inactivating current in the deltaKPQ (DIII-DIV linker), 1795insD (C-terminal), and Q1909R (C-terminal) mutants while calmodulin over-expression decreases non-inactivating current in the E1901Q (C-terminal), Q1909R (C-terminal), and R1913H (C-terminal) mutants (75,76,79).

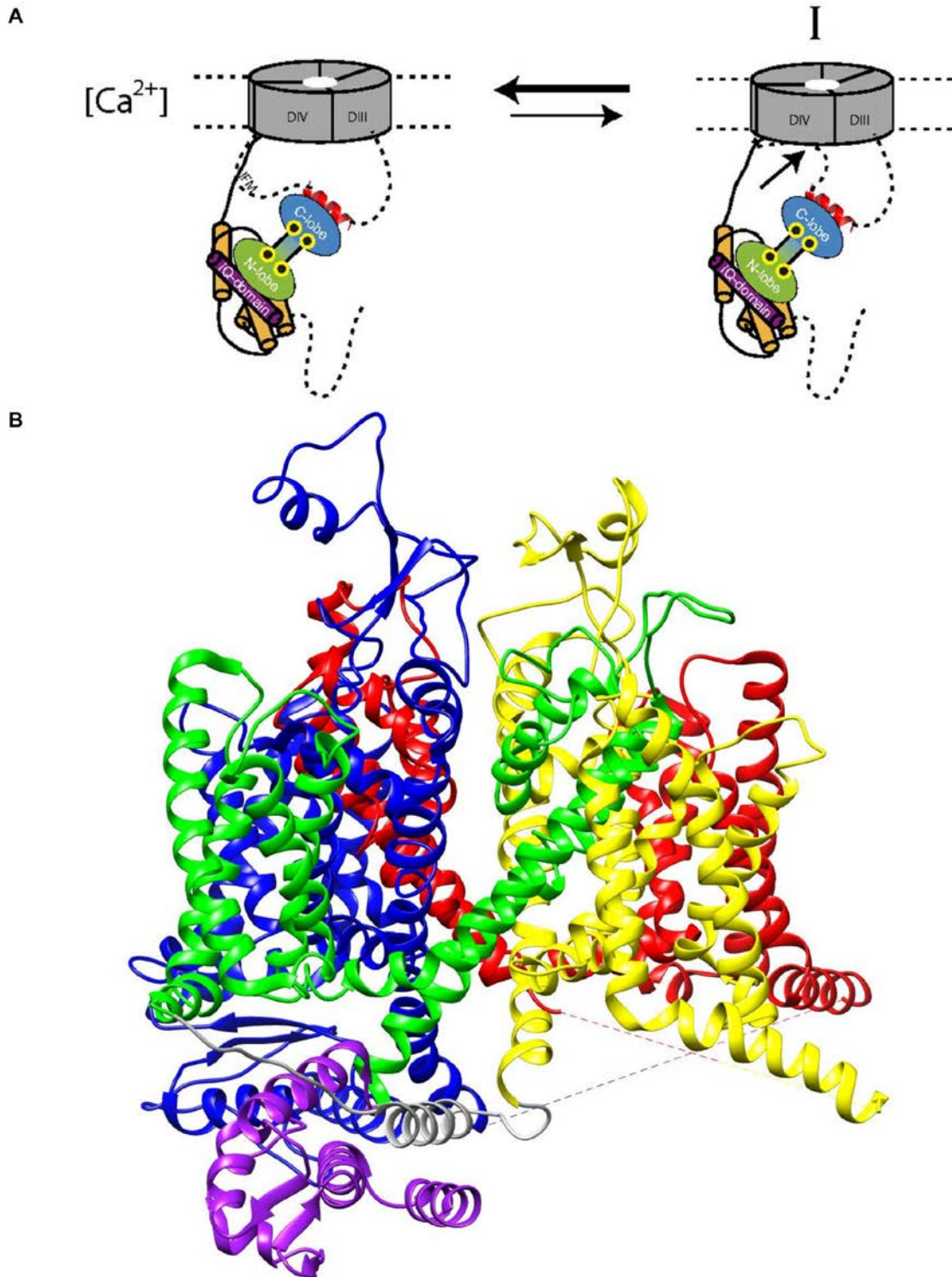


Figure 1.4. C-Terminal Interactions with the DIII-DIV linker

A: Model of a proposed calcium-calmodulin dependent interaction between the C-terminus and the DIII-DIV linker. In the presence of calcium, the N-terminal domain of calmodulin binds the IQ motif in the sodium channel C-terminus while the C-terminal domain of calmodulin binds the sodium channel DIII-DIV linker. The calmodulin bridge stabilizes channel fast inactivation. From Sarhan *et al.*, 2012 (46). **B:** Structure of the NavPaS sodium channel showing the interaction between the C-terminus (purple) and the

DIII-DIV linker (gray). In the NavPaS structure, the C-terminus interacts directly with the DIII-DIV linker and the DIVS4-S5 linker (PDB ID: 5X0M) (9).

1.2.3. Sodium Channel Slow Inactivation

Sodium channels can also become inactivated in a process called slow inactivation (85,86). Physiologically, slow inactivation occurs during repetitive or prolonged depolarizations of sodium channels thereby limiting channel availability over longer time periods. While fast inactivation occurs in the millisecond time range, slow inactivation occurs on the time scale of seconds. The exact process by which slow inactivation occurs is unknown, but involves voltage-sensor movement as well as rearrangement of the channel pore and selectivity filter (87–90).

Voltage-sensors may cause slow inactivation through voltage-sensor relaxation. The active conformation of channel voltage-sensors is not the most stable outward conformation; studies in voltage-gated potassium channels and voltage-gated sodium channels shows the existence of one or more relaxed state conformations (88,89,91,92). Voltage-sensor relaxation also occurs in *Ciona intestinalis* voltage-sensitive phosphatase, suggesting the relaxed state is intrinsic to voltage-sensors (91). In Nav1.4 the relaxation rates of the voltage-sensors in DI-DIII correlates well with the slow inactivation (88). This correlation is also true in the L689I mutant in Nav1.4, which causes corresponding decreases in channel slow inactivation and voltage-sensor relaxation (89). Additionally, when TTX is added, a time constant of slow inactivation is impaired in the 10 s range as is a corresponding relaxation movement in DIS4 and DIIS4 (88). These experiments suggest that the relaxation movements of the voltage-sensors in the first 3 domains of voltage-gated sodium channels are responsible for slow inactivation of the channel pore. Although these experiments did not identify a role of DIVS4, other studies have implicated the movement of DIVS4 in slow inactivation. Removing fast inactivation in sodium channels increases the number of channels which enter the slow inactivated state (93,94). Furthermore, the conformation of the channel selectivity filter rearranges during slow inactivation and is tied to the movement of DIVS4 (95). Based on these data Silva and Goldstein hypothesized that DIVS4 may be involved in intermediate slow inactivation at time scales less than 1 s (88,89).

The mechanistic link between voltage-sensor relaxation and slow inactivation of the pore has yet to be fully elucidated. Given that the movements of the voltage-sensors are transferred to the channel pore in the activation and deactivation processes, relaxation movements also altering the conformation of the pore is not a stretch of the imagination. The crystal structure of the archaebacterial NavAb suggests that slow inactivation is due to collapse of the pore and selectivity filter (48). This collapse was accompanied by formation of a new interaction between the S4-S5 linker segment and the S6 segment. A possible model is, therefore, that voltage-sensor relaxation allows for an interaction between the S4-S5 linker and the S6 segments. The rearrangement of pore domain to form this new interaction causes selectivity filter and pore collapse which prevents current conduction through the channel.

1.2.4. Modulation of Sodium Gating by Accessory Proteins and Molecules

Sodium channels are associated with numerous accessory proteins that alter channel gating. These include beta-subunits, caveolin, fibroblast growth factors (FGF), and calmodulin (96–100). These associated proteins and regulators alter channel trafficking, expression and gating parameters. In some cases, these accessory proteins may even block the channel, producing inactivation-like states (101).

Although capable of functioning independently, in humans the voltage-gated sodium channel α -subunit associates with sodium channel β -subunits (102). There are 5 sodium channel β -subunits, β 1 through β 4 and β 1B, that are expressed in tissues throughout the body. β 1 through β 4 are formed by an extracellular N-terminal immunoglobulin domain, an α -helical transmembrane segment, and an intracellular C-terminus. β 1B is a splice variant of the SCN1B gene with only the extracellular domain. While β 1 and β 3 interact with the α -subunit of the sodium channel through non-covalent interactions, β 2 and β 4 interact covalently. This covalent interaction is between C55 (β 2) or C58 (β 4) and a cysteine triad in the DIIS5-S6 linker of the α -subunit. In the TTX-resistant channels this cysteine triad is missing. Unlike in Nav1.2, no protection from the tarantula toxin peptide ProTx-II is granted in Nav1.5 by β 2 expression (103). This suggests that β 2 and β 4 do not regulate Nav1.5 function.

In 1992, Lori Isom, “the inventor of the β -subunit” (L. Isom, personal communication, Feb. 8, 2017), and colleagues provided the first functional characterization of β -subunit effects on sodium channels (96). They showed that the rat β 1-subunit accelerates inactivation, hyperpolarizes the voltage-dependence of fast-inactivation, and increases current amplitude of the rat Nav1.2 channel. The effects of β 1 and β 3 on Nav1.5 remain controversial with some studies showing a hyperpolarization of the voltage-dependence of fast inactivation and others suggesting depolarization of fast inactivation (104,105). Similarly, while one of these reports suggested that β 3 slows fast inactivation recovery and β 1 and β 3 accelerate fast inactivation onset, the other suggests that β 1 accelerates fast inactivation recovery and β 3 may slightly decelerate fast inactivation onset. The differences in these reports may be due to the expression system as one was from Chinese hamster ovary cells and the other was from *Xenopus laevis* oocytes (104,105). Still other studies suggest that the β 1 subunit does not affect gating, but rather expression. SCN1B knockout mice show increased transient and non-inactivating sodium currents and elongated QT intervals with no changes to channel gating (106).

Sodium channel gating is also modified by fibroblast growth factors (FGF) (101). A crystal structure of the Nav1.5 C-terminus shows FGF13 bound distal to the EF-hand like domain and proximal to the IQ motif (47). FGF14 splice variant 1A decreases Nav1.5 currents in HEK cells by directly blocking the channel pore. FGF14 also shifts the voltage-dependence of inactivation to more depolarized potentials (107).

Sodium currents are further regulated by the adrenergic stimulation from the autonomic nervous system. β -adrenergic stimulation increases peak sodium currents (108–110). One possible mechanism behind sodium channel regulation by β -adrenergic stimulation is increased membrane expression of sodium channels (111). Increased channel expression in rat cardiac myocytes is entirely blocked in the presence of caveolin 3 antibodies, suggesting a role for caveolin based trafficking of sodium channel containing vesicles (97). Caveolin may also play a role in modulating sodium channel gating as caveolin 3 mutants increase the fraction of non-inactivating channels (98). β -adrenergic stimulation leads to PKA based phosphorylation of sodium channels. PKA

also hyperpolarizes the voltage-dependence of fast inactivation and activation (110,112). The DI-DII linker in Nav1.5 is a major player in channel phosphorylation as replacement with the DI-DII linker of Nav1.4 abolishes many effects (113).

The importance of accessory subunits is underscored by their role in electrical diseases. All of β 1 through β 4 are associated with cardiac diseases including atrial fibrillation, Brugada syndrome, and Long QT syndrome (106,114–118). FGF14 knockout mice suffer from severe neurological deficits with altered sodium channel gating (99). And mutants in the C-terminus that disrupt the calcium-calmodulin machinery can lead to both Brugada syndrome and LQT3 (75,77,79).

1.3. Sodium Channels and Disease

Electrically excitable tissues are sensitive to improper gating behaviour in the underlying ion channels. Single missense mutants in voltage-gated sodium channels may cause fatal electrical diseases. Epilepsy syndromes are defined by hyperexcitability of the nervous system and are associated with non-inactivating sodium currents and resurgent sodium currents during repolarization (119). These gain-of-function effects are caused by mutations in SCN1A, SCN2A, SCN3A, SCN8A, and SCN1B (119–124). Nav1.4 mutants cause either myotonic or paralytic syndromes, both of which are associated with abnormal inactivation (125). And Nav1.5 mutants have been classified as gain-of-function mutants that increase non-inactivating current, causing LQT3, and loss-of-function mutants that decrease peak current, causing BrS1 and conduction defects (69,126).

What is increasingly being discovered, however, is that sodium channel mutants may have a mixture of loss-of-function and gain-of-function effects that interact with external factors. Mutants in Nav1.1 may cause increases or decreases in the sodium current leading to a spectrum of epilepsy disorders including Generalized Epilepsy with Febrile Seizures plus and Dravet syndrome (119). Interestingly, the same mutant may display both loss-of-function and gain-of-function effects. In the A1273V mutant, febrile temperatures unmask both gain and loss-of-function that may alter neuronal action

potential firing (127). Similarly, the P1158S mutant in Nav1.4, which causes an overlapping syndrome of hypokalemic periodic paralysis and myotonia congenita, displays both loss-of-function and gain-of-function properties that are dependent on pH (128,129). A model based on these data suggests that lowered extracellular pH results in an increased non-inactivating sodium current that switches the P1158S mutant from a periodic paralysis phenotype to a myotonic phenotype. Overlapping disease phenotypes are also seen in Nav1.5, with single mutants capable of causing LQT3, Brugada syndrome, or a mixed phenotype (130). These mutants include the first characterized LQT3 mutant, deltaKPQ (1505-1507), located in the DIII-DIV linker; the most prevalent sodium channel mutant, E1784K, located in the C-terminus; the famous Dutch founder mutant, 1795insD, located in the C-terminus; the deltaK1500 mutant in the DIII-DIV linker; the delF1617 mutant in the DIVS3-S4 linker; and the L1786Q mutant in the C-terminus. All of these mutants increase non-inactivating sodium current and alter the rate or voltage-dependence of fast inactivation (2,69,70,75,130–146).

1.3.1. The Cardiac Action Potential

Sodium channels play a key role in the electrical signalling cascade that coordinates the beating of the heart. Each heart beat is initiated by a depolarization of the pace making cells of the sinoatrial node. This depolarization is conducted through the atria, down the Bundle of His and bundle branches in the interventricular septum to the apex of the ventricles. This depolarization brings the membrane potential of the ventricular cardiomyocytes to the activation threshold of Nav1.5, triggering an action potential.

The ventricular cardiomyocyte action potential has 5 phases, due to the asynchronous action of voltage-gated sodium, calcium and potassium channels (Figure 1.5). The phase 0 depolarization is due to the influx of sodium through active sodium channels. The flow of sodium rapidly ceases at the end of phase 0 due to fast inactivation of the channel. The phase 1 notch is caused by the transient outward potassium current through Kv1.4, Kv4.2, and Kv4.3. The extent of repolarization is greater in the outer heart wall, known as the epicardium, than it is in the inner heart wall, known as the

endocardium. Phase 2 is the action potential plateau, during which calcium influx through Cav1.2, the L-type calcium channel, is counteracted by the outward, slow and rapid delayed-rectifier potassium currents through Kv7.1 and Kv11.1, respectively. The phase 3 repolarization occurs when the delayed-rectifier potassium currents overcome the L-type calcium current allowing for the full repolarization of the ventricles. Phase 4 is the resting membrane potential which is maintained by potassium efflux through the inward-rectifier potassium channel Kir2.1.

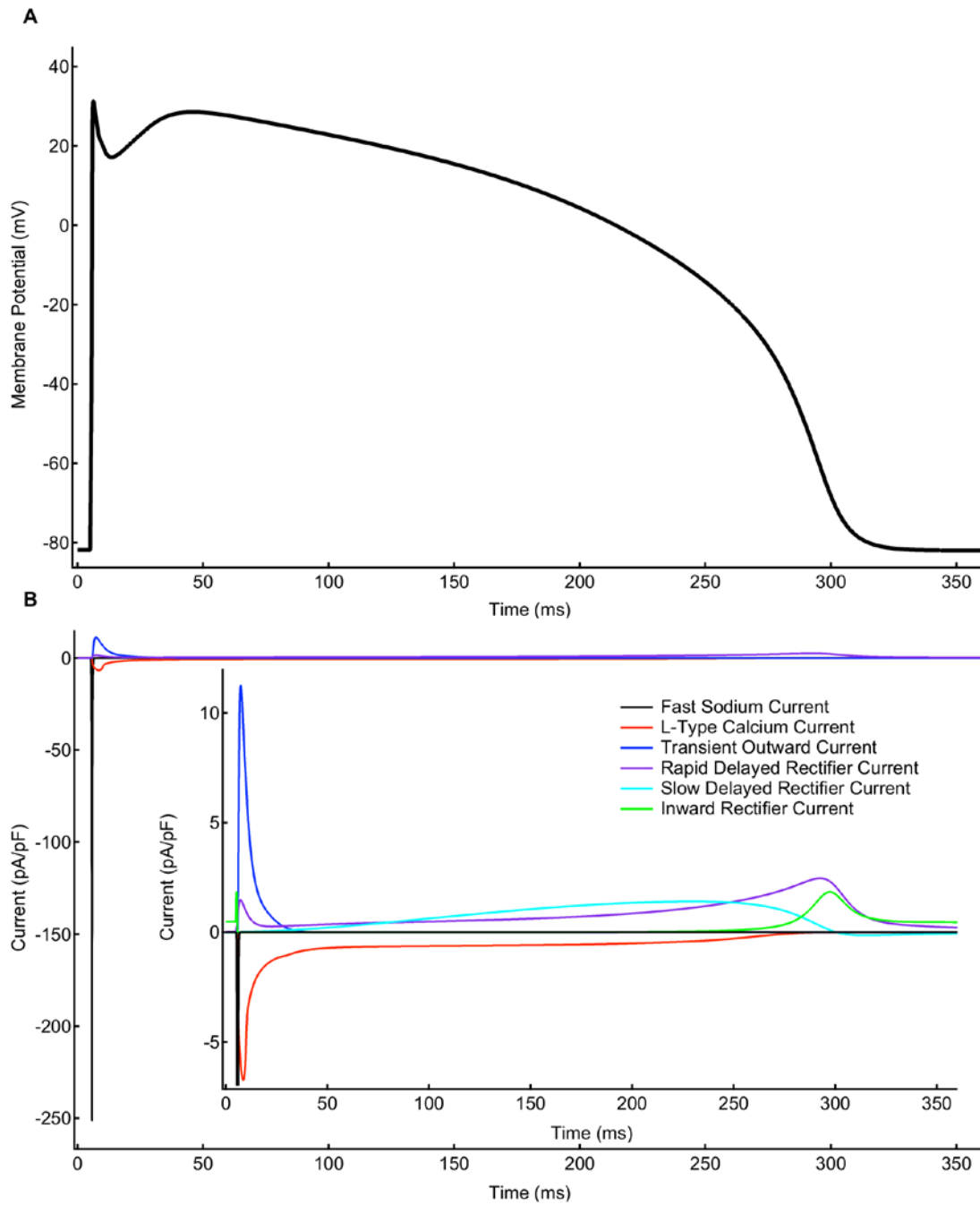


Figure 1.5 The Ventricular Cardiomyocyte Action Potential and its Underlying Currents

A: A single ventricular cardiomyocyte action potential plotted over time. **B:** Major currents during the ventricular action potential. **B inset:** Zoomed in plot of the major currents activate throughout the ventricular action potential. The fast sodium current is responsible for the action potential upstroke. All traces are simulated with a ten Tusscher 2006 model.

1.3.2. Long QT Syndrome

Congenital Long-QT syndrome (LQTS) is associated with mutations in 17 genes (147–149); however, 90 % of inherited LQTS cases are due to mutations in three genes: KCNQ1 (LQT1), KCNH2 (LQT2), and SCN5A (LQT3) (150). LQTS is characterized by an elongated QT interval on an electrocardiogram (ECG) in conjunction with a personal or family history of syncope or sudden cardiac death. The first known ECG of a patient with LQTS was recorded in 1957 by Jervell and Lange-Nielsen (151); however, the first possible report of LQTS is from 1856 by Friedrich Ludwig Meissner (152). The LQTS documented by Jervell and Lange-Nielsen, now termed Jervell and Lange-Nielsen syndrome, was associated with congenital deafness and represents a rare form of LQTS with an autosomal recessive mode of inheritance (153). The more common LQTS type, Romano-Ward syndrome, which is inherited with an autosomal dominant pattern, was discovered in the 1960s and is not associated with deafness (154,155).

At a cellular level, LQTS is caused by an elongation of the ventricular action potential plateau due to delayed phase 3 repolarization. This elongation may be caused by mutants, drugs, or environmental factors which decrease repolarizing currents or increase depolarizing currents during the action potential plateau. LQT1 is the most common congenital LQTS and is caused by loss-of-function mutations, which decrease the slow delayed-rectifier potassium current through $K_v7.1$ (156). LQT2 is caused by loss-of-function mutants in $K_v11.1$ which decrease the rapid delayed-rectifier potassium current (157). Pharmaceutical block of $K_v11.1$ is the most common cause of acquired LQTS (158). In contrast to LQT1 and LQT2, LQT3 is due to mutations that cause a gain-of-function in $Nav1.5$, which increases the fraction of non-inactivating sodium current which is active throughout the action potential plateau (159). Non-inactivating sodium current both delays action potential repolarization and may further predispose patients to arrhythmia by altering calcium handling (160). Entry of sodium throughout the action potential plateau may decrease the ability of the sodium-calcium exchanger to shuttle calcium out of the cell. This increases the amount of calcium pumped into the sarcoplasmic reticulum and can cause spontaneous calcium release and after-depolarizations (161).

The elongation of the QT interval in LQT3 patients is greatest at low heart rates and arrhythmias are most common during sleep (162,163). This is in contrast to LQT1, where arrhythmia is most common during exercise (163). A simulation study suggested that action potential elongation during tachycardia is due to an imbalance between the non-inactivating sodium current and the slow delayed-rectifier potassium current (164). At elevated heart rates, the Kv7.1 potassium channel does not fully deactivate between action potentials. Consequently, the slow delayed-rectifier potassium current is large enough to overwhelm the non-inactivating sodium current. In contrast, bradycardia allows full deactivation of Kv7.1 during diastole and, therefore, the repolarizing potassium current during the action potential plateau is much smaller. This allows the non-inactivating sodium current to delay repolarization. An alternative mechanism is dependent on increased intracellular calcium concentrations at elevated heart rates (165). Increases in intracellular calcium may reduce the non-inactivating sodium current in some mutants, thereby attenuating action potential prolongation during tachycardia (75,76). Although, arrhythmia is most common during sleep, LQT3 exhibits heterogeneity between patients (163). The effects of environmental triggers and the efficacy of treatment options in LQT3 patients both appear to be dependent on the specific mutant (75,166,167). This underscores that variability exists even within patients carrying mutations of the same gene, indicating the need for patient-specific recommendations.

1.3.3. Brugada Syndrome

Brugada syndrome was first described as a distinct syndrome in 1992 (168). The syndrome is characterized by right bundle branch block and an ST segment elevation in leads V₁-V₃. The 8 original patients developed polymorphic ventricular tachycardias, recurrent aborted sudden cardiac deaths, and, in one case, sudden death. In Brugada syndrome the ST-segment abnormalities are graded, with only the type I ECG considered diagnostic when found in conjunction with a personal or family history of sudden death, syncope, or arrhythmia (169). The type I ECG includes greater than 2 mm elevation at the J-point followed by a descending ST-segment and an inverted T-wave in leads V₁ through V₃. Type II and III ECGs are suggestive of Brugada syndrome when present in

patients with personal or family histories of syncope, arrhythmia, or sudden death. Both the type II and III ECGs include J point elevation and a positive T-wave. Clinicians may use sodium blockers, such as ajmaline, to try to elicit a type I ECG in suspected Brugada syndrome patients.

Two mechanisms, both with substantial supporting evidence, are suggested for the pathophysiology of Brugada syndrome and the appearance of the Brugada syndrome ECG (170–172). The repolarization hypothesis is based primarily on recordings of ventricular tissue. This hypothesis suggests that decreases in peak sodium current cause a decrease in the phase 0 depolarization of the ventricular cardiomyocyte. In conjunction with a large phase 1 transient outward potassium current, this can cause early repolarization of ventricular cardiomyocytes (Figure 1.6) (170,173). The right epicardium is the region most likely to repolarize early due to the large transient outward current in that region. The repolarization hypothesis states that early repolarization of the right epicardium causes a large heterogeneity of repolarization across the right ventricular wall that is responsible for the ST-segment elevation in leads V1-V3. This heterogeneity of repolarization allows for a triggered action potential during phase 2 of the action potential which leads to generation of ventricular arrhythmias.

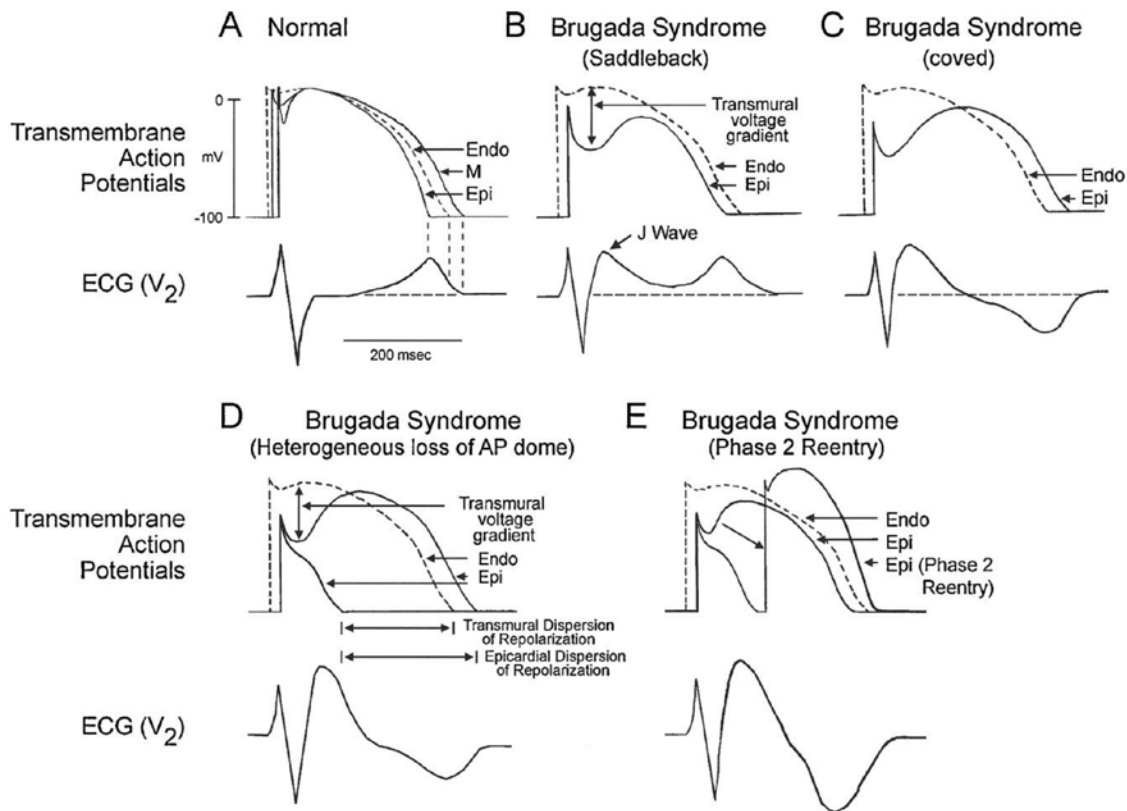


Figure 1.6. The Repolarization Hypothesis for Brugada Syndrome

Schematic of the repolarization hypothesis for the Brugada syndrome ECG. **A:** Normal action potential morphologies for endocardial, epicardial, and midmyocardial tissue and the corresponding normal ECG waveform. **B:** Decreased sodium current allows for greater repolarization of the epicardial action potential by the transient outward potassium current. The increased repolarization in the epicardium causes J-point elevation on the ECG. **C:** Further decreases in the fast sodium current lead to a delay in the action potential plateau, leading to an elongated epicardial action potential. This elongation causes T-wave inversion on the ECG. **D:** Decreased sodium current can lead to a full phase 1 repolarization in some epicardial tissue. **E:** Repolarization during phase 1 allows for a second, triggered action potential during phase 2. Taken with permission from Antzelevitch, 2006 (174).

The depolarization hypothesis is primarily based on mathematical models and clinical assays, including body surface potential mappings and ECGs. The depolarization hypothesis postulates that the Brugada syndrome ECG and the right bundle branch block pattern are due to a delay in conduction to the right ventricular outflow tract (170,172). The conduction delays create a heterogeneity of depolarization which is responsible for ST-segment abnormalities (Figure 1.7). Data from the explanted heart of a Brugada syndrome patient showed delayed activation of the right ventricular outflow tract and generation of ventricular arrhythmias from that region (175).

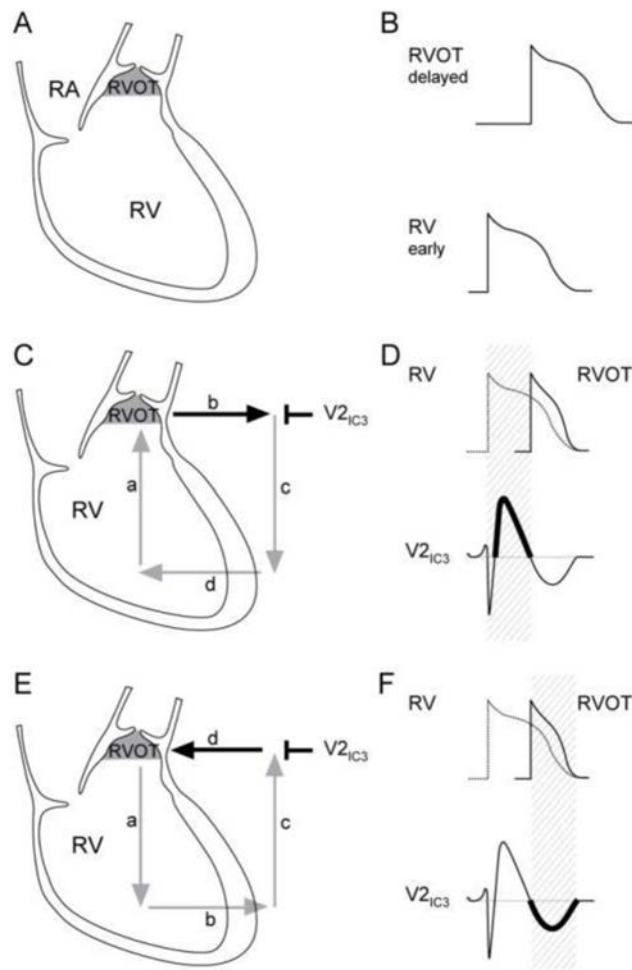


Figure 1.7. The Depolarization Hypothesis for Brugada Syndrome

Schematic of the depolarization hypothesis for the Brugada syndrome ECG waveform. **A:** Diagram of the right atrium (RA), right ventricle (RV), and right ventricular outflow tract (RVOT). **B:** Slowed conduction delays the action potential in the RVOT relative to the RV. **C and D:** Delayed activation of the RVOT relative to the RV causes J-point elevation on the ECG in the right precordial lead, V2. **E and F:** Delayed repolarization of the RVOT relative to the RV causes T-wave inversion in lead V2. Taken with permission from Wilde *et al.*, 2010 (171).

Other aspects of Brugada syndrome also remain controversial, including the importance of the SCN5A mutations. Studies in large families carrying SCN5A mutations have shown that a small number of mutation-negative individuals have Brugada syndrome (176). However, the same study suggests that penetrance of Brugada syndrome is approximately 5 times greater in family members carrying SCN5A mutations. As approximately 20 % of Brugada syndrome cases with a known genetic cause are due to mutations in SCN5A (BrS1), with up to 15 % more due to mutations in

SCN10A, and rare variants in each of Nav β 1-3, sodium channel associated mutations remain the largest genetic contributor (177).

What does seem likely is the need for additional factors that increase the potential for arrhythmia in SCN5A mutation carriers. Clinically this may be accomplished using sodium channel blockers, typically ajmaline or flecainide, to block currents through Nav1.5. In patients, age is suspected to play a large role in eliciting ST segment abnormalities and arrhythmia. A recent study in a large family with the E1784K mutant noted that SCN5A mutation carriers over the age of 40 had significantly longer PR intervals and QRS duration than mutation carriers under 40 (178). Aging may lead to structural rearrangement and fibrosis which cause further electrical instability.

Currently the best whole animal models of Brugada syndrome are an established heterozygous SCN5A knock-out mouse line and a more recent line of pigs. The mice develop conduction abnormalities and susceptibility to ventricular arrhythmias at an early age (179). At 12-24 weeks ST segment elevation can be elicited with flecainide in these mice (180). The heterozygote mice also develop significant fibrosis in the working myocardium, with onset at an undetermined point between 16 and 50 weeks (181,182). Fibrosis in these animals is associated with greater conduction slowing. This illustrates the link between electrical signals and cardiac structure. Sodium channel mutants may lead to structural changes in the heart and structural changes may in turn influence sodium channel expression (183,184).

The first large animal model is the Yucatan mini pig model. These animals are heterozygotic for a truncation mutant 558X in Nav1.5. The pigs show conduction abnormalities at an early age, however, ST-segment elevation has not been found in these animals (185). The lack of ST-segment abnormalities may be due to the lack of a transient outward current in the pig. It may also indicate that a further substrate, possibly fibrosis, is necessary for the development of Brugada syndrome in these animals.

1.4. Environmental Regulators of Electrical Signalling

Electrical signalling in humans is affected not only by mutants, but also alterations in the internal environment of the body. Hypoxia induced activation of voltage-gated sodium channels can trigger neuronal cell death (186). Hyperthermia triggers seizures in generalized epilepsy with febrile seizures plus and Dravet syndrome (119,187). Hyperthermia may also unmask Brugada syndrome (188,189). Similarly, hyperthermia induces myotonia in carriers of the Nav1.4 P1158S mutant, while hypothermia causes periodic paralysis in the same patients (190). Finally, changes in cardiac pH during ischemia can elongate the QT interval, cause ST segment abnormalities, and trigger ventricular arrhythmias (191–194).

Changes to the internal environment of the body not only act as triggers for electrical dysfunction in patients with sodium channel mutants, but may be sufficient to elicit symptoms of electrical disease in the absence of an underlying mutant. Seizures occur in patients with Glutaric aciduria type 1, Propionic acidemia, and methylmalonic acidemia (195–197). And in Brugada phenocopy a Brugada syndrome like ECG occurs due to environmental changes in the absence of an underlying mutation (198). In one case of hypokalemia-induced Brugada phenocopy the ECG was resolved and then returned upon recurrence of hypokalemia in the patient (199). Brugada phenocopy is also known to be elicited by cocaine ingestion, cardiac ischemia, and acute pulmonary embolism (200–204).

1.4.1. pH and Sudden Cardiac Death

Arrhythmia and sudden cardiac death are associated with exercise, sudden infant death syndrome (SIDS), ischemia, and cocaine use (163,205–211). Cocaine directly blocks sodium channels and is associated with Brugada syndrome-like ECGs, ventricular tachycardia, and ventricular fibrillation (200,201,212). Exercise may be used clinically to elicit arrhythmia in those suspected of carrying LQT and Brugada syndrome mutations (213). A recent analysis of tissue from 191 child sudden unexplained death cases found pathogenic variants in cardiac genes in 6.7 % of cases and variants of unknown

significance in 26.7 % of cases (214). Brugada syndrome may also be responsible for some SIDS cases (210,211). And cardiac ischemia is associated with an elongated QT interval, ST-segment abnormalities, and arrhythmia (215–217).

A factor common to these triggers is changes in extracellular pH. Exercise causes small changes to arterial pH, SIDS is associated with arterial blood pH less than pH 7.0, cocaine ingestion can decrease arterial blood pH below pH 6.3, and ischemia can lower cardiac pH to pH 6.0 (200,215,218–224). When blood pH decreases, the extracellular cardiac pH mirrors these changes, thus decreases in arterial pH decrease extracellular cardiac pH (225). Decreases in intracellular cardiac pH occur in respiratory acidosis and in metabolic acidosis with extracellular pH below pH 6.8, thus the type of acidosis is important when considering acidaemia (224,226–228). Cocaine ingestion causes metabolic acidosis, while in SIDS evidence supports both respiratory and metabolic acidosis (200,219,220,229–233). Of the cases listed, the most severe decreases in pH occur during cardiac ischemia. Brief serial ischemic episodes and no-flow ischemia both induce large decreases in extracellular pH to below pH 6.0 (215,222–224,234). As duration of the ischemia increase, so to does the severity of acidaemia.

1.4.2. Proton Modulation of Cardiac Channel Gating

Increases in extracellular protons alter many aspects of voltage-gated sodium channel gating. Protons decrease maximal channel conductance and depolarize the voltage-dependence of activation, fast inactivation, and slow inactivation (235). Interestingly, decreasing intracellular pH in a similar range to extracellular pH appears to have minimal or no effect on voltage-gated sodium channels (128,206). This suggests an extracellular interaction site for protons.

Experiments in guinea pig cardiomyocytes show that protons directly block sodium channels, decreasing single channel conductance (236). In multi-channel assays this proton block causes a decrease in the maximal conductance. Early experiments by Woodhull suggested that block of the channel pore is voltage-dependent as proton block is decreased at positive membrane potentials (237). Woodhull proposed a proton binding site one quarter of the distance from the extracellular to intracellular membranes.

Currently, the known binding sites for protons include the selectivity filter, the outer charged ring, residue H880 and residue C373 (55,238–240). Replacement of the selectivity filter carboxylates increases the fraction of sodium current resistant to proton block by approximately 25 % (55). The presence of the C373 residue, which also confers TTX resistance, allows for full proton block of sodium channels. In Nav1.4, where the analogous residue is Y401, 12–17 % of the current is resistant to protons. The C373F and C373Y mutants in Nav1.5 impart a similar proton-insensitive current as does the H880Q mutant (239,240).

Many of the proton-induced changes to channel gating have an underlying proton effect on the channel gating currents. The voltage-dependence of gating current activation is depolarized by decreasing extracellular pH (73). This depolarization of voltage-sensor movement would account for the depolarization of the conductance-voltage (GV) relationship and the voltage-dependence of fast inactivation. Extracellular protons also slow outward gating charge movement and accelerate inward gating charge movement (73). Slowed activation and accelerated deactivation of the DIVS4 would explain the proton-dependent slowing of fast inactivation onset and acceleration of fast inactivation recovery. Additionally, decreasing extracellular pH decreases the fraction of immobilized charge, indicative of a less stable fast inactivated state (73). Destabilization of the fast-inactivated state would explain the increased fraction of non-inactivating current when extracellular pH is decreased.

Structural studies and functional data from hERG potassium channels suggest a likely extracellular binding site for protons to affect the voltage-sensors. Similar to sodium channels, decreasing extracellular pH slows and depolarizes the outward movement of the voltage-sensors in hERG (241). Mutating the acidic residues D456 and D460 in S2 and D509 in S3 of hERG abolishes the effects of protons on channel activation (241). The 2011 crystal structure of the *Arcobacter butzleri* voltage-gated sodium channel noted an aqueous cleft which exposed homologous extracellular acidic residues in the voltage-sensor to the extracellular solution (38). As these residues are responsible for stabilizing the S4 voltage-sensors in the active conformation, protonation

of these residues is a likely candidate for the depolarized and slowed outward movement of the voltage-sensors.

Overall, decreasing extracellular pH decreases peak sodium current, which could in turn decrease the action potential upstroke velocity, slowing conduction of electrical signals in the heart (235,242). Protons also destabilize the fast-inactivated state leading to increases in the fraction of non-inactivating current (235). As the effects of extracellular protons on sodium channels mirror the effects of cardiac sodium channel mutants that cause LQT3 and Brugada syndrome, acidosis may be particularly dangerous for those with an underlying Nav1.5 mutants associated with both Brugada syndrome and/or LQT3.

1.5. The E1784K mutant

The E1784K mutant in Nav1.5 is, along with deltaKPQ and 1795insD, one of the best studied mutants associated with both Brugada syndrome and LQT3. In one study of 44 LQT3-positive families from 7 referral centers, E1784K was the most common mutant (134). The E1784K mutant is particularly prevalent on the island of Okinawa where, in one study, 14 of 23 children who met the diagnostic criteria for LQTs harboured the E1784K mutant (136).

E1784K was first described as an LQTs mutant in a 3 generation family following the sudden death of a 13 year old girl (133). The initial biophysical characterization of the mutant showed that E1784K induces a 2-4 % non-inactivating sodium current. Additionally, the E1784K mutant shifts the voltage-dependence of fast inactivation to more hyperpolarized membrane potentials. The authors note that E1784K occurs in a region of the C-terminus that contains many negative charges. When sets of four of these charges were neutralized in WT channels (E1773Q/E1780Q/E1781Q/E1784Q and E1788Q/D1789Q/D1790Q/D1792Q), the voltage-dependence of fast inactivation was hyperpolarized in the resulting channels and a small fraction of non-inactivating current was also present.

Later biophysical characterizations of E1784K showed that the mutant affects most aspects of sodium channel gating (134,146). E1784K accelerates the recovery from and onset of fast inactivation. E1784K shifts the GV of the sodium channel to more depolarized membrane potentials and decreases the slope of the curve. The mutant also increases the fraction of channels that move into an intermediate slow inactivated state on a timescale less than 2 s. Notably, the E1784K mutant does not disrupt trafficking of the channel to the cell membrane (134). The summed effect of these shifts is a decrease in the peak sodium current transient and an increase in the non-inactivating sodium current.

Although E1784K was originally thought to cause LQT3 exclusively, it is now recognized as both an LQT3 and Brugada syndrome mutant. The first study of E1784K in the context of Brugada syndrome found a Brugada ECG in 9 of 41 carriers (134). A more recent study showed approximately 90 % of E1784K carriers have a positive ajmaline test for a Brugada ECG (178).

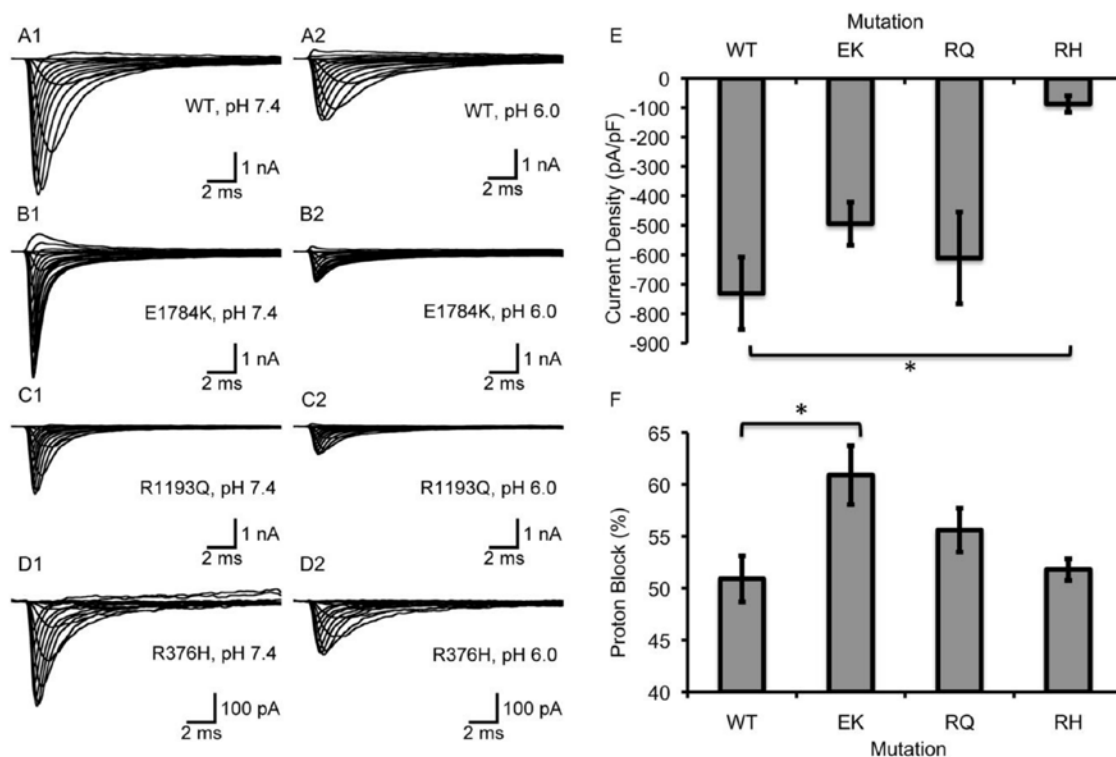


Figure 1.8. Maximal Conductance in the E1784K Mutant is Preferentially Blocked by Protons

Current density and proton block of wildtype and mutant $Na_v1.5$ channels. **A1-D2:** Sample macroscopic currents from WT, E1784K, R1193Q, and R376H channels at pH 7.4 and pH 6.0. Note that the scale for R376H currents is $1/10^{th}$ that of the other constructs. **E:** The R376H decreases the sodium current density compared to the other three constructs. **F:** The maximal conductance in E1784K is decreased to a greater extent by decreasing extracellular pH compared to wildtype channels. Taken with permission from Peters *et al.*, 2016 (2).

The necessity of ajmaline testing highlights an important question: why can a patient with a sodium channel mutant have many years of normal heart function before occurrence of an arrhythmia? One possibility is that external factors that lend further arrhythmogenic substrate are necessary to trigger an event. Elevated temperatures drastically increase non-inactivating sodium currents in E1784K mutants (243). Furthermore, while calcium decreases non-inactivating current in other mutants, it does not do so in E1784K (75). As protons block peak sodium currents and increase non-inactivating sodium current similar to Brugada syndrome and LQT3 mutants, decreases in pH may represent another potential trigger (235).

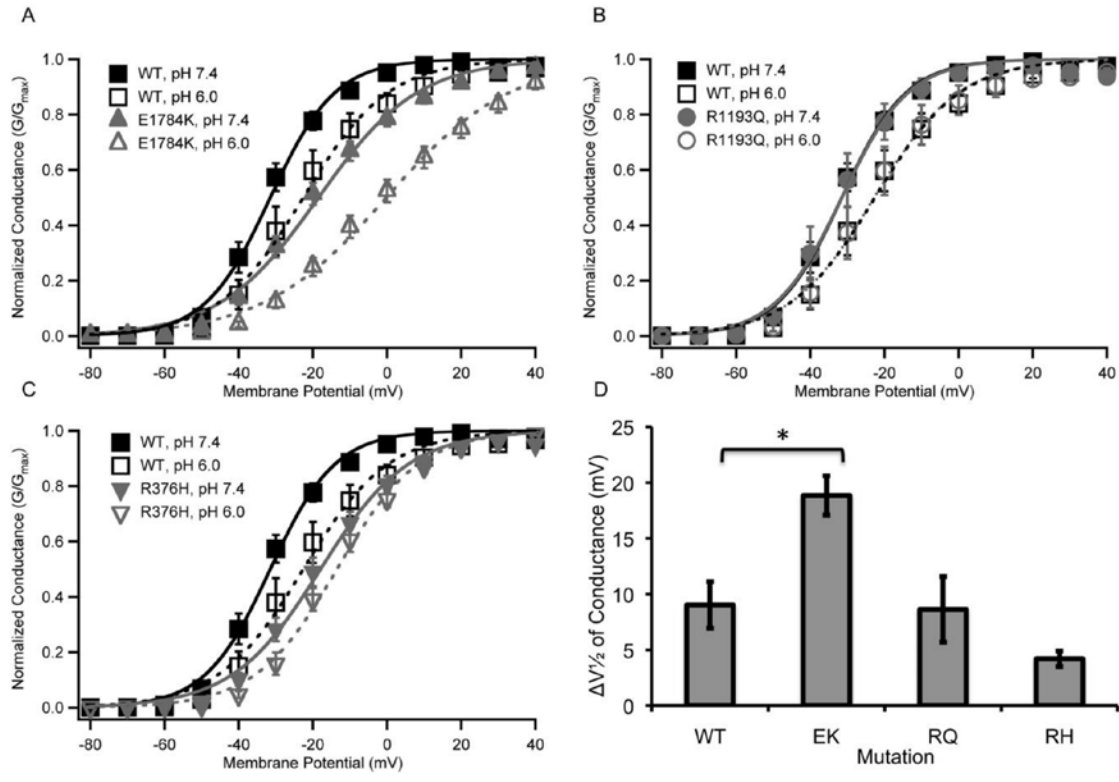


Figure 1.9. Protons Preferentially Depolarize the Conductance Curve in E1784K Nav1.5

A: Normalized conductance-voltage relationships of E1784K Nav_v1.5 at pH 7.4 and pH 6.0 overlaid with those of wildtype channels. **B:** Normalized conductance-voltage relationships of R1193Q Nav_v1.5 at pH 7.4 and pH 6.0 overlaid with those of wildtype channels. **C:** Normalized conductance-voltage relationships of R376H Nav_v1.5 at pH 7.4 and pH 6.0 overlaid with those of wildtype channels. **D:** The midpoint of the conductance-voltage relationship is depolarized more by decreasing extracellular pH to pH 6.0 in E1784K Nav_v1.5 than WT. Taken with permission from Peters *et al.*, 2016 (2).

I previously tested the effects of acidifying extracellular pH on 3 Nav1.5 mutants: the R376H mutant; the R1193Q (R1192Q) mutant; and the E1784K mutant (2). That study found that the E1784K mutant is preferentially sensitive to changes in extracellular pH. Compared to wildtype channels, E1784K maximal conductance is blocked by a further 10 % when extracellular pH is decreased to pH 6.0 (Figure 1.8). Lowering extracellular pH also depolarizes the GV curve by an extra 10mV in the E1784K mutant compared to wildtype (Figure 1.9). Finally, lowering extracellular pH from pH 7.4 to pH 6.0 increases the fraction of non-inactivating channels approximately 2 % more in E1784K (3 % to 7 %) than in wildtype channels (1 % to 3 %) (Figure 1.10; Note that the Y-axis in Figure 1.10E is mislabelled and should actually be from 0 % to 9 %). These data suggest that acidemia exacerbates the loss-of-function and gain-of-function of

E1784K Nav1.5, and potentially provides a trigger for arrhythmogenesis in E1784K carriers.

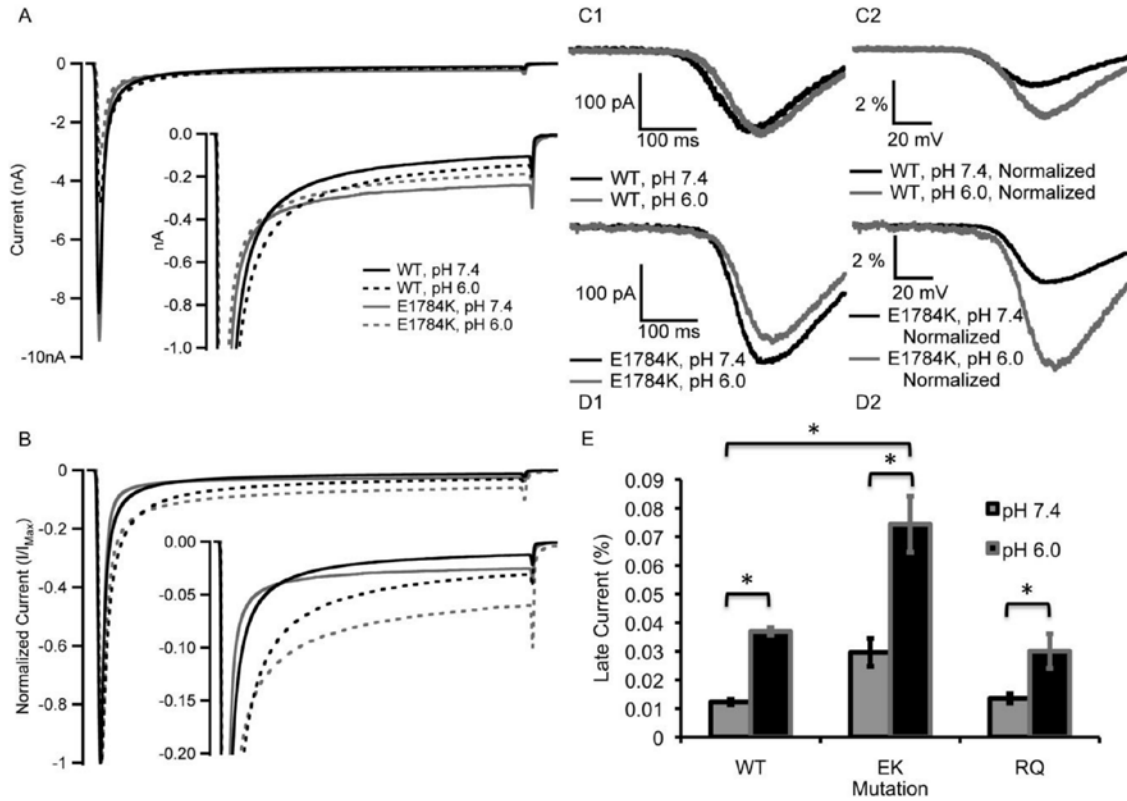


Figure 1.10. Lowered Extracellular pH Preferentially Increases Non-Inactivating Currents in E1784K Nav_v1.5

A: Sample non-inactivating currents from E1784K Nav_v1.5 and wildtype channels at extracellular pH 7.4 and pH 6.0. **B:** Traces from panel A normalized to the peak inward current. **C1-D2:** Sample sodium channel ramp currents in E1784K and wildtype Nav_v1.5 at extracellular pH 7.4 and pH 6.0. Currents were elicited by a 500ms ramp from -130mV to +20mV. Currents in C2 and D2 are normalized to peak inward sodium current recorded by a depolarization to 0mV prior to the ramp protocol. **E:** Decreasing extracellular pH to pH 6.0 increases the fraction of non-inactivating current to a greater extent in E1784K Nav_v1.5 than wildtype. Taken with permission from Peters *et al.*, 2016 (2).

1.6. Conclusion

Despite more than a half century of research, many aspects of sodium channel remain elusive. In many ways, sodium channel researchers have been hampered by a lack of structural evidence. The first structure of a heterotetrameric sodium channel was published earlier this year and shares only 40 % sequence homology to mammalian channels (9). The more recent structures of electric eel sodium channels share higher

homology, however, not all regions of the channel were resolved (10). Thus, for years researchers have relied on functional studies to guide our model of the sodium channel. From these studies, much has been learned about the function of channels in physiological and pathophysiological conditions. The first Nav1.5 mutant to be associated with LQT3, deltaKPQ, was studied in 1995 (69). The Brugada brothers first described Brugada syndrome in 1992 and it was first linked to mutations in SCN5A in 1998 (126,168). More than 400 mutants in the cardiac sodium channel have now been identified to underlie these diseases (<http://triad.fsm.it/cardmoc/>). Of these mutants the E1784K mutant is the most common and one of the best studied (134). Despite decades of research, it is not known how single missense mutants in the C-terminus of the sodium channel can alter nearly every aspect of channel gating. My projects have focussed on answering this question.

In project 1 I measure gating currents from E1784K Nav1.5 at pH 7.4 and pH 6.0 to determine whether the changes to channel conductance and preferential effects of extracellular protons are mediated by altered movement of the channel voltage-sensors. In project 2, I construct a new model of the voltage-gated sodium channel to test whether the effects of the E1784K mutant are mediated through fast inactivation. This simulation was later confirmed by recording voltage-sensor fluorescence from E1784K mutant channels, and recording currents from fast inactivation deficient channels. Finally, in project 3, I record ionic and gating currents of 8 different mutants at position 1784 to test whether the effects of the E1784K mutant on fast inactivation voltage-dependence and non-inactivating current are separable and which properties of residue 1784 are important for each disruption. The data that follow provides an explanatory model of how C-terminal mutations that underlie both Brugada syndrome and LQT can alter many aspects of channel gating.

Chapter 2. Proton Modulation of E1784K Ionic and Gating Currents

2.1. Introduction

The cardiac voltage-gated sodium channel, Nav1.5, passes an inward sodium current that is responsible for the upstroke of the ventricular cardiomyocyte action potential. Mutants that change the gating of Nav1.5 can alter action potential morphology leading to potentially fatal cardiac arrhythmias. Nav1.5 is composed of a single transcript encoding 4 domains (DI-DIV), each with 6 transmembrane segments (S1-S6) (37). In response to membrane depolarization, the positively charged S4 segments rotate and move towards the outside of the membrane (17,41,51). The movement of the S4s is physically coupled to the channel pore. Activation of the S4s in DI-DIII causes pore opening, allowing for conductance of sodium. The activation of the S4s produce a small but measurable gating current that can be used to map the conformational changes of the voltage-sensors *en masse* (16).

Following activation, the DIII-DIV linker segment binds to, and occludes, the internal channel pore, thereby blocking the inward movement of sodium ions, a process termed fast inactivation (62,244). The binding of the DIII-DIV linker is coupled to activation of DIVS4, which is rate limiting for fast inactivation (20). Mutants in the C-terminus of the voltage-gated sodium channel alter the rate and voltage-dependence of fast inactivation, suggesting coupling between the C-terminus and the fast inactivation machinery of the channel (130,133,146). One such mutant is E1784K, which shifts the voltage-dependence of fast inactivation to more hyperpolarized potentials and accelerates the rate of fast inactivation onset and recovery. The E1784K mutant also increases the fraction of channels that fail to enter the fast-inactivated state, increasing the non-inactivating current throughout the action potential plateau. Furthermore, E1784K shifts the conductance-voltage (GV) relationship to more depolarized potentials. The summed result of these shifts in gating is a decrease in the peak sodium transient followed by a non-inactivating current that is 2-4 % of the peak (2,133,134,146,178,243).

The E1784K mutant causes two cardiac diseases, long QT syndrome type 3 (LQT3) and Brugada syndrome. LQT3 is caused by gain-of-function channel defects that lead to incomplete inactivation and persistent inward current, prolonging the cardiac action potential (69,70). Action potential prolongation puts the patient at risk for cardiac arrhythmia (159,245). In contrast, Brugada syndrome is caused by mutants that decrease the peak sodium current (126). The consequence of this decrease is still being debated. The depolarization hypothesis suggests that this decrease slows conduction of the action potential throughout the ventricles, leading to heterogeneity of depolarization (170,171). The repolarization hypothesis suggests that the decreased sodium current allows for early repolarization of the epicardial cells in the ventricles, leading to heterogeneity of repolarization (173). In both hypotheses, the heterogeneity in the ventricles is believed to predispose the patient to triggered activity and ventricular arrhythmia.

Previous studies on E1784K have focused on the prevalence of LQT3 and Brugada syndrome signs in carriers and the biophysical characteristics of E1784K ionic currents (133,134,146,178). Our lab recently added studies on the temperature and pH sensitivity of the E1784K mutant heterologously expressed in Chinese Hamster Ovary cells (2,243). In wildtype (WT) channels, lowered extracellular pH decreases peak sodium currents and increases the fraction of non-inactivating sodium channels (235,246). We showed E1784K has preferential sensitivity to changes in extracellular pH, with an increased depolarizing shift of the GV curve, increased proton block of peak current, and an increase in the fraction of persistent current at pH 6.0 (2). It is not known, however, if E1784K alters the movement of the channel voltage-sensors, or whether preferential depolarization of the GV curve by extracellular protons is matched by a preferential depolarization of voltage-sensor movement.

In this chapter, the results of experiments using the cut-open oocyte voltage-clamp procedure are reported. I record ionic and gating currents using a ‘background’ C373F mutant to increase channel sensitivity to tetrodotoxin (TTX) and allow for full channel block during gating current recordings (22). The intracellular pH was also measured during some recordings to test whether the changes to the biophysical properties of the channels are due to changes in extracellular pH or concurrent changes to

intracellular pH. I hypothesize that the depolarizing shift in the channel conductance curve in E1784K, and the greater depolarizing shift of conductance at low pH, are a direct result of depolarized gating charge movement.

2.2. Methods

2.2.1. DNA Constructs

The C373F construct in pPoll was used in a previous study from our lab and was generously donated by Dr. Mohamed Chahine (Laval University) (240). The E1784K point mutant was made by Ziwei Ding (Simon Fraser University) and was then cloned into 10 β *E. coli* cells (New England Biolabs, Ipswich, MA). The plasmid DNA was purified using a Qiagen Midi-prep kit (Qiagen, Hilden, Germany) and sequenced by Eurofin MWG Operon sequencing service (Eurofins Scientific, Luxembourg). I used NotI (NEB) to linearize both the C373F and C373F/E1784K DNA. Transcription was performed using a T7 mMESSAGE mMACHINE high yield capped RNA transcription kit (Ambion Inc., Foster City, CA).

2.2.2. Oocyte preparation

Female *Xenopus laevis* were obtained from Boreal Northwest (St. Catherines, Canada) and Nasco (Salida, CA). Frogs were housed in an AQUANEERING Xenopus Aquatic Housing System (Aquaneering Inc., San Diego, CA). Water temperature was maintained at 16-17 °C and frogs were fed either Nasco frog brittle or Boreal *Xenopus* food 3 times a week. Breeding was not performed at our facility.

All animal surgery and animal care procedures were performed in accordance with the policies of the Canadian Council of Animal Care. The protocols for this study were approved by the Simon Fraser Animal Care Committee (SFU Permit 1207K-07). All surgery was performed under Tricaine Methanesulfonate (2 g/L) anesthesia and confirmed by pinching of the hind leg. All efforts were made to minimize suffering. Euthanasia was confirmed by cervical dislocation and pithing of the brain.

The *X. laevis* oocyte preparation has been published previously (235). Oocytes were injected with 55 nL of purified Nav1.5 α -subunit RNA. For ionic current recordings, RNA was injected at concentrations between 100 ng/uL and 360 ng/uL. Ionic current experiments were performed within 24-72 h after injection. Gating currents were recorded between 96-120 h after injecting oocytes with 360 ng/uL RNA.

2.2.3. Data acquisition

Cut-open voltage clamp procedures were as described previously (247,248). We used a CA-1B amplifier (Dagan Corp., Minneapolis, MN) in the cut-open mode. Data were low pass-filtered at 10 kHz, digitized at 50 kHz, and recorded using Patchmaster (HEKA Elektronik, Lambrecht, Germany). Cells were permeabilized via bottom bath perfusion with intracellular solution supplemented with 0.1 % saponin. After a 10 – 60 s exposure, saponin-free intracellular solution was washed in.

For ionic current recordings, the extracellular solution contained (in mM): 96 NaCl, 4 KCl, 1 MgCl₂, 2 CaCl₂, and 5 HEPES. For ionic current recordings, the intracellular solution contained (in mM): 9.6 NaCl, 88 KCl, 11 EGTA, 5 HEPES. For gating current recordings, the extracellular solution at pH 7.4 contained (in mM): 117.7 NMDG, 122.3 MES, 10 HEPES, and 2 Ca(OH)₂; and the extracellular solution at pH 6.0 contained (in mM): 70 NDMG, 170 MES, 10 HEPES, and 2 Ca(OH)₂. The ratio of NMDG to MES was changed to make solutions at the correct pH of the same osmolarity. For gating current recordings, the intracellular solution contained (in mM): 120 NMDG, 120 MES, 10 HEPES, and 2 EGTA. MES was substituted in place of HEPES for all ionic solutions at or below pH 6.5. HCl and NMDG were used to titrate ionic solutions to the desired pH and MES and NMDG were used for gating current solutions.

Gating currents were recorded after addition of 20 uL of 50 uM TTX to the 0.5 mL top chamber yielding a final TTX concentration of ≈ 2 μ M. Data at low pH is matched in all cells to data at pH 7.4. In gating current experiments, TTX was applied after each replacement of the extracellular solution.

Intracellular pH recordings were made using a VE-2 amplifier in zero current mode (Alembic Instruments, Montreal, Canada). We filled pipettes with 3 M KCl solution, and backfilled with hydrogen ionophore solution. The hydrogen ionophore consisted of 6 wt.-% Hydrogen Ionophore II (Santa Cruz Biotechnology) and <1 wt.-% Potassium tetrakis(4-chloro-phenyl)borate dissolved in o-nitrophenol octyl ether. Immediately prior to recordings, the voltage response of the pH electrode was determined with solutions at pH 7.4 and pH 6.0. The average voltage change per pH unit in the electrodes was 46 ± 1 mV/pH unit.

Capacitance was compensated prior to recordings and leak was subtracted using either a P/4 or P/8 protocol.

2.2.4. Protocols

To measure the voltage-dependence of sodium conductance through the channel pore, I depolarized channels to voltages between -100 mV and +60 mV for 20 ms from a holding potential of -150 mV. Conductance was determined by dividing the peak current by the voltage minus the experimentally observed equilibrium potential. For comparisons of proton block I compared absolute conductance values while conductance-voltage relationship comparisons were performed with normalized conductance. GV relationships were fit by a single Boltzmann function (Equation 2.1)

$$\frac{Y}{Y_{Max}} = \frac{1}{(1 + e^{\frac{-z \cdot e \cdot (V_m - V_{1/2})}{K \cdot T}})} \quad (2.1)$$

where Y is conductance, charge, or current; V_m is membrane potential in mV; $V_{1/2}$ is the midpoint in mV; z is apparent valence in e (elementary charges); K is the Boltzmann constant in $\text{meV} \cdot \text{K}^{-1}$; and T is temperature in °K.

The proton block of conductance was measured by fitting conductance from individual cells recorded at pH values between 4.0 and 8.0 to a Hill equation.

Charge-voltage (QV) relationships were measured by 20 ms depolarizations to potentials between -150 mV and +40 mV from a holding potential of -150 mV. This was

followed by a 20 ms hyperpolarization to -150 mV. I measured the activation of the S4 segments by integrating the outward gating currents (I_{gon}) during the initial depolarization steps to give the amount of charge moved at a given membrane potential (QVon). I fit the resulting QV curve with a Boltzmann function. I fit the decay of the outward gating currents with a single exponential function to determine the rate of S4 segment activation.

To measure the voltage-dependence of fast inactivation I conditioned cells to voltages between -150 mV and -10 mV for 500 ms. After the conditioning pulse, currents were elicited by a depolarizing pulse to -10 mV. The peak currents were normalized and plotted versus conditioning potential. The resulting curves were fit by a single Boltzmann function (Equation 2.1).

I measured fast inactivation recovery with a double pulse protocol; following a 500 ms depolarization to 0 mV, channels were allowed to recover for varying lengths of time at potentials between -130 mV and -70 mV after which currents were measured by a pulse to -10 mV. Recovery time courses were fit by a double exponential function with the fast time constant being analyzed as the time constant of fast inactivation.

I measured open-state fast inactivation by fitting the decay of macroscopic currents with a single exponential function. The rate of fast inactivation from the closed state was measured by depolarizing cells to -70 mV or -50 mV for varying amounts of time from a holding potential of -150 mV. The amount of current remaining was measured during a test pulse to -10 mV and the normalized current versus onset time was fit by a double exponential function at -70 mV and a single exponential equation at -50 mV.

I measured non-inactivating current as the fraction of current remaining at the end of 100 ms depolarizations to voltages between -30 mV and 0 mV. To measure the fraction of channels that failed to inactivate, the non-inactivating current was divided by the peak inward current at the same potential to show relative non-inactivating current. Five traces were averaged for each measurement.

I measured the voltage-dependence of gating current deactivation by 20 ms repolarizations between 20 mV and -150 mV after a 20 ms depolarization to +50 mV. The amount of returning charge was assessed by integrating inward gating currents (I_{goff}) during the repolarizing pulse. Normalized charge was plotted versus voltage and fit with a Boltzmann function. Results were similar if gating charge return was measured by integrating outward gating currents during a depolarization to +50 mV immediately following the repolarization. The inverse of the returning charge is plotted in Figure 2.5.

I measured the rate of gating charge deactivation with a double pulse protocol. I depolarized cells for 500 ms to 0 mV and then repolarized the cell to -150 mV for varying lengths of time. The amount of charge returned during a given time period was measured by integrating an outward gating current elicited by a return pulse to 0 mV immediately following the repolarization. The time course of charge return was fit by a double exponential function

The voltage-dependence of slow inactivation was measured by holding cells for 60 s at membrane potentials between -130 mV and -10 mV, recovering fast inactivation at -130 mV for 20 ms, and measuring the remaining current with a test pulse to -10 mV. Steady-state slow inactivation was fit by a Boltzmann function (equation 2.1) with a non-zero asymptote.

Slow inactivation onset and recovery were measured using the same protocol. Currents were measured during a 5 ms pulse to -10 mV, followed by a depolarization to +30 mV, 0 mV, or -30 mV for between 500 ms and 64 s (0.5 s, 1 s, 2 s, 4 s, 8 s, 16 s, 32 s, 64 s), and a repolarization to -120 mV, -90 mV, or -80 mV for a total of 60 s. By measuring slow inactivation recovery and onset at different membrane potentials I determined whether any mutant or proton-dependent effects occur throughout the voltage range. Currents were measured at 10 time points after each depolarization pulse (0.02 s, 0.1 s, 0.25 s, 0.5 s, 1 s, 2 s, 5 s, 10 s, 20 s, 60 s). Onset at +30 mV, 0 mV, and -30 mV were matched to repolarizations at -120 mV, -80 mV, and -90 mV, respectively. The currents for a given set of recovery pulses were normalized to the current elicited before the depolarizing pulse. The 20 ms recovery pulse was not used in analysis as there are

still channels in the fast-inactivated state at that point. Slow inactivation recovery time courses at a given membrane potential were globally fit for all onset durations with a double exponential function where the two time constants were global variables. Slow inactivation onset time courses at a given membrane potential were fit globally for recovery durations of 100 ms to 10 s with a double exponential where the two time constants were global variables. Using this global fit method allows for more accurate determination of the time constants of recovery and onset as the time constants are determined from 8 recovery time courses or 7 onset time courses at each membrane potential.

2.2.5. Data analysis

Ionic and gating currents were analyzed using Fitmaster (HEKA) and Igor Pro (Wavemetrics). All statistical analysis was performed using JMP statistical software (SAS Institute, Cary, NC). Except for the midpoint of proton block of peak conductance, all comparisons were made using a 2 factor repeated measures analysis of variance where the main factors analyzed were pH (ordinal variable) and mutant (nominal variable). A significant interaction term between the two main factors was interpreted as a significant difference in the effect of protons on the dependent variable of C373F/E1784K compared to C373F channels. A TUKEY post-hoc test was used for pairwise comparisons of pH. For comparisons of time constants, the log of the time constants was compared. To compare proton block of conductance between C373F and C373F/E1784K channels I used a Student's t-test. Statistical significance was measured at $\alpha < 0.05$. For many cases where the same parameter was measured at multiple voltages (e.g. non-inactivating current) only the largest P-value (significant effects) or the smallest P-value (non-significant effects) is stated. All midpoint measurements are means and measurements of error listed are standard error of the mean.

2.3. Results

Source data for figures, including means, standard errors of the mean, and number of independent recordings, can be found in Appendix A.

2.3.1. Intracellular pH does not Change Along with Extracellular pH in Oocytes

A pH sensitive micro-electrode was used to measure the change in intracellular pH when extracellular pH was decreased in uninjected *Xenopus laevis* oocytes and oocytes injected with C373F (CF) or C373F/E1784K (CF/EK) Nav1.5 channels (Figure 2.1 A-C). Measurements of intracellular pH were recorded simultaneously with ionic current recordings at pH 7.4 and following perfusion of pH 6.0 extracellular solution. Similar to previously published experiments, peak sodium current is blocked at pH 6.0 (240). There is no significant change in the intracellular pH after 5 minutes exposure to pH 6.0 extracellular solution in the uninjected cells, nor in those injected with either channel construct ($P = 0.9760$) (Figure 2.1D).

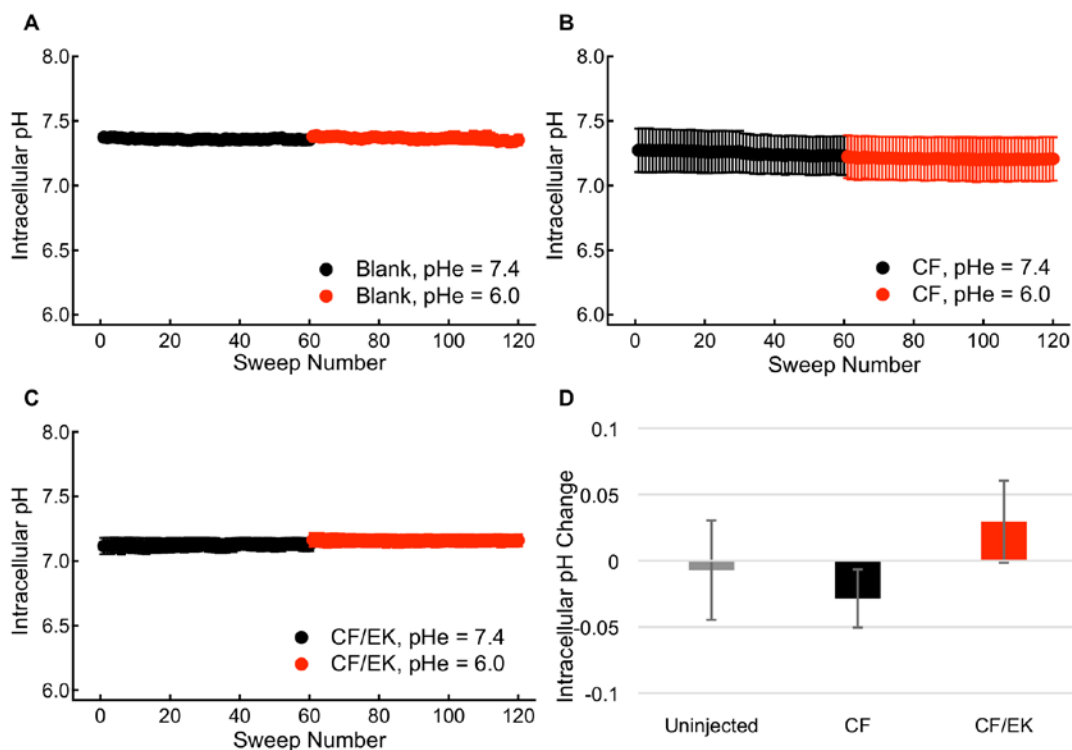


Figure 2.1. Intracellular pH is not Decreased by Decreases in Extracellular pH
Intracellular pH was measured for 5 minutes with extracellular pH at pH 7.4 and for 5 minute after changing extracellular pH to pH 6.0 in (A) un-injected cells ($N = 5$) and cells injected with (B) C373F ($N = 5$) or (C) C373F/E1784K ($N = 5$) Nav1.5. Cells were held at -110 mV and were depolarized to 0 mV 60 times during each 5-minute segment. All error bars are standard error of the mean. There was no significant change in the intracellular pH after 5 minutes at extracellular pH 6.0 (D). Previously published in Peters et al., 2017 (3).

2.3.2. E1784K Depolarizes the Conductance-Voltage Relationship and Hyperpolarizes Gating Charge Activation

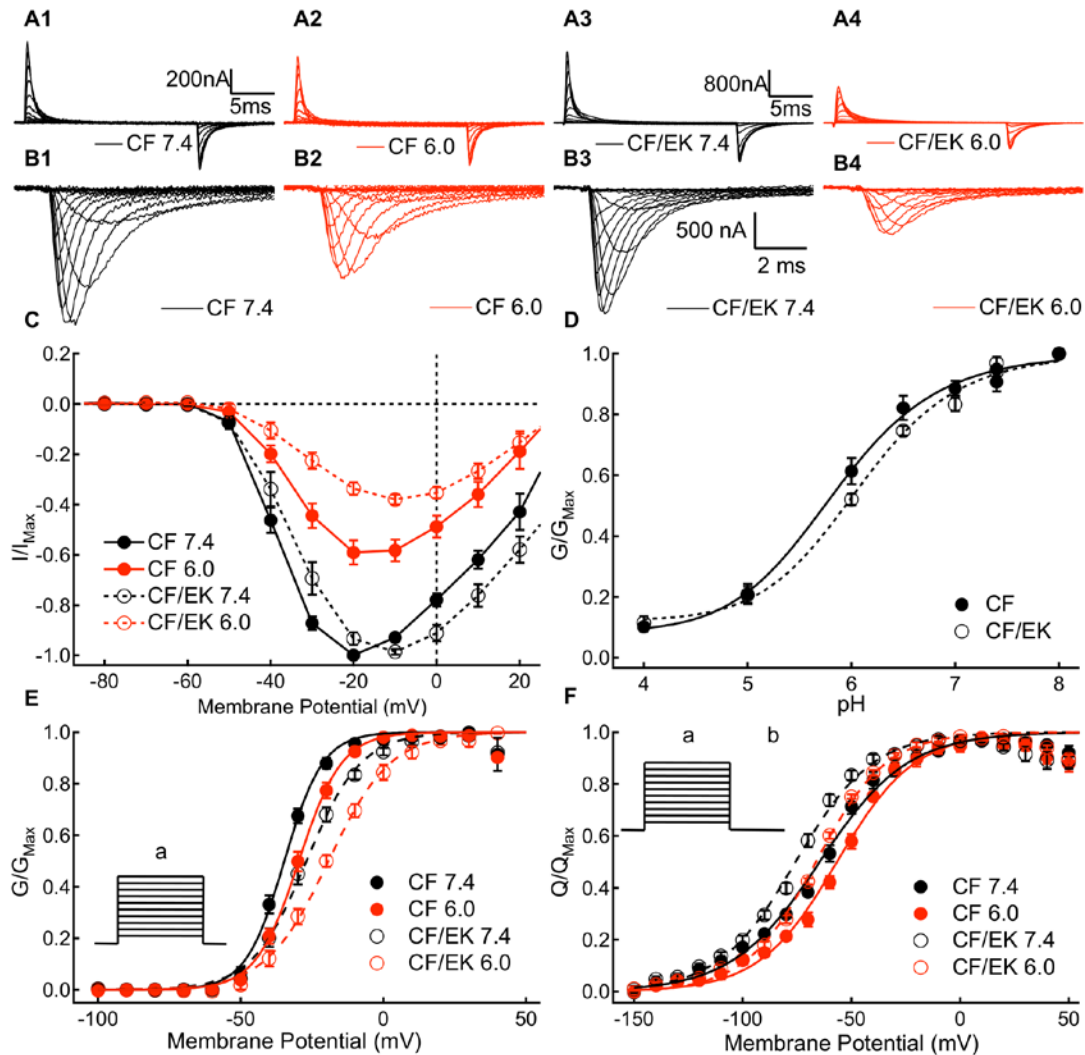


Figure 2.2. The E1784K Mutant Depolarizes the Conductance-Voltage Relationship and Hyperpolarizes Gating Charge Activation

(A1-A4) Sample outward and inward gating currents recorded from C373F and C373F/E1784K Nav_v1.5 at pH 7.4 and pH 6.0. (B1-B4) Sample ionic currents recorded from C373F and C373F/E1784K Nav_v1.5 at pH 7.4 and pH 6.0. CF and CF/EK currents with relatively similar amplitudes were selected to highlight the effects of protons. (C) Average normalized peak ionic current plotted versus voltage for C373F and C373F/E1784K Nav_v1.5 at pH 7.4 and pH 6.0. Currents at pH 6.0 are normalized to the peak current recorded at pH 7.4 from the same cell. (D) Average peak conductance plotted versus pH in C373F and C373F/E1784K Nav_v1.5. Conductance at all pH values is normalized to the peak conductance recorded from the same cell at pH 8.0. The pH at which conductance is reduced by 50% is shifted to higher pH in CF/EK channels. (E) Conductance-voltage relationships from ionic currents recorded in C373F and

C373F/E1784K Nav1.5 at pH 7.4 and pH 6.0. The E1784K mutant shifts the midpoint of the conductance-voltage relationship to more depolarized potentials. E1784K undergoes a larger depolarizing shift of the conductance curve when extracellular pH is lowered. (**E inset**) To measure current voltage relationships from which conductance was determined, cells were depolarized to membrane potentials between -100mV and +60 mV (a) from a holding potential of -150 mV. (**F**) Charge-voltage relationships for outward gating currents recorded from C373F and C373F/E1784K Nav1.5 at pH 7.4 and pH 6.0. The E1784K mutant shifts the midpoint of the charge-voltage relationship in the hyperpolarizing direction. (**F inset**) To measure gating current activation, cells were depolarized to membrane potentials between -150 mV and +40 mV (a) followed by a hyperpolarization to -150 mV (b). Previously published in Peters et al., 2017 (3).

I measured the voltage-dependence and rate of S4 voltage-sensor movement by recording outward and inward gating currents for CF and CF/EK channels at pH 7.4 and pH 6.0 (Figure 2.2 *AI-A4*). Channel conductance was measured by recording macroscopic ionic currents at membrane potentials between -100 mV and +60 mV (Figure 2.2 *BI-B4*).

I compared the dependence of peak currents and conductance in CF and CF/EK channels between pH 4.0 and pH 8.0. The current-voltage relationships for CF and CF/EK channels at pH 6.0 normalized to currents at pH 7.4 are shown in Figure 2.2*C*. The maximal conductance at all pH values normalized to the maximal conductance at pH 8.0 in the same cell is shown for CF and CF/EK channels in Figure 2.2*D*. There is a significant shift in the pKa of conductance block of CF/EK channels compared to CF channels ($P = 0.0149$).

I determined the voltage-dependence of sodium channel conductance in CF and CF/EK Nav1.5 channels at pH 7.4, 7.0, and 6.0 (Figure 2.2*E*). Both the presence of the E1784K mutant ($P = 0.0004$) and lowering extracellular pH to pH 7.0 and 6.0 ($P = 0.0253$ and $P < 0.0001$, respectively) cause a significant shift of the GV curve of CF Nav1.5 to more depolarized membrane potentials. The depolarizing shift due to decreases in pH is significantly larger in the CF/EK mutant than in CF ($P = 0.0374$). Both the E1784K mutant ($P = 0.0002$), and lowering extracellular pH to pH 6.0 from pH 7.4 ($P < 0.0001$), cause significant decreases in the apparent valence of the GV curve.

The total gating charge moved at a given voltage was determined by taking the time integral of the outward gating current during a depolarization step. Normalized outward charge versus voltage relationships (QV) were measured for C373F and C373F/E1784K at pH 7.4 and pH 6.0 (Figure 2.2*F*). Decreasing pH from pH 7.4 to pH

6.0 causes a significant shift in the midpoint of the QV relationship in the depolarized direction in both CF and CF/EK channels ($P < 0.0001$). Although E1784K causes a depolarizing shift in the midpoint of the GV curve, it causes a hyperpolarizing shift in the midpoint of the QV relationship ($P < 0.0001$). Thus, the voltage-sensors move outwards at more negative potentials in the mutant, but the channel does not conduct ions until more positive potentials.

The rate of outward gating charge movement was measured by fitting the decay phase of outward gating currents to a single exponential function (Figure 2.3A). E1784K does not significantly alter the rate of outward gating charge movement at most measured potentials ($P \geq 0.1368$ for 13 of the 15 measured voltages) (Figure 2.3B). Decreasing extracellular pH to pH 6.0 slows the rate of outward gating charge movement at all measured membrane potentials ($P \leq 0.0235$). There is no significant difference in the effect of protons on the rate of outward gating charge movement between CF and CF/EK channels at most measured membrane potentials ($P \geq 0.08011$ for 12 of 15 measured voltages)

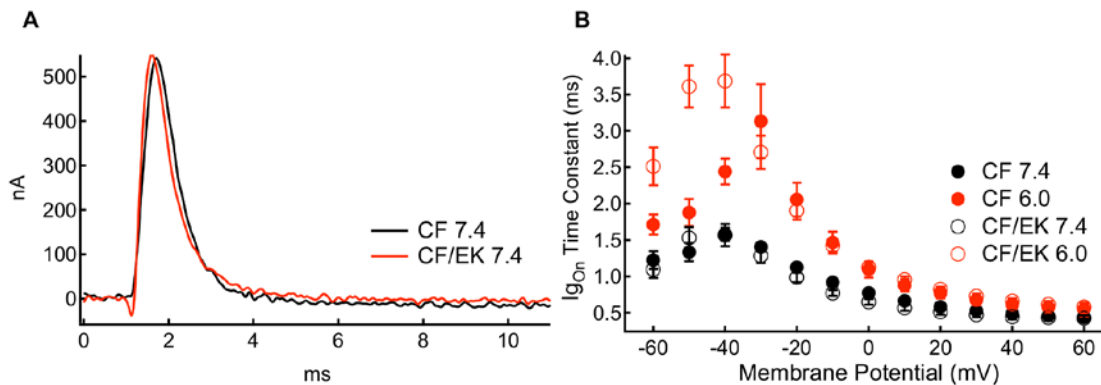


Figure 2.3. The E1784K Mutant does not Alter the Rate of Outward Gating Charge Movement at Depolarized Membrane Potentials

A: Outward gating currents recorded at 0 mV from CF and CF/EK channels at pH 7.4. The decay of outward gating currents was fit with a single exponential decay and the time constants are plotted in **B**. The E1784K mutant does not alter the rate of gating charge movement at the majority of membrane potentials whereas decreasing pH slows outward gating charge movement. Adapted from Peters et al., 2017 (3).

Contrary to my hypothesis, these results suggest the basis for the shift in the midpoint of the GV curve caused by E1784K is not due to a direct effect on the voltage-sensors responsible for activation.

2.3.3. E1784K Hyperpolarizes and Accelerates Fast Inactivation

I measured the voltage-dependence of fast inactivation in CF and CF/EK Nav1.5 channels using a test pulse to -10 mV following a 500 ms prepulse to membrane potentials between -150 mV and -10 mV (Figure 2.4 *A1-A4*). The normalized currents recorded during the test pulse are plotted versus prepulse potential in Figure 2.4*B*. The E1784K mutant causes a significant hyperpolarizing shift in the midpoint of the voltage-dependence of fast inactivation ($P = 0.0003$). Decreasing pH to 7.0 or 6.0 from pH 7.4 causes a significant depolarizing shift in the midpoint of the voltage-dependence of fast inactivation ($P = 0.0312$ and $P < 0.0001$, respectively). The shift in the voltage-dependence of fast inactivation to more hyperpolarized membrane potentials due to the E1784K mutant parallels the hyperpolarizing shift in the E1784K QV curve.

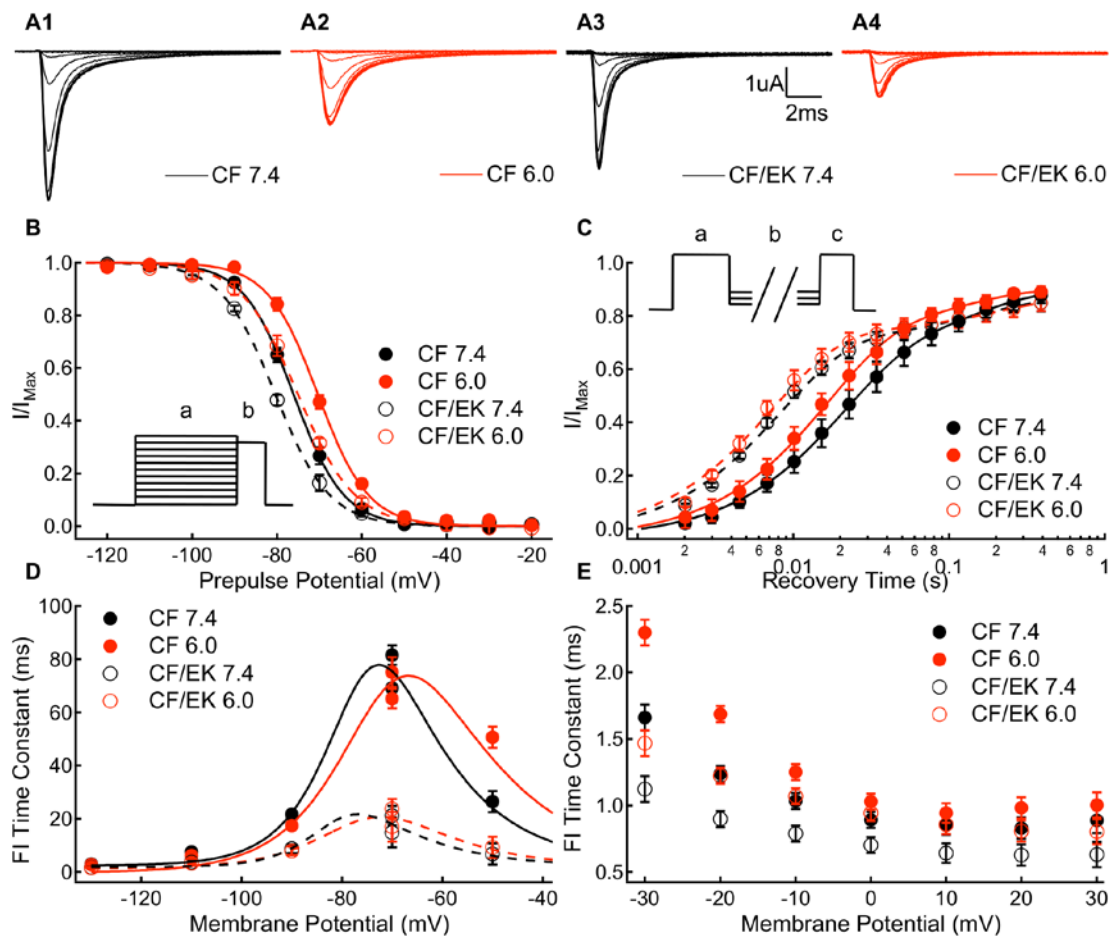


Figure 2.4. The E1784K Mutant Hyperpolarizes the Voltage-Dependence of Fast Inactivation

(A1-A4) Sample ionic currents elicited during steady-state fast inactivation recordings from C373F and C373F/E1784K $\text{Nav}_1.5$ at pH 7.4 and pH 6.0. (B) Steady-state fast inactivation relationships for C373F and C373F/E1784K $\text{Nav}_1.5$ at pH 7.4 and pH 6.0. The E1784K mutant shifts the midpoint of the fast inactivation voltage-dependence in the hyperpolarizing direction, whereas decreasing extracellular pH to pH 6.0 shifts the midpoint of the fast inactivation voltage-dependence to more depolarized membrane potentials. (B inset) To measure steady-state fast inactivation, cells were depolarized to -10 mV (b) following a conditioning pulse to membrane potentials between -150 mV and -10 mV (a). (C) Recovery from fast inactivation time course at -90 mV for C373F and C373F/E1784K $\text{Nav}_1.5$ at pH 7.4 and pH 6.0. The E1784K mutant accelerates recovery from inactivation. (C inset) To measure recovery from inactivation, cells were depolarized to -10 mV (c) following a conditioning pulse to 0 mV (a) and a recovery pulse of variable duration to membrane potentials between -130 mV and -70 mV (b). (D) Time constants of fast inactivation recovery (-130 mV to -70 mV) and closed-state fast inactivation onset (-70 mV and -50 mV) plotted versus voltage for C373F and C373F/E1784K $\text{Nav}_1.5$ at pH 7.4 and pH 6.0. The E1784K mutant accelerates fast inactivation recovery and closed-state fast inactivation onset at all potentials. (E) Time constants of open-state fast inactivation onset for C373F and C373F/E1784K $\text{Nav}_1.5$ at pH 7.4 and pH 6.0. The E1784K mutant accelerates open-state inactivation at all membrane potentials excluding +20 mV. Previously published in Peters et al., 2017 (3).

The time course of ionic current recovery from fast inactivation at -90 mV is plotted in Figure 2.4C. The time constants of fast inactivation recovery at voltages between -130 mV and -70 mV were measured as the faster time constant in bi-exponential fits to data like that found in Figure 2.4C. Similarly, the time constants of closed-state fast inactivation onset at -70 mV and -50 mV were measured as the faster time constant in bi-exponential fits to fast inactivation onset time courses. The fast time constants of fast inactivation recovery and closed-state onset are plotted versus membrane potential in Figure 2.4D. E1784K significantly decreases the fast time constants of fast inactivation recovery at -130 mV, -110 mV, -90 mV, and -70 mV ($P < 0.0001$ in all cases). E1784K also significantly decreases the time constant of closed-state fast inactivation onset at -70 mV and -50 mV ($P < 0.0001$ in both cases). Lower extracellular pH significantly decreases the fast time constant of fast-inactivation recovery at -110 mV ($P = 0.0002$) and -90 mV ($P = 0.0054$) and increases the time constant of closed-state fast inactivation at -50 mV ($P < 0.0001$).

The time constants of open-state fast inactivation were determined by fitting mono-exponential equations to ionic current decay. The time constants of open-state fast inactivation onset are plotted versus voltage in Figure 2.4E. E1784K decreases the time constant of open-state inactivation at voltages between -40 mV and 30 mV, excluding at +20 mV ($P < 0.044$ for all cases, except at +20 mV $P = 0.0763$). Thus, the E1784K mutant accelerates both entry into and recovery from the fast-inactivated state. Lower extracellular pH significantly increases the time constant of open-state fast inactivation between -40 mV and +30 mV ($P < 0.0408$).

2.3.4. E1784K Increases Non-Inactivating Current

I measured absolute (Figure 2.5A) and relative (Figure 2.5A *inset*) non-inactivating current amplitudes in CF and CF/EK Nav1.5 channels at pH 7.4, 7.0, and 6.0 at membrane potentials between -30 mV and 0 mV. The CF/EK mutant has a significantly larger proportion of non-inactivating current compared to CF channels at all membrane potentials ($P \leq 0.0018$) (Figure 2.5B). Low pH significantly increases the relative non-inactivating current more in the CF/EK mutant compared to CF channels at

all membrane potentials ($P \leq 0.0002$). Thus, whereas CF channels have a relatively similar fraction of non-inactivating current at -20 mV at pH 7.4 and pH 6.0 (0.45 % and 0.43 %, respectively), the CF/EK channels have a 2.5 % increase in non-inactivating current from pH 7.4 to pH 6.0 at -20 mV (4.0 % and 6.5 %, respectively). The CF/EK mutant also increases the absolute non-inactivating current at all membrane potentials ($P \leq 0.0058$).

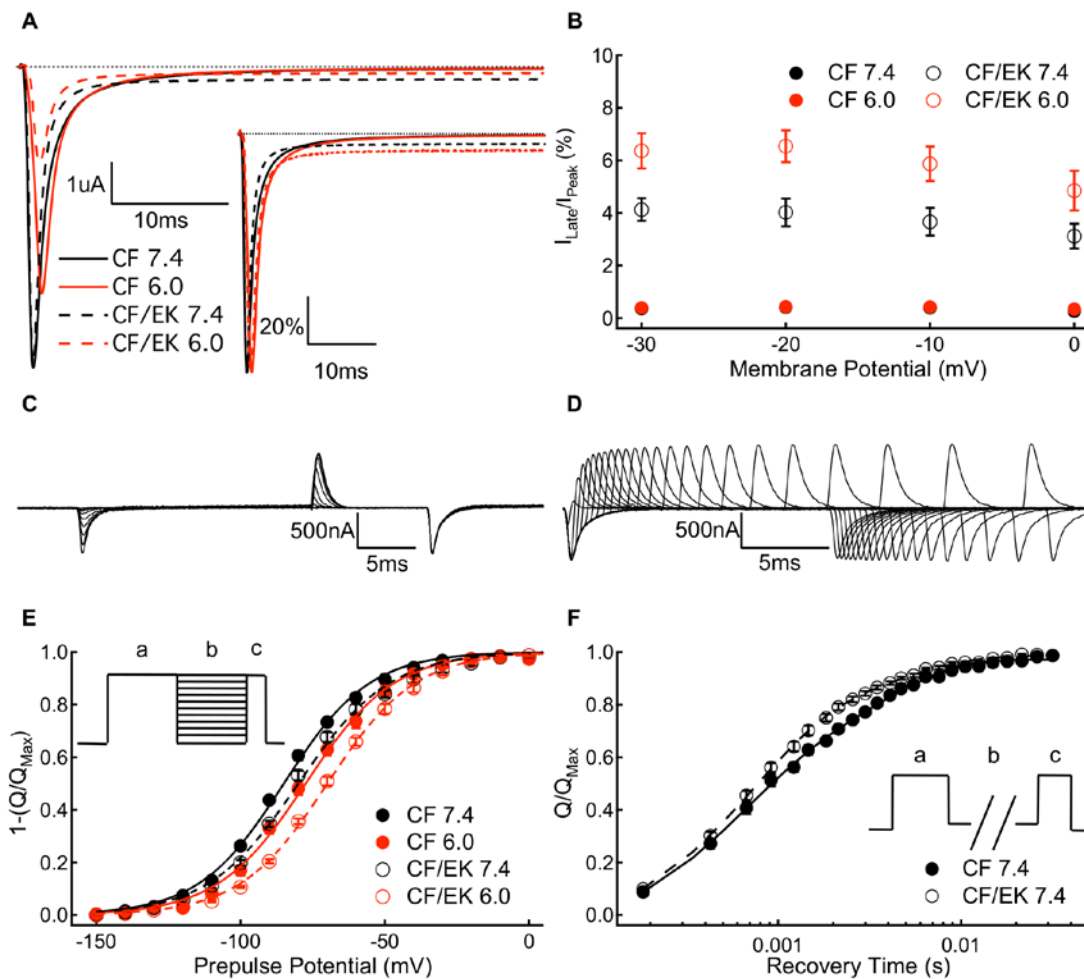


Figure 2.5. The E1784K Mutant Increases Non-Inactivating Current and Depolarizes the Voltage-Dependence of Gating Charge Deactivation

(A) Sample persistent sodium current recordings at -20 mV from C373F and C373F/E1784K $\text{Na}_v1.5$ at pH 7.4 and pH 6.0. (A *inset*) Sample persistent sodium current recordings at -20mV normalized to peak current from C373F and C373F/E1784K $\text{Na}_v1.5$ at pH 7.4 and pH 6.0. (B) Persistent current normalized to peak current for C373F and C373F/E1784K $\text{Na}_v1.5$ at pH 7.4 and pH 6.0 at membrane potentials between -30 mV and 0 mV. The E1784K mutant increases the fraction of persistent current. When extracellular pH is lowered to pH 6.0 there is a larger increase in the fraction of persistent current in CF/EK compared with CF. (C) Sample gating currents recorded during a protocol to measure gating current deactivation voltage-

dependence. **(D)** Sample gating currents recorded to measure the time course of voltage-sensor deactivation at -150 mV. **(E)** Voltage-dependence of gating current deactivation for C373F and C373F/E1784K $\text{Na}_v1.5$ at pH 7.4 and pH 6.0. The inverse of the amount of charge deactivating at a given voltage is plotted to facilitate comparisons with the outward charge-voltage relationship. The voltage-dependence of gating current deactivation is shifted in the depolarizing direction by the E1784K mutant. **(E inset)** To measure the voltage-dependence of gating current deactivation, cells were hyperpolarized to membrane potentials between -150 mV and +20 mV (b) following a depolarization pulse to +50 mV (a). This was followed by depolarization to +50 mV (c). **(F)** Time course of gating charge deactivation at -150 mV for C373F and C373F/E1784K $\text{Na}_v1.5$ at pH 7.4. Time courses at pH 6.0 overlap those recorded at pH 7.4 and are therefore not shown. The E1784K mutant increases the fraction of charge which recovers with the fast time constant of recovery and decreases the fraction of slow charge return. **(F inset)** To measure the rate of gating current deactivation, we depolarized cells to 0 mV (c) following a conditioning pulse to 0 mV (a) and a recovery pulse of variable length to -150 mV (b). Previously published in Peters et al., 2017 (3).

2.3.5. E1784K Depolarizes Voltage-Sensor Deactivation

The voltage-dependence of inward gating charge movement, or gating charge deactivation, was measured by integrating inward gating currents at membrane potentials between +20 mV and -150 mV after depolarizing pulses to move the S4 segments to their activated conformation (Figure 2.5C). Similar results were obtained when the amount of charge deactivation was measured by integrating outward gating currents at +50 mV immediately after the test pulse. To facilitate comparison with activating gating currents, the inverse of the total inward charge is plotted versus voltage (Figure 2.5E). Thus, like the outward charge-voltage relationships, the deactivation voltage-dependence represents how much gating charge is in the outward conformation. In contrast to the shift in the midpoint of the activation QV relationship to more hyperpolarized membrane potentials, E1784K causes a significant depolarizing shift in the voltage at which gating charge deactivates ($P = 0.0007$).

I measured the rate of gating charge deactivation at -150 mV (Figure 2.5D). The amount of gating charge that has deactivated for a given recovery time is plotted in Fig 3F and is fit by a bi-exponential equation. The fast and slow time constants of deactivation are not significantly altered by E1784K ($P = 0.0812$ and $P = 0.1809$, respectively). In the CF/EK channels the amplitude of the fast time constant is significantly increased and the amplitude of the slow time constant is significantly decreased compared to CF channels ($P = 0.0012$ and $P = 0.0082$, respectively). Thus, the overall rate of gating charge deactivation is accelerated by the E1784K mutant.

2.3.6. E1784K does not Impact Slow Inactivation Voltage-Dependence

I measured the voltage-dependence of slow inactivation in CF and CF/EK channels using a 60 s prepulse to membrane potentials between -130 mV and -10 mV (Figure 2.6A). Current amplitude was assessed during a subsequent step depolarization to -10 mV. E1784K does not cause a significant change in the voltage-dependence ($P = 0.7824$), asymptote ($P = 0.1690$), or apparent valence ($P = 0.9071$) of slow inactivation; however, extracellular acidosis causes a significant depolarization of slow inactivation in both CF and CF/EK channels ($P = 0.0003$).

2.3.7. E1784K Accelerates Slow Inactivation Onset and Recovery

Slow inactivation onset and recovery were measured in CF and CF/EK channels using a multiple pulse protocol with slow inactivation onset durations between 500 ms and 64 s and recovery durations between 20 ms and 60 s (Figure 2.6 *B1* and *B2*). The resulting slow inactivation recovery and onset curves were fit with double exponential functions (Figure 2.6*C* and Figure 2.6*D*, respectively). The exception was at +30 mV where only a single time component of slow inactivation could be fit. The currents recorded after 20 ms of recovery were not used in this analysis as many channels were still fast inactivated at that time, based on the time constants from our fast inactivation recovery experiments. The fast and slow time constants of slow inactivation recovery and onset are plotted versus voltage in Figure 2.6 *E* and *F*, respectively.

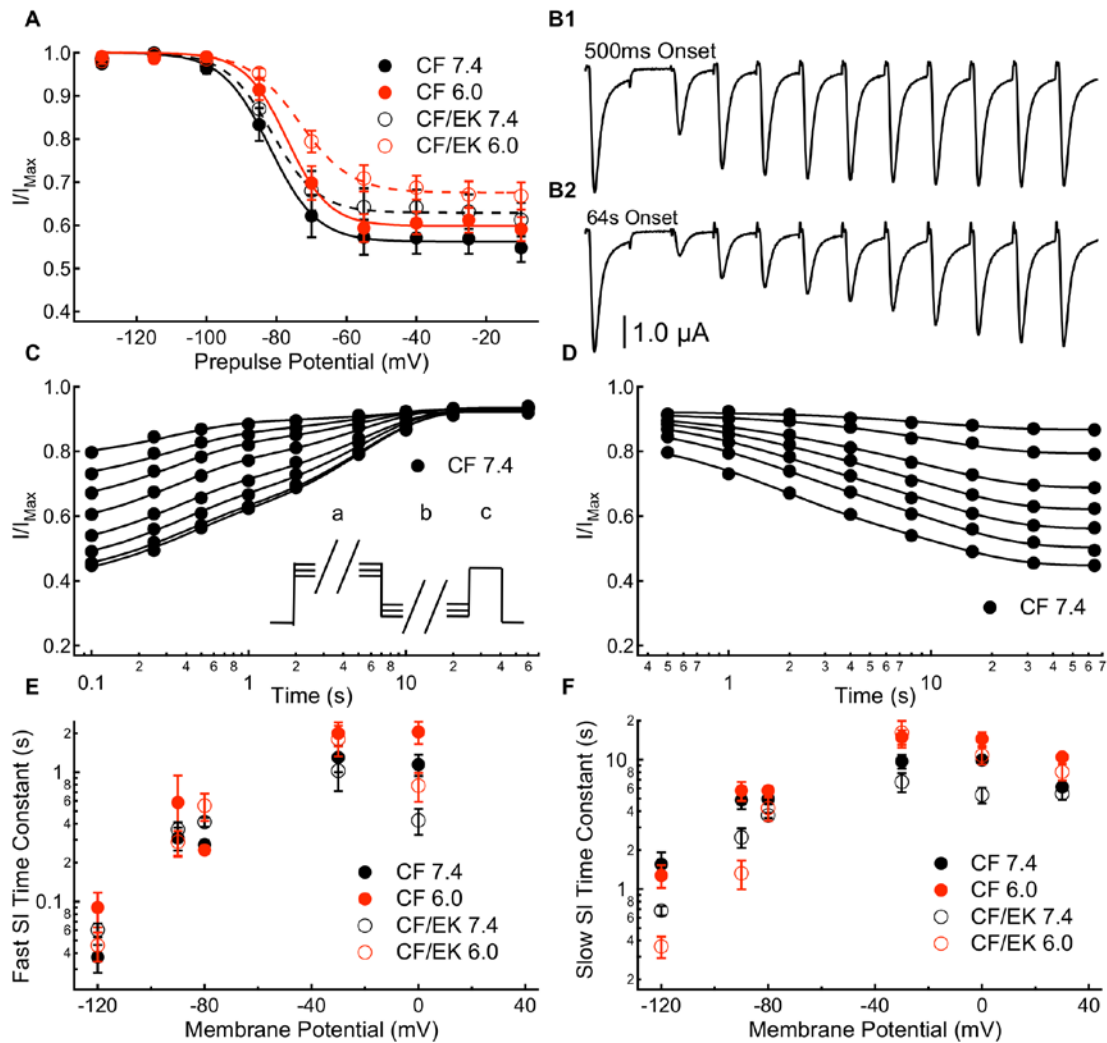


Figure 2.6. The E1784K Mutant Accelerates a Slow Time Component of Slow Inactivation

(A1) Voltage-dependence of slow inactivation in C373F and C373F/E1784K Nav_v1.5 at pH 7.4 and pH 6.0. Decreasing extracellular pH to pH 6.0 depolarizes the midpoint of low inactivation and increases the asymptote reflecting maximal slow inactivation onset. (B1 and B2) Sample inward sodium currents recorded after 20 ms to 60 s repolarization pulses to -90 mV following either a 500 ms or 64 s depolarization to -30 mV. (C) Time course of slow inactivation recovery at -90 mV in C373F Nav_v1.5 at pH 7.4 following depolarizations to -30 mV for durations between 500 ms (top curve) and 64 s (bottom curve). (C inset) To measure onset and recovery time courses for slow inactivation, cells were depolarized to -10 mV (c) following a depolarizing pulse of variable duration to membrane potentials between -30 mV and +30 mV (a) and a recovery pulse of variable duration to membrane potentials between -120 mV and -80 mV (b). (D) Time course of slow inactivation onset at -30 mV in C373F Nav_v1.5 at pH 7.4 with recovery interpulses to -90 mV for durations between 100 ms (bottom curve) and 10s (top curve). (E) Time constants for the fast component of slow inactivation recovery (-120 mV to -80 mV) and slow inactivation onset (-30 mV and 0 mV) plotted versus voltage for C373F and C373F/E1784K Nav_v1.5 at pH 7.4 and pH 6.0. The E1784K mutant decelerates the fast component of inactivation recovery at -80 mV and accelerates inactivation at 0 mV. Decreasing extracellular pH slows the fast component of inactivation onset at 0 mV. (F) Time constants for the slow component of slow inactivation recovery (-120 mV to -80 mV) and slow inactivation onset (-30 mV to 30 mV) plotted versus voltage for C373F and C373F/E1784K Nav_v1.5 at pH

7.4 and pH 6.0. The E1784K mutant accelerates the slow component of recovery at -120 mV and -90 mV and accelerates the slow component of onset at 0 mV. Decreasing extracellular pH slows the slow component of inactivation onset at -30 mV, 0 mV, and +30 mV. Adapted from Peters et al., 2017 (3).

The recovery of the fast component of slow inactivation is slowed in the CF/EK mutant at -80 mV ($P = 0.0149$) whereas the fast component of slow inactivation onset at 0 mV is significantly accelerated in the CF/EK mutant compared to CF ($P = 0.0052$). The mutant effect on the fast component of slow inactivation recovery was not significant at other voltages (-120mV: $P = 0.1168$, -90mV: $P = 0.7984$, -30mV: $P = 0.7962$). The slow component of slow inactivation recovery and onset is accelerated in E1784K at -120 mV, -90 mV, and 0 mV ($P = 0.0017$, $P = 0.0397$, and $P = 0.0030$) while at -80 mV and -30 mV a non-significant trend was seen ($P = 0.0945$, $P = 0.0865$). In total, these data suggest that E1784K primarily accelerates the rate of a component of slow inactivation onset and recovery in the 1-10 s range.

Decreasing extracellular pH significantly slows the fast component of slow inactivation onset at 0 mV ($P = 0.0029$) and the slow component of slow inactivation onset at -30 mV ($P = 0.0169$), 0mV ($P = 0.0009$), and +30 mV ($P < 0.0001$). Decreasing extracellular pH does not significantly affect the fast component of slow inactivation recovery at any membrane potential ($P \geq 0.6884$). In contrast, decreasing extracellular pH causes a non-linear effect on the slow component of slow inactivation recovery at -120 mV, -90 mV, and -80 mV. In all cases the slow recovery time constant was slowest at pH 7.0 compared to pH 7.4 and pH 6.0. The changes to the slow component of recovery were consistent in CF and CF/EK channels. Since time constants reflect both the forward and reverse rates of slow inactivation, it is possible that one rate is affected by a change to pH 7.0 whereas the other is not affected until pH reaches 6.0. Overall, these data suggest that decreases in extracellular pH primarily impacts slow inactivation in the 1-10 s range as opposed to the range less than 1 s.

2.4. Discussion

The E1784K mutant in Nav1.5 is the most common LQT3 and Brugada syndrome mutant and is sensitive to extracellular acidosis (2,249,250). Acidosis is a common factor

in a number of scenarios which can elicit arrhythmia and sudden cardiac death, including sudden infant death syndrome, exercise, cocaine ingestion, and ischemic heart disease (200,205,208,210,251). During myocardial ischemia extracellular pH may drop as low as pH 6.0, while exercise can produce decreases to pH 7.0-7.2 (215,252,253). Since arrhythmias associated with E1784K potentially arise during these acidotic conditions, we further investigated how E1784K modifies channel gating at physiologically normal pH (pH 7.4) and during extracellular acidosis (pH 7.0 and 6.0).

Consistent with my previous study, I show that extracellular acidosis produces a larger depolarization of the GV curve and a larger proton-dependent block of inward sodium currents in E1784K (2). When extracellular pH was decreased from pH 7.4 to pH 6.0 the depolarizing shift in the GV curve is twice as large (≈ 8.5 mV) in the CF/EK Nav1.5 compared to CF Nav1.5 (≈ 4 mV). The larger depolarizing shift seems to be limited to extracellular acidosis below pH 7.0 as both CF and CF/EK channels saw similar (≈ 1.8 mV) shifts when pH was decreased to pH 7.0. The effect was similar when looking at proton-dependent decreases in channel conductance as CF and CF/EK Nav1.5 show relatively similar effects at pH 7.0, 3 % block in CF and 1 % in CF/EK, when compared to the block at pH 6.0, 26 % in CF and 37 % in CF/EK. Overall these results suggest that small decreases in pH, such as during exercise, will not preferentially alter function in patients with the E1784K mutant; however, as pH decreases below pH 7.0, as might occur during ischemia, the CF/EK mutant will show drastically larger decreases in sodium channel conductance compared to CF Nav1.5. In patients, these changes could exacerbate the decreases in peak current found with the E1784K mutant, potentially increasing the risk of arrhythmia or sudden cardiac death.

A simple explanation for the depolarization of the conductance curve in the E1784K mutant would be a depolarizing shift in the voltage at which S4s translocate. The gating current experiments show that this hypothesis is unlikely to be true, since the activation QV relationship is hyperpolarized in the CF/EK mutant compared to CF, nor is there a preferential effect of protons on the E1784K QV relationship.

Hyperpolarization of the QV curve may reflect the E1784K-induced hyperpolarizing shift in the steady-state fast inactivation curve, which is tied to the movement of DIVS4. I conclude that the shifts in the channel conductance curve in the E1784K mutant are not due to changes in the movements of the DI-DIII S4s linked to channel activation (53). Instead, I hypothesize that the changes in conductance are due to the increased rates of DIVS4 movement, which leads to an increased rate of channel fast inactivation (20). This increased rate of fast inactivation could decrease the amplitude of inward currents at potentials in the middle of the conductance curve when the activation rate is lower, causing a shift in the channel conductance that is unrelated to DI-DIII voltage-sensor movements. This hypothesis is tested with a voltage-sensor-based model of ionic currents in the subsequent chapter.

Interestingly, the data show that the voltage-dependence of gating current deactivation is depolarized in E1784K. The result is that the large hysteresis between voltage-sensor activation and deactivation observed in CF channels is not apparent in CF/EK channels. This may reflect the decreased stability of the fast-inactivated state, which normally immobilizes a fraction of the gating charge in the activated conformation (71,72). This idea is consistent with the decreased amplitude of the slow component of gating charge deactivation we observed in CF/EK channels, which represents a decrease in the amount of immobilized charge. Overall, these results, and the increased rate of fast inactivation recovery suggest a lower energy barrier for the deactivation of the DIVS4. Therefore, a small fraction of the DIVS4 voltage-sensors may be able to deactivate at depolarized potentials leading to fast inactivation recovery and the increases in non-inactivating current in the E1784K mutant.

Similar to other studies, the data show that E1784K increases non-inactivating current (2,134,146). Relative non-inactivating current is further increased at pH 6.0 in the CF/EK channels, while it is relatively similar in CF Nav1.5 at pH 7.4 and pH 6.0. This suggests a decrease in the stability of the fast-inactivated state in E1784K that is further exacerbated by acidemia. This decreased stability may reflect a less stable binding by the IFM motif or the accelerated fast inactivation recovery rate in E1784K. Although extracellular acidosis decreases the absolute peak and non-inactivating current

amplitudes, non-inactivating current is more resistant to these changes than is peak current, hence the increase in relative non-inactivating current. Thus, while low pH will block sodium channels and increase the likelihood of conduction abnormalities in patients carrying the E1784K mutant, this blockade may not sufficiently reduce non-inactivating currents to alleviate the elongated AP plateau.

The slow inactivation experiments showed that E1784K primarily accelerates the slow component of onset and recovery in the range of 1-10 s. One possible mechanism for this could be a decrease in the stability of the fast-inactivated state. Previous studies show that removing fast inactivation enhances entry into the slow inactivated state in cardiac sodium channels (86). Thus, the changes to slow inactivation in E1784K may reflect a less stable interaction between the channel and the DIII-DIV linker. I speculate that the acceleration of both onset and recovery from slow inactivation means there will be little effect on channel availability at resting heart rates. Although channels will enter the slow inactivated state more rapidly during the action potential plateau, the long diastolic time and accelerated recovery rate will be sufficient to recover this extra slow inactivation; however, as heart rate increases, the diastolic interval represents a smaller proportion of each cycle. Therefore, the increased slow inactivation in E1784K may not fully recover at elevated heart rates which would decrease the number of available sodium channels further decreasing peak sodium current.

The slow inactivation experiments did not show preferential effects of acidosis in E1784K; however, there is an interesting effect on both CF and CF/EK channels in which the time constants of the slow component of recovery decreased at pH 7.0, but not pH 6.0. This time constant not only reflects the forward and reverse rates of slow inactivation but, if slow inactivation is tied to a voltage-sensor relaxation step from the active position as has been previously suggested, it is also likely to be influenced by the activation and deactivation rates of the DI-DIII voltage-sensors (88,89). This makes interpreting this phenomenon difficult. One possibility is that the one of the rates is altered at pH 7.0, while the other is not affected until pH 6.0.

Overall, these results show profound effects of extracellular acidosis on the ionic currents and suggest that the mechanism by which E1784K alters channel function is tied primarily to the fast inactivation mechanism. This finding is consistent with the location of the mutant in the C-terminus, a region shown to interact with the DIII-DIV linker and to play a key role in determining the rates of fast inactivation (46,74). This hypothesis is investigated in the subsequent chapter.

Chapter 3. Chapter 3: E1784K Regulates Channel Fast Inactivation

3.1. Introduction

The E1784K mutant in the cardiac voltage-gated sodium channel Nav1.5 is the most common LQT3-linked mutant (134). The mutant is found with a particularly high prevalence on the island of Okinawa where a study on children found that LQT3 was the most prevalent LQT subtype and all that all children with LQT3 variants carried the E1784K mutant (136). The mutant is also linked to Brugada syndrome and patient ECGs may show a Brugada syndrome waveform and an elongated QT interval simultaneously. For these reasons, E1784K is classified as a mixed syndrome mutant (134,243).

Data in the previous chapter show that the depolarizing shift in the voltage-dependence of channel conductance occurs in the absence of a depolarized charge-voltage relationship. Thus, the shifts in channel activation and the preferential depolarization of conductance by extracellular acidosis in E1784K are not explained by a simple depolarization in the movement of the S4 voltage-sensing segments. Instead, I hypothesize that the effects of E1784K on channel conductance and gating-charge movement can be explained by the modified fast inactivation of E1784K. To test this hypothesis, I developed a new sodium channel model that expands the Hodgkin and Huxley (HH) model to include multiple movement of the individual gates which can be directly related to movements of the 4 voltage-sensing domains (8).

The simplicity of the HH model makes it computationally efficient, but its usefulness is limited in the face of increasing data on the biophysical and structural properties of sodium channels. Data accumulated since the original formulation of the HH model show that the movements of the 4 voltage-sensors likely involve multiple voltage-dependent activation steps and, as discussed below, at least one voltage-independent step (19,254). Furthermore, the channel enters multiple slow inactivated

states that are not well accounted for by the HH model (85,88). Markov-type models address a number of these problems, simultaneously increasing the necessary computational power and the complexity (255). For example, the Clancy-Rudy model uses nine states, but operates under the assumption that the activation voltage-sensors are either equivalent or ordered in their activation sequence (256). Equivalent voltage-sensors are not supported by fluorescence data which show: 1) different midpoints of activation for the different voltage-sensors; 2) DIIS4 carrying 50 % more charge than DIS4 or DIIS4; 3) immobilization of DIIS4, but not DIS4 or DIIS4, by fast inactivation; and 4) changes in the slope of the conductance curve as holding potential is changed (53,71,72,257,258). Ordered transitions are not supported by fluorescence data that show no lag in the activation of any of the DIS4, DIIS4, or DIIS4 movements (53). A model that separates the motion of DIIS4 from DIS4 and DIIS4 is the 19 state Armstrong model, however, the Armstrong model does not include slow inactivation (259).

If the 4 voltage-sensors are all assumed to differ from one another and do not activate in a particular order, then a Markov model of deactivation and activation of the voltage-sensors, with no consideration of any inactivation step, would require 2^4 (16) states. If, similar to potassium channels and consistent with the non-zero asymptote of the rates of channel activation and gating charge movement, the movements of the voltage-sensing segments are modeled with a voltage-independent transition prior to voltage-dependent activation, the necessary number of states to model the 4 voltage-sensors is 3^4 (81) (53,73,260). Recent evidence suggests that relaxation movements of the voltage-sensors during prolonged or repetitive depolarizations underlies the slow inactivation of currents (88,89). Incorporating a single relaxation step in the first 3 voltage-sensors and a single voltage independent transition tied to the DIVS4 voltage-sensor for binding of the DIII-DIV fast inactivation particle yields a Markov model with 4^4 (256) states.

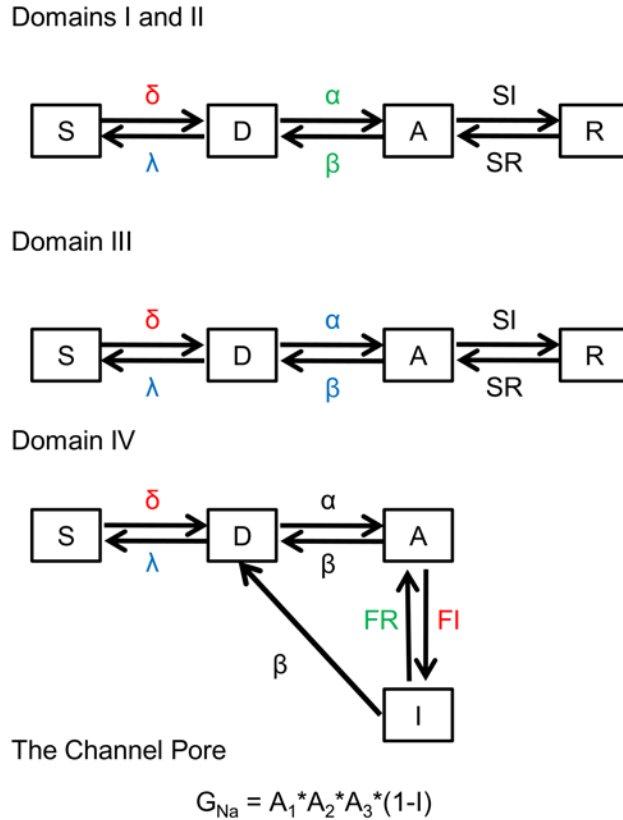


Figure 3.1. The Peters-Ruben Model of Voltage-Gated Sodium Channel Gating
 Schematic of the Peters-Ruben model of $Na_v1.5$. The movement of the four voltage-sensors is calculated independently and the channel pore is modelled based on the position of the individual voltage-sensors. Rates colored red are voltage-independent rates with values directly derived from experimental data. Rates colored black are voltage-dependent rates directly fitted from experimental data. Rates colored green are fitted to minimize the deviation between simulated currents and experimental data. Rates colored blue are ones to which the model is relatively insensitive. Adapted from Peters et al., 2017 (3).

As more and more states are incorporated the computational power necessary to solve the model increases along with the number of seldom- or never-occupied states that theoretically exist. As opposed to the general 256 state Markov model, I propose using a voltage-sensor activation model in which the state of every voltage-sensor is calculated independently, like the HH model. In this model, the probability of pore opening is calculated based on the states of the voltage-sensors. The proposed scheme (Figure 3.1) is composed of 16 states, and includes 4 positions for each of the voltage-sensors. In the first 3 voltage-sensors these positions are: stable (S), deactive (D), active (A), and relaxed (R). In the fourth voltage-sensors these positions are: stable (S), deactive (D), active (A), and Inactive (I). The pore is open when the first three voltage-sensors move to their

active conformation (53,72). Fast inactivation of the channel is modelled as a voltage-independent movement of the inactivation particle following DIVS4 activation (20,67,72). The conductance of the pore can then be calculated similarly to the Hodgkin and Huxley model (Equation 3.1).

$$G_{Na} = A_I * A_{II} * A_{III} *(1-I). \quad (3.1)$$

The results that follow show that this model accurately simulates both ionic and gating currents of the cardiac voltage-gated sodium channel, Nav1.5, with rates obtained from experimentally recorded data. The model also allows for prediction of how the channel is affected by the E1784K mutant. When only the rates of DIVS4 movement are altered with data from E1784K experiments, the mutant effects on fast inactivation, activation, non-inactivating current, and gating charge movement can be replicated. The hypothesis that the effects of the E1784K mutant on the QV and GV relationships are due to altered fast inactivation is supported by experiments with fluorophore tagged DIVS4 movement and experiments with the fast inactivation deficient IFM/QQQ mutant.

3.2. Materials and Methods:

3.2.1. Modeling

All models were run in python on an iMac computer. Graphing and analysis were done using IGOR Pro. Changes in the voltage were simulated as an exponential time course to match the time course of voltage change in our experiments. The time constants of voltage change in our experiments were determined by fitting the decay of capacitive transients from ionic current or gating current recordings.

Data from our ionic and gating current recordings were used to fit the rates of the 4 individual voltage-sensors in the modeling scheme shown in Figure 3.1. The forward voltage-independent rate between the S and D states for all voltage-sensors (DI-DIV δ) is the maximal rate of outward gating charge movement. The asymptote of the experimentally measured outward gating current decay (Figure 2.3B) at positive membrane potentials was used for this variable. If this value is changed, the maximal

rate of the simulated outward gating charge movement is altered. The reverse D to S transition (λ) was ten times the forward rate (δ). This rate cannot be derived from our experimental data and simulations of ionic and gating currents are relatively insensitive to higher rates for this transition. The reason for using ten times the forward rate is explained in the discussion section.

The D to A transition rates for the first 3 voltage-sensors (DI-DIII α and β) were derived from the time constants of outward gating charge motion (Figure 2.3B). Initially, the forward and reverse rates in all three voltage-sensors were fit with the same equation, which produced recognizable sodium currents (Figure 3.7A). To provide an accurate fit of ionic currents, a genetic algorithm was used to minimize the deviation between simulated ionic currents and averaged experimental currents (261). This algorithm was performed with the constraint that the first and second voltage-sensors are equivalent and therefore their motion can be fit by the same parameters. The genetic algorithm is based on the principals of natural selection for a population under a selective pressure. The first generation of 200 individuals was constructed randomly. Each individual was given a value for the amplitude and voltage-dependence of the α and β rates for each of DI and DIII (the DII rates are the same as DI). Thus, each individual is defined by a set of 8 values. The values were assigned randomly based on normal distributions centered at the values derived from fitting the time course of outward gating charge movements in the experiments from chapter 2. Individuals were grouped randomly in sets of four and current-voltage relationships were simulated for each individual. The two individuals which less accurately simulated the experimental data, as measured by a greater sum of squared deviations, were discarded. The two more accurate individuals were used to construct 4 individuals in the next generation (offspring) and then discarded. For each of the 8 values, the offspring had a 90 % chance of inheriting a value from a parent (45 % for each parent) and a 10 % chance of getting a random value based on a normal distribution centred on the value from the best individual discovered by the algorithm to that point. The algorithm was continued until 50 generations failed to produce a better individual than the best one previously found. The resulting best individual was then optimized using a climbing hill algorithm. The outcome of the two algorithms was a hyperpolarizing shift in the steady-state activation of DIII and relatively little change in

the rates of DI and DII. Changes to either of the DI or DII α or β rates alter the simulated conductance-voltage relationship. The DIII rates can be shifted to more hyperpolarized potentials with minimal impacts on the simulated conductance-voltage relationship. This is discussed in the discussion section of this chapter as well as the updated model section of chapter 5.

The D to A transition rates of the fourth voltage-sensor (DIV α and β) were modeled with the rates derived from fast inactivation time constants and steady-state fast inactivation values at given membrane potentials (Figure 2.4 *B* and *D*). The sum of the forward and reverse rates at a given voltage is defined by the time constant ($1/\alpha+\beta$) while the ratio of the forward to reverse rates is defined by the fraction of channels that inactivate at steady-state ($\alpha/\alpha+\beta$). From these relationships, the α and β rates can be calculated at each voltage. The calculated forward and reverse rates were fit by bi-exponential functions. Any changes to the DIV α and β rates will alter the simulated fast inactivation voltage-dependence and rates. The voltage-independent inactivation rate between the DIV-A and DIV-I states (FI) was the maximum rate of open-state fast inactivation in the experiments from the previous chapter (Figure 2.4*E*). Changes to this rate alter the simulated rates of fast inactivation onset, particularly at more depolarized potentials. The voltage-independent reverse rate (FR) was modelled to replicate the fraction of non-inactivating current from experimental recordings (Figure 2.5*B*). Changes to this rate alter the fraction of non-inactivating channels in ionic current simulations.

To produce modeled gating current traces, the proportion of each voltage-sensor which shifted between the D and A states in a time step was calculated. To accurately reproduce charge immobilization, the deactivation rate for DIII was multiplied by one minus the number of DIV voltage-sensors in the I state; the result was a slower deactivation rate of DIII when the channel is inactivated. When simulating gating charge movement, the value for proportion of DIII and DIV moved in each timestep were multiplied by 1.5 to account for the 50 % larger gating charge moved by these two.

The relaxation and de-relaxation rates of DIS4 and DIIS4 (DI/DII SI and SR) were directly derived from the fast time constants of slow inactivation (Figure 2.6E), whereas relaxation and de-relaxation rates of DIIS4 (DIII SI and SR) were derived from the slow time constant of slow inactivation (Figure 2.6F). The slow inactivation rates were calculated using a similar manner as that discussed above for DIV α and β . The slow inactivation onset time constant at a given voltage was used to calculate the total forward and reverse rates ($1/\text{SI}+\text{SR}$) at a given membrane potential. The fraction of the total rate accounted for by the forward rate was the maximal amplitude for the given time component of slow inactivation divided by the total slow inactivation amplitude. As the fast time component of slow inactivation is determined by two independent voltage-sensors in the model, the fraction of the fast outward rate was square-rooted prior to determining the SI and SR rates. The relaxation rates at -30 mV, 0 mV, and 30 mV were relatively similar, thus the average of the three was used as a voltage-independent forward rate (SI). The forward rate of slow inactivation (SI) was subtracted from the total slow inactivation rate to determine the reverse rate (SR). Changes to SI or SR in DI or DII alter the fast component of slow inactivation in the simulations, while changes to SI or SR in DIII alter the slow component of slow inactivation.

3.2.2. Experimental

For experiments on IFM/QQQ channels, all *Xenopus* oocyte preparation procedures, cut-open voltage clamp techniques, solutions, protocols, and analysis are as described in the previous chapter. The Nav1.5 IFM/QQQ mutant is in the pRcCMV plasmid. A QuikChange Lightning (Agilent Technologies) kit was used to perform site directed mutagenesis and make the IFM/QQQ E1784K construct.

Fluorescence experiments were performed by Wandu Zhu at Washington University in St. Louis. The DIII voltage-clamp fluorimetry (VCF) (C373Y/M1296C/Y1977A or C373Y/M1296C/E1784K/Y1977A) and DIV VCF (C373Y/S1618C/Y1977A or C373Y/S1618C/E1784K/Y1977A) constructs are in the pMAX plasmid. VCF constructs were linearized with PacI and then purified with the NucleoSpin Gel and PCR Clean-up kit (Macherey-Nagel, Bethlehem, PA). At

Washington University frogs were also housed in an AQUANEERING Xenopus Aquatic Housing System. Water temperature was maintained at 17-18 °C and frogs were fed with Nasco's frog brittle three times a week. At Washington University, both terminal and survival surgeries were performed in accordance with the Washington University Institutional Animal Care and Use Committee Protocol 20150237. In terminal surgeries euthanasia was confirmed by excision of the frog's heart. For fluorescence recordings cRNA for mutant human α -subunit Nav1.5 and human β 1-subunit (to boost expression for maximal fluorescent signals) were injected at a 1:2 molar ratio into oocytes.

For fluorescence recordings, Clampex software (v10; Molecular Devices, Sunnyvale, CA) was used for data acquisition. The light source for stimulation was a green, high-powered LED (PT-121, Luminus, Sunnyvale CA) controlled by a LED driver (Lumina Power, LDPC-30-6-24VDC). The light was then focused into a liquid light guide with a 45°, 5 mm compound parabolic concentrator (Edmund Optics, Barrington, NJ) and the guide was coupled to the microscope via a collimating adapter (EXFO, Quebec City, Canada). A 40 \times water-immersion objective with a numerical aperture of 0.8 (CFI Plan Fluor, Nikon, Tokyo, Japan) was used. Light measurements were made with a photodiode (PIN-040A; United Detector Technology, San Diego, CA) mounted on an XY axis manipulator (Thorlabs Inc., Newton NJ) at the microscope epifluorescence port. The photodiode was attached to the integrating headstage of a patch-clamp amplifier (Axopatch-200A; Molecular Devices) for low noise amplification of the photocurrent. The fluorescence emission was focused onto the photodiode active area using an achromatic doublet (Thorlabs Inc.) with a focal distance of 25 mm. Clampex software (v10; Molecular Devices) was used for data acquisition. Recording temperature was maintained at 19 °C with a temperature controller (HCC-100A; Dagan Corporation) (68,262). The internal recording solution was (mM): 105 NMDG-MES, 10 Na-MES, 20 HEPES, and 2 EGTA, pH 7.4. The external recording solution was (mM): 25 NMDG-MES, 90 Na-MES, 20 HEPES, and 2 Ca-MES₂, pH 7.4.

Before fluorescence recordings, oocytes were labeled with 20 μ M methanethiosulfonate-carboxytetramethylrhodamine (MTS-TAMRA; Santa Cruz

Biotechnology, Dallas, TX) in a depolarizing solution (mM: 110 KCl, 1.5 MgCl₂, 0.8 CaCl₂, 0.2 EDTA and 10 HEPES, pH 7.1) on ice for 20 min.

To record both fluorescence and conductance of the voltage-clamp fluorimetry mutants, cells were depolarized in 20 mV increments from a holding potential of -100 mV. Depolarizing pulses were preceded by a 100 ms long prepulse and 50 ms long postpulse at -120 mV. The amplitude of the fluorescence signals was determined as the mean of the signal from 5 ms after depolarizing voltage pulse to the end of voltage pulse. The magnitude of the signal in fluorescence traces is expressed as $\Delta F/F_0$ (%), where ΔF is the change in signal amplitude in response to the voltage change and F_0 is the baseline fluorescence recorded with no voltage change.

Fluorescence data were analyzed using Clampfit software (v10; Molecular Devices). To correct photobleaching of the fluorescence probe, fluorescence traces were subtracted by the fluorescence baseline, which was recorded with no change in voltage. The magnitude of fluorescence signals is expressed as $\Delta F/F_0$, where ΔF is the change in fluorescence in response to voltage change and F_0 is the magnitude of baseline.

3.2.3. Statistical Analysis

All statistical analysis was performed using JMP statistical software. Comparisons between IFM/QQQ and IFM/QQQ E1784K channels were made using a 2 factor repeated measures analysis of variance where the main factors analyzed were pH (ordinal variable) and mutant (nominal variable). The interaction between the two main factors was used to analyze differences in proton sensitivity. Statistical significance was measured at $\alpha < 0.05$. All midpoint measurements are means and measurements of error listed are standard error of the mean.

3.3. Results

The rates and equations used for the model can be found in Appendix B. Experimental means, standard error of the means, and number of independent experiments are found in Appendix C

3.3.1. The Peters-Ruben Model Accurately Recapitulates Experimental Gating and Ionic Currents

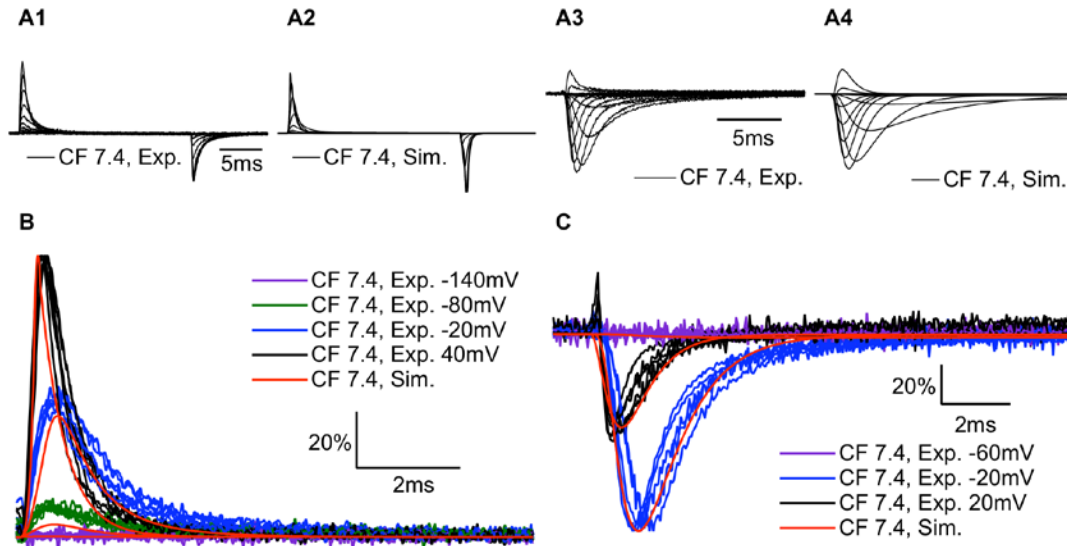


Figure 3.2. The Peters-Ruben Model Accurately Simulates Sodium Channel Ionic and Gating Currents

(A1-4) Sample experimental and simulated gating currents and ionic currents for C373F Nav_v1.5 at pH 7.4. (B) Overlaps of outward gating current traces recorded from 6 different cells expressing C373F Nav_v1.5 at pH 7.4 with simulated outward gating currents at the same membrane potentials. Gating currents were normalized to the peak outward current at 40 mV. (C) Overlaps of ionic current traces recorded from 6 different cells expressing C373F Nav_v1.5 at pH 7.4 with simulated ionic currents at the same membrane potentials. Ionic currents were normalized to the peak inward current at 20 mV. Overall the model replicates the experimental ionic and gating currents at different membrane potentials. Previously published in Peters et al., 2017 (3).

The model accurately simulates both ionic and gating currents. Simulated and experimental gating currents and macroscopic ionic currents are shown in Figure 3.2 A1-A4. Overlaps of experimental data with simulated gating currents and ionic currents at different voltages are shown in Figure 3.2 B and C. By integrating the modeled gating current, I obtained modeled QV curves (Figure 3.3A). Two issues with the modeled gating currents are an accelerated recovery of immobilized charge and a small depolarization of the QV relationship, both of which are discussed in the model limitations section of the discussion. The GV relationship, fast inactivation voltage-dependence, rates of fast inactivation onset and recovery, and rates of slow inactivation

onset and recovery overlap with experimental data from the previous chapter (Figure 3.3 B-F).

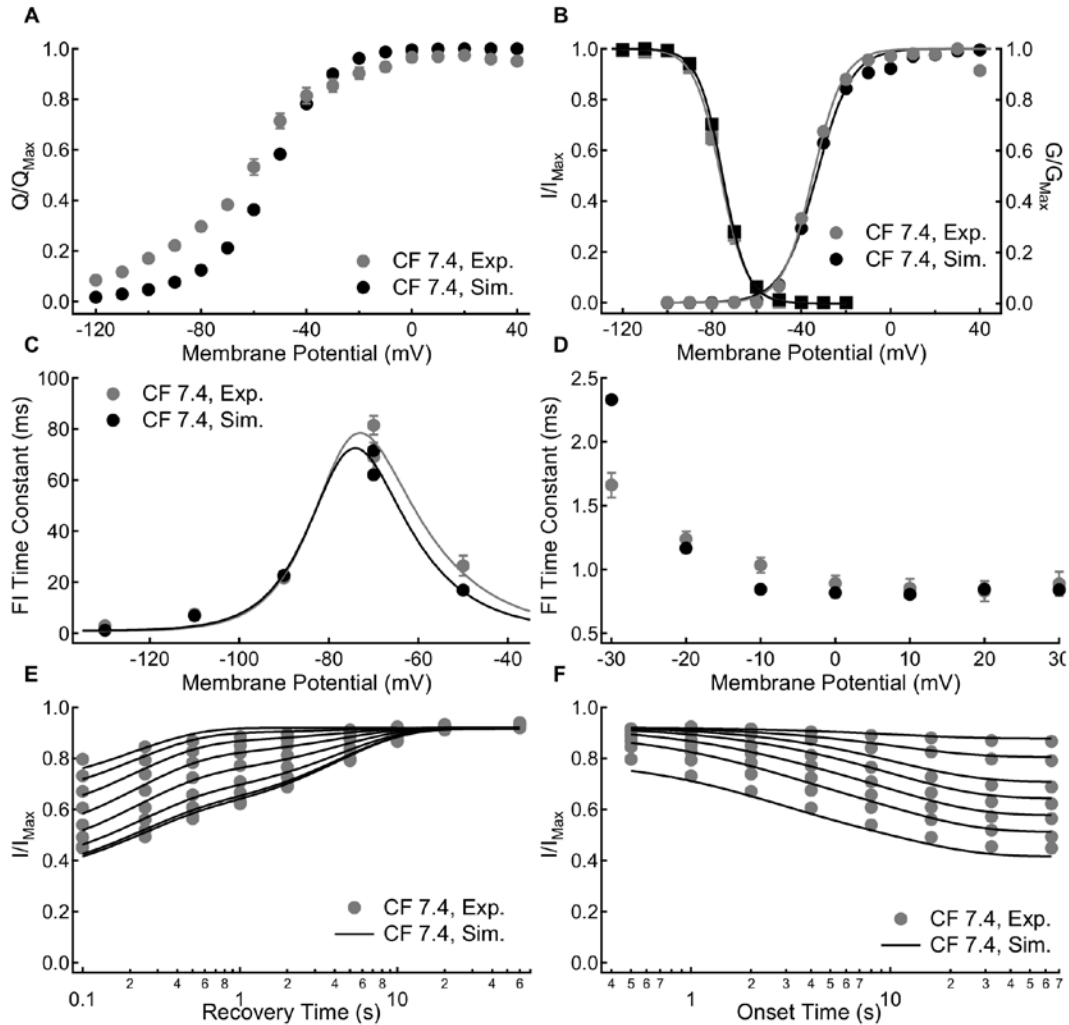


Figure 3.3. The Peters-Ruben Model Accurately Simulates Channel Activation, Fast Inactivation, and Slow Inactivation

The simulated charge voltage relationship of C373F Nav1.5 is overlapped with experimental data from the previous chapter in **A**. In **B** the simulated GV curve and voltage-dependence of fast inactivation is overlapped with experimental data from the previous chapter. In **C** and **D**, simulated time constants of C373F fast inactivation are overlapped with experimental data from the previous chapter. Simulated time courses of slow inactivation recovery and onset are overlapped with experimental data in **E** and **F**, respectively. Adapted from Peters et al., 2017 (3).

3.3.2. The E1784K Mutant Can be Modelled with Shifts to Fast Inactivation

Models of the sodium current at pH 6.0 were derived in the same manner as the pH 7.4 models from data collected at pH 6.0. Models of C373F/E1784K were the same as the C373F model at the same pH with the exception that the rates between D and A and A and I in domain IV were modified to reflect fast inactivation of E1784K. The E1784K model also includes a modified de-relaxation rate of DIII, but not domains I or II, to reflect the changes to the slow time component of slow inactivation. Simulated currents from all models are shown in Figure 3.4 *A1-A4*. The models accurately reproduced the direction of shifts seen in experimental data including: (1) the mutant-dependent hyperpolarization and proton-dependent depolarization in the QV relationship (Figure 3.4*B*); (2) the mutant- and proton-dependent depolarization of the GV curve (Figure 3.4*C*); (3) the mutant-dependent hyperpolarization and proton-dependent depolarization of steady-state fast inactivation (Figure 3.4*C*); (4) the mutant-dependent acceleration of fast inactivation recovery and onset and the proton-dependent slowing of fast inactivation onset (Figure 3.4*D*), and; (5) the mutant-dependent increase in non-inactivating current and the proton-dependent increase in normalized non-inactivating current in the E1784K mutant (Figure 3.4*E*).

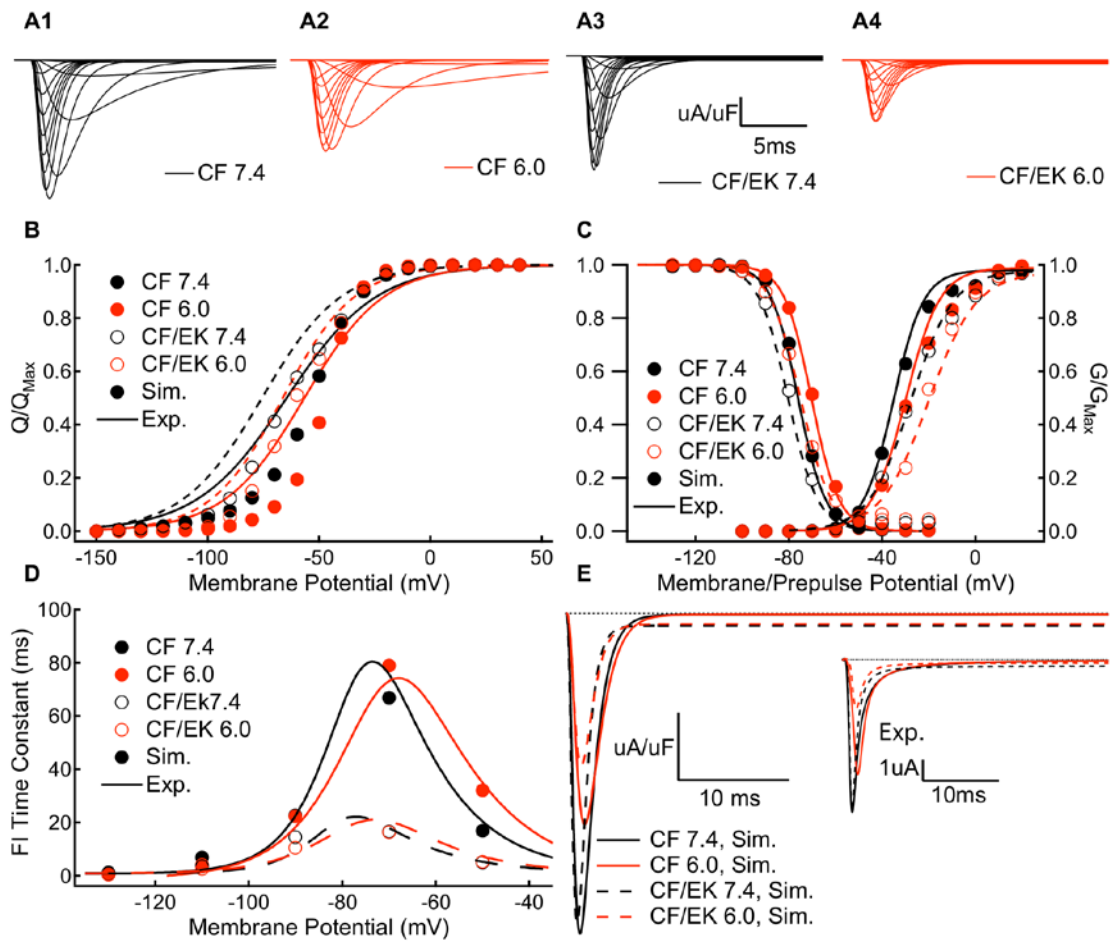


Figure 3.4. The Peters-Ruben Model Accurately Simulates E1784K Nav1.5 at pH 7.4 and pH 6.0

(A1-A4) Simulated ionic currents from C373F and C373F/E1784K Nav1.5 models at pH 7.4 and pH 6.0. (B) Simulated outward charge-voltage relationships from C373F (solid circles) and C373F/E1784K (open circles) Nav1.5 models at pH 7.4 (black) and pH 6.0 (red) are overlapped with fits to data from C373F (solid lines) and C373F/E1784K (dashed lines) experiments at pH 7.4 (black) and pH 6.0 (red). In all cases, there is a small depolarizing shift in the simulated gating current voltage-dependence which is reviewed in the discussion section (C) Simulated fast inactivation steady-state and conductance-voltage relationships from C373F (solid circles) and C373F/E1784K (open circles) Nav1.5 models at pH 7.4 (black) and pH 6.0 (red) overlapped with fits to data from C373F (solid lines) and C373F/E1784K (dashed lines) experiments at pH 7.4 (black) and pH 6.0 (red). (D) Simulated time constants of fast inactivation recovery (-130 mV to -70 mV) and closed-state fast inactivation onset (-70 mV and -50 mV) from C373F (solid circles) and C373F/E1784K (open circles) Nav1.5 models at pH 7.4 (black) and pH 6.0 (red) overlapped with fits to data from C373F (solid lines) and C373F/E1784K (dashed lines) experiments at pH 7.4 (black) and pH 6.0 (red). (E) Simulated persistent currents at -20 mV from C373F and C373F/E1784K Nav1.5 models at pH 7.4 and pH 6.0. (E inset) Sample experimental persistent current recordings at -20 mV from C373F and C373F/E1784K Nav1.5 at pH 7.4 and pH 6.0. Overall the model accurately replicates the experimental conductance-voltage relationship, steady-state fast inactivation, time course of fast inactivation, and persistent current amplitudes. Previously published in Peters et al., 2017 (3).

3.3.3. DIVS4 movement is shifted to more hyperpolarized potentials in E1784K

Recordings of activating and deactivating gating currents from the previous chapter, suggest that the E1784K mutant affects channel voltage-sensing domains. Based on: (1) the position of the mutant, (2) changes in fast inactivation, (3) increases in persistent current, and (4) a relatively smaller fraction of slowly deactivating gating charge, altered movement of the DIV voltage-sensor seems likely (20,72). My model of the E1784K channel suggests that the shifts in fast inactivation and the depolarization of the conductance-voltage relationship can be accurately simulated with shifts to the DIVS4 movement.

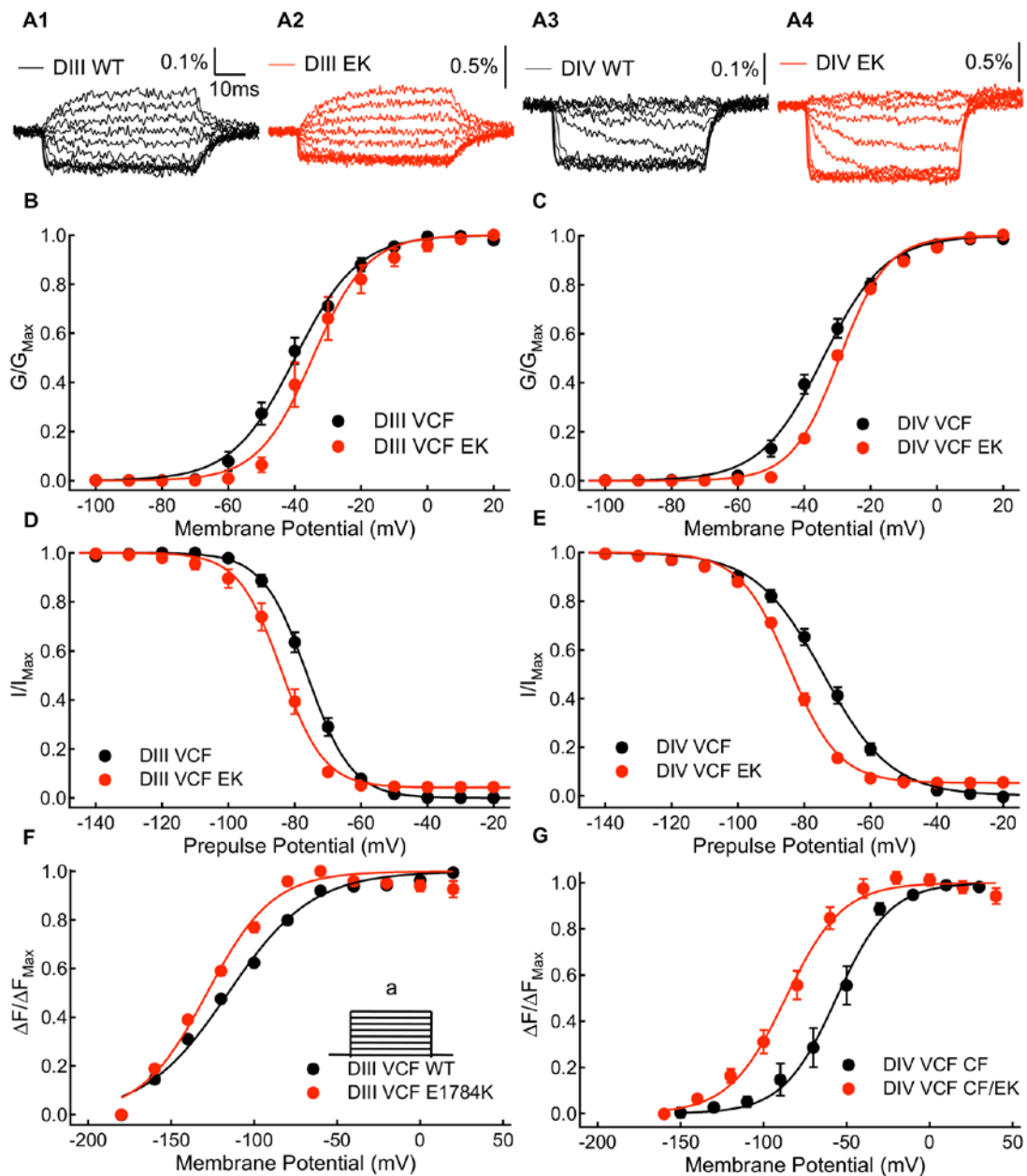


Figure 3.5. The Movement of DIVS4 is Hyperpolarized by the E1784K Mutant (A1-A4) Representative fluorescence signals for DIII-VCF, E1784K-DIII-VCF, DIV-VCF, and E1784K DIV-VCF constructs. Percentage of fluorescence change were calculated as $\Delta F/F_0$. Conductance-voltage relationships for DIII (B) and DIV (C) VCF constructs with and without the E1784K mutant. In both VCF constructs the E1784K mutant depolarizes the conductance-voltage relationship. Steady-state fast inactivation voltage-dependence for DIII (D) and DIV (E) VCF constructs with and without the E1784K mutant. In both VCF constructs the E1784K mutant causes a hyperpolarizing shift in the steady-state fast inactivation voltage-dependence. (F) Voltage-dependence of steady state fluorescence signal change (FV) of WT-DIII-VCF and E1784K-DIII-VCF constructs. The E1784K mutant causes a shift in the DIII FV curve to more hyperpolarized membrane potentials. (F inset) To measure the voltage-dependence of voltage-sensor fluorescence, the membrane potential of cells was changed to between -180 mV and +20 mV (a) from a holding potential of -120 mV. (G) Voltage-dependence of steady state fluorescence signal

change (FV) of WT-DIV-VCF and E1784K-DIV-VCF constructs. The E1784K mutant shifts the DIV FV curve in the hyperpolarizing direction. Adapted from Peters et al., 2017 (3).

To confirm whether DIV voltage-sensors is affected by E1784K, the voltage clamp fluorometry (VCF) method was used. The VCF constructs used a C373Y mutant instead of a C373F mutant to increase channel sensitivity to TTX. They also contain a Y1977A mutation to prevent ubiquitination of the channel to increase expression level. Sample traces of CY and CY/EK, DIII and DIV voltage-sensor fluorescence are shown in Figure 3.5 *AI-A4*. The E1784K mutant induces similar shifts in the midpoints of the channel conductance and fast inactivation curves in the two VCF constructs as in the non-VCF constructs (Figure 3.5 *B-E*). The voltage-dependence of voltage-sensor activation is described by the fluorescence-voltage (FV) curve. Compared to CY channels, CY/EK induces a significant shift in the hyperpolarizing direction in midpoint of the DIV FV ($P = 0.0126$) (Figure 3.5*F*), suggesting that the DIVS4 activates at lower potentials in the presence of the E1784K mutant. E1784K also causes a small shift in the hyperpolarizing direction in the midpoint of the DIII F-V curve ($P = 0.0193$) (Figure 3.5*G*). Since the DIII and DIV voltage-sensors have been shown to closely regulate each other, it is possible that any E1784K modulation of the DIIS4 is a secondary effect of modifications to the DIVS4 (263).

3.3.4. Removal of FI removes E1784K-Dependent shifts in conductance

As hypothesized, the model reproduced the depolarizing shift in C373F/E1784K conductance without any modifications in the activation rates of DI-DIII (Figure 3.6*B*). This mutant-dependent depolarizing shift in the GV curve was accompanied by a hyperpolarizing shift in the QV relationship in the E1784K model, consistent with the shift seen experimentally. To confirm that the changes to channel conductance in the E1784K mutant are due to altered fast inactivation, I measured conductance in the fast inactivation-deficient IFM/QQQ and the IFM/QQQ/E1784K mutants. Sample macroscopic ionic current traces at pH 7.4 and pH 6.0 are shown for IFM/QQQ and IFM/QQQ/E1784K channels in Figure 3.6 *AI-A4*. In the absence of fast inactivation, the GV relationship in the IFM/QQQ/E1784K mutant at pH 7.4 and pH 6.0 are not significantly different from those of IFM/QQQ (Figure 3.6*C*).

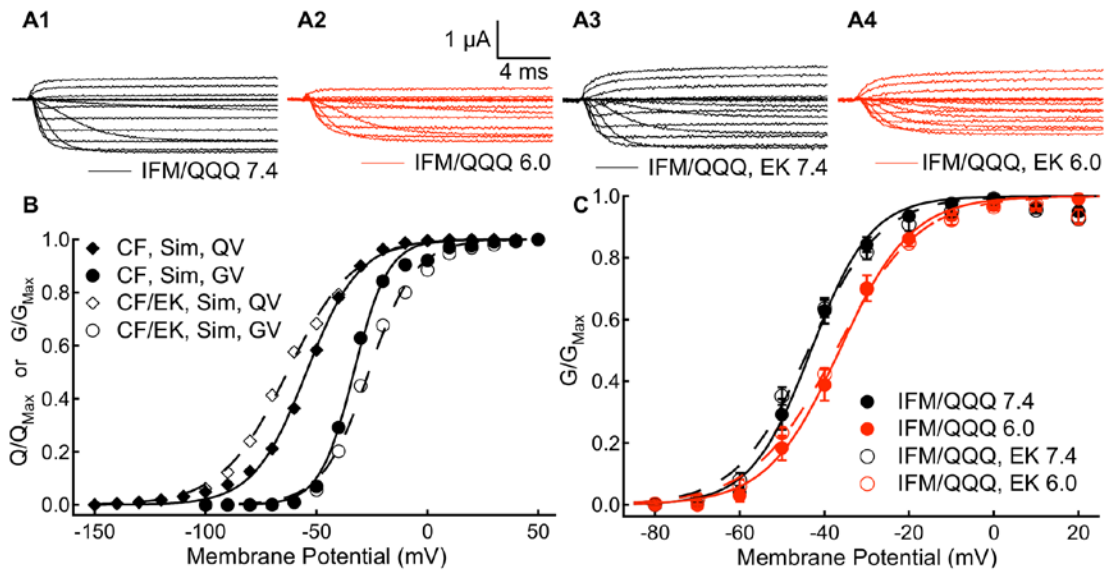


Figure 3.6. The E1784K Mutant Depolarizes the Conductance-Voltage Relationship Through Altered Fast Inactivation

(A1-A4) Sample ionic currents recorded from IFM/QQQ and IFM/QQQ-E1784K Nav_v1.5 at pH 7.4 and pH 6.0. (B) Simulated outward charge-voltage and conductance-voltage relationships from C373F and C373F/E1784K Nav_v1.5 models at pH 7.4. To replicate the hyperpolarizing shift in the midpoint of the charge-voltage relationship and the depolarizing shift in the midpoint of the conductance-voltage-relationship in the E1784K model required only changes to DIVS4 movement to correspond to experimental data on fast inactivation (C) Conductance-voltage relationships of IFM/QQQ and IFM/QQQ-E1784K Nav_v1.5 at pH 7.4 and pH 6.0. In the absence of fast inactivation, the E1784K mutant does not significantly affect the conductance-voltage relationship. Previously published in Peters et al., 2017 (3).

3.4. Discussion

Here I describe a new model of voltage-gated sodium current behavior that can simulate both ionic and gating currents. The model includes a voltage-independent step in the activation pathway of each voltage-sensor and a slow transition into a relaxed state at depolarized potentials. To simulate the effects of the E1784K mutant, I need only change the rates in DIV and one relaxation rate. Thus, this model predicts that the depolarization of the conductance curve in this mutant is caused by a mutant-induced change in fast inactivation, a finding confirmed by experiments with WT and E1784K mutant channels expressing IFM/QQQ, which removes fast inactivation.

3.4.1. The Peters-Ruben Model

This model proposes that a voltage-independent step is present in the activation pathway for voltage-gated sodium channels. Thus, I included a “stable” state which the majority of sodium channel S4 segments occupy at negative membrane potentials. A similar step has been used previously in models of hERG potassium currents (260). The rationale for a voltage-independent step in the hERG model and in this model is that the outward motion of the gating currents and the opening of the channel pore do not saturate to zero at depolarized membrane potentials (53,73,260). A voltage-independent, solvent-dependent step in channel opening has previously been suggested to represent the hydration of the channel pore following voltage-sensor activation (54). The voltage-independent step in this model, however, must be different because it is the rate-limiting step in gating charge movement at depolarized potentials. Thus, it must occur prior to the charge carrying steps in voltage-sensor activation.

Other models recognized that the activation step in sodium channels does not follow a straight voltage-dependent exponential equation, and used sigmoid curves (256,264). I chose to make this step explicit in the model and used the experimentally determined asymptote of outward gating current movement rates at positive membrane potentials as a forward rate (Figure 2.3B). Consistent with the altered asymptote in our gating current decay curves, I used a slower forward rate at pH 6.0. One problem is that I could not measure the reverse rate of this transition. To overcome this problem, I made an assumption that if greater than 10 % of channels were in the deactive state at rest, there would be a measurable component of gating current activation that is purely voltage-dependent. This would appear as a fast spike in gating current recordings that could be fit with a time constant that decays to zero at positive membrane potentials. This, however, was not seen in any of our gating current recordings in the previous chapter, thus I used a reverse rate that was 10x the forward rate. In the resulting simulations, greater than 90 % of the voltage-sensors occupy the stable state at hyperpolarized potentials; thus, the modeled gating currents show primarily voltage-independent activation at depolarized potentials, like the experimental results.

My recordings of ionic and gating currents do not allow for direct measurement of the D to A transition rates for any voltage-sensor; however, once the voltage-independent rates between the S and D states are known, the rates between the D and A states can be modeled such that the overall transition from S to A accurately replicates the experimental data. In contrast to other sodium channel gating models, the Peters-Ruben model uses different rates for the voltage-dependent step in the DIII activation pathway compared to that for DI and DII (8,256). When developing the model, I tried using 3 identical activation voltage-sensors with rates directly extracted from the gating current decay. Although this produced recognizable inward sodium currents, there were visible errors in the voltage-dependence of activation, particularly obvious at -20 mV and -10 mV (Figure 3.7A) when compared to experimental data (Figure 3.2A3). I subsequently used two fitting algorithms, a genetic algorithm and a climbing hill algorithm, that were allowed to alter the DIII or the DI and DII activation and deactivation rates while fitting to an average of 6 experimental IV curves (261). The outcome was a hyperpolarization of DIII activation movement and a slowing of its rates.

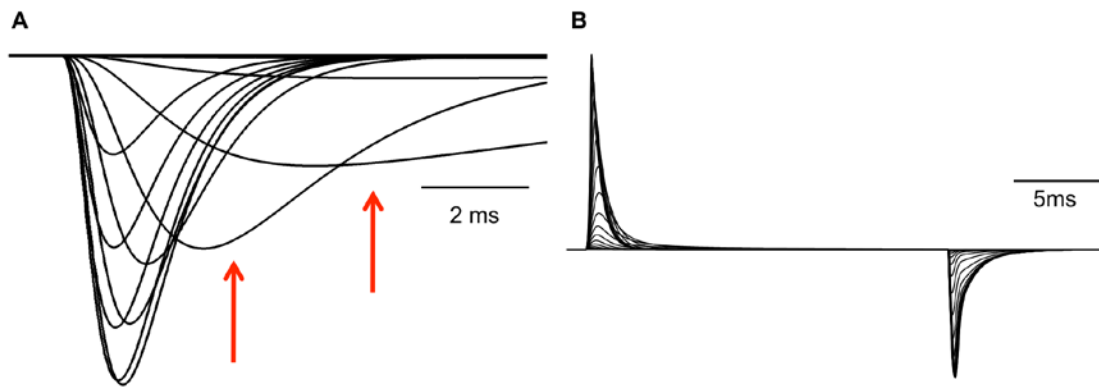


Figure 3.7. Limitations of the Peters-Ruben Model

Ionic currents simulated with the Peters-Ruben model with the rates of DIII activation being the same as DI and DII activation are shown in A. Red arrows show the -20 mV and -10 mV traces. B shows simulated gating currents when a hyperpolarization to -130 mV is used as opposed to -150 mV.

The model also includes a depolarization-induced transition to a relaxed state in the DI-DIII voltage-sensors, simulating slow inactivation. Fluorescence and gating current measurements show that the relaxed state is present in sodium and potassium channels, and, given its presence in *Ciona intestinalis* voltage-sensing phosphatase, is

likely an intrinsic voltage-sensor property (88,89,91,92,265). The impact and role of relaxation on ionic currents has not been fully resolved, however in sodium channels it may cause slow inactivation of the channel pore. A fluorescence study correlated the relaxation of the voltage-sensing domains to the onset and recovery of slow inactivation in Nav1.4 (88). Furthermore, the L689I mutant in Nav1.4, which alters ionic current slow inactivation, also causes corresponding changes to the relaxation rates of the voltage-sensors (89). For these reasons, the relaxation rates were used to model sodium channel slow inactivation.

Similar to the previous experimental study, a voltage-independent relaxation rate was used (89). The de-relaxation rate was voltage-dependent and may reflect that the voltage-sensor can move directly to the deactive state. Simulations in which the voltage-sensors relax directly to the deactive state did not differ from those in which the voltage-sensors went through the active state. I resolved two components of slow inactivation with time constants in the range of 1 s and 10 s. A third, slower component has also been observed with time constants in the 100 s range, but as the experimental data from the previous chapter were on a shorter timescale, this ultra-slow component was not included in the model (88,266). As exact coupling data for Nav1.5 voltage-sensors and slow inactivation are not available, I chose to couple the faster component (1 s) of slow inactivation to Domains I and II, and the slower component (10 s) to DIII. This choice was made because of the mutant changes to slow inactivation discussed below and may need to be revised if future fluorescence data on this coupling suggest otherwise.

Another possibility to code slow inactivation in the model is multiple relaxation steps for each voltage-sensor. Previous data suggest that all four voltage-sensors undergo relaxation movements on similar timescales, however the time scale that correlates to slow inactivation differs between the voltage-sensors (88,89). These data suggest that the faster components of relaxation in the DI and DII voltage-sensors are correlated to slow inactivation, while the slower component of relaxation in DIII is correlated to slow inactivation. This method was not implemented in this model as the relaxation transitions that do not correlate to a time component of slow inactivation can't be extracted from ionic data and require in depth fluorescence experiments; however, those wishing to

model the slower relaxed transitions in DI and DII or the faster relaxation transition in DIII could incorporate these transitions with a relatively small impact on computational efficiency

3.4.2. The E1784K Mutant Primarily Modifies Fast Inactivation

The Peters-Ruben model was used to test whether modifications of fast inactivation are sufficient to explain a hyperpolarization of the charge-voltage relationship in the presence of a depolarized conductance-voltage relationship. I hypothesized the hyperpolarized QV curve reflects a hyperpolarization of DIVS4 movement consistent with the hyperpolarization of steady-state fast inactivation in E1784K (20,146). The increased probability and rate of fast inactivation in the mutant could lead to decreased peak sodium currents in the middle of the normal GV curve when the rates of opening are slowest. This hypothesis is also consistent with data which show that a significant number of channels enter the fast-inactivated state before channel activation is complete (66).

When DIVS4 rates were altered to correspond to the increased probability and rate of fast inactivation in E1784K, the simulated GV curve depolarized to accurately reproduce the experimental GV. Furthermore, when channel fast inactivation was removed experimentally with IFM/QQQ, the E1784K mutant no longer depolarized the GV curve.

The only other change needed to model the E1784K mutant was an increase in the rate of de-relaxation in domain III (rate SR in DIII). Previous studies suggest that the rates of deactivation in DIII and DIV are slowed by channel fast inactivation, a process termed charge immobilization (72,267). The rate of fast inactivation recovery and persistent currents are increased in E1784K. The amplitude of the slow component of gating charge deactivation in E1784K is decreased which indicates a decrease in charge immobilization. Together these data indicate fast inactivation destabilization in E1784K. As the DIII-DIV linker normally stabilizes DIIS4 in an outward conformation, destabilization of fast inactivation may lead to decreased stability of the outward states (A and R) in DIIS4. For this reason, I chose DIIS4 to reflect the 10s component of slow

inactivation as E1784K increases the rate of slow inactivation recovery for that component.

Overall, these data show that the E1784K mutant alters sodium currents by altering fast inactivation. This may be important for targeting therapeutics to patients. As with some other Nav1.5 mutants, E1784K is associated with both a gain-of-function disorder (LQT3) and a loss-of-function disorder (Brugada syndrome) (134,268); pharmacological interventions for these mixed syndrome mutants may prove difficult (269). One of the first LQT3-specific treatments was the sodium channel blocker mexiletine; however, not all patients respond to mexiletine, and its effects in Brugada syndrome patients are mixed. Mexiletine rescues some trafficking deficient mutants, thereby increasing current density. In one patient with both Brugada syndrome and LQT3, however, mexiletine was found to increase persistent currents while also blocking the peak currents in the channel, leading to cardiac arrhythmia (269). These cases illustrate that, although the SCN5A gene is a common factor for Brugada syndrome and LQT3 patients, the pathophysiology and response to pharmaceuticals can vary based on the specific mutant. These data show that E1784K alters fast inactivation, thus pharmaceuticals targeted at DIV are a rational direction for drug development in E1784K patients.

3.4.3. Advantages of the Peters-Ruben Model

This model, and its strategy of modeling individual voltage-sensors, has some advantages over other models, including computational efficiency and a direct relationship to the channel structure and function. By individually modeling the voltage-sensors, the channel is constrained to 16 states while removing the assumption of equivalent activation voltage-sensors. Thus, this model is more efficient and comprehensive than previous models in that it requires fewer states while encompassing slow inactivation, which has been omitted in many previous models (53,259). Furthermore, by modeling the sensors separately, the cost of adding a state is relatively low as the number of explicitly modeled states increases by only one. This allows for the model to include two additional states of the voltage-sensors stable and relaxed, with

minimal decreases in efficiency. It also allows for model expansion. Currently, 3 distinct relaxed states per voltage-sensor, including DIV, have been suggested, which in this scheme would lead to a 25 state model (6+6+6+7) while the corresponding Markov chain would be 1512 states (6*6*6*7) (88,89). Expansion of the voltage-dependent activation process to include 5 distinct charge transferring steps would yield a 41 (10+10+10+11) state model with this formulation method and a Markov chain of 11,000 states (10*10*10*11) (19).

3.4.4. Limitations of the Peters-Ruben Model

This model has a few shortcomings, which include accelerated FI recovery at membrane potentials < -110 mV and a lack of explicit coupling between voltage-sensors. In this model, I chose to preferentially fit the fast inactivation curves to values within the physiological range. The outcome was that the recovery of fast inactivation at -130 mV is faster than observed experimentally. This error occurs outside the physiological range, but can lead to some resurgent currents, which are not observed experimentally, when the membrane potential is abruptly hyperpolarized to very negative potentials. This also leads to a faster recovery of immobilized gating charge at -150 mV. When off gating currents are simulated at -130 mV, however, the immobilized charge is similar to experimental recordings (Figure 3.7B).

This model also lacks much of the explicit coupling between voltage-sensors (263). Only one coupling interaction was included: DIIS4 deactivation was coupled to DIVS4 as part of the immobilized charge. Coupling exists between other voltage-sensors, but is not explicitly accounted for in our model or in other models of cardiac sodium channels. In this model, the coupling between sensors is assumed to be implicit in the experimental data from which our model is derived. Those wishing to use this model in studies of coupling may wish to include this explicitly as we did for DIII and DIV.

Because the original model formulation was based on data from gating charge movements, I was required to use a fitting algorithm to parameterize the DI-DIII activation steps to accurately model the conductance-voltage relationship. The resulting

modeled QV curve is slightly depolarized compared to the experimentally derived curve. This may be due to me not assigning the correct relative amounts of gating charge to each voltage-sensor. Based on estimates of total charge contribution from experiments using lidocaine to trap voltage-sensors, I assigned 30 % of the total charge moved to each of DIIS4 and DIVS4 and 20 % to each of DIS4 and DIIS4 (257). This assumption may be incorrect, however, as fluorescence experiments suggest DIIS4 and DIIS4 may be the voltage-sensors which carry the most charge (68). It is also possible that constraining DIS4 and DIIS4 to be equivalent causes part of the depolarizing shift. DIS4 movement is hyperpolarized compared to DIIS4, although not to the extent of DIIS4, and this would also shift the QV to more hyperpolarized potentials (68). Finally, the DIIS4 may need to be hyperpolarized further in the model (68). Simulations of conductance-voltage relationships are not sensitive to hyperpolarizing shifts in the DIII voltage-sensor rates. Thus, a hyperpolarizing shift in the DIII voltage-sensor rates could be used to hyperpolarize the simulated QV curve. Simulations from an updated model with a more hyperpolarized DIIS4 movement are found in chapter 5.4.

3.5. Conclusion

I present a new computationally-efficient model of the voltage-gated sodium channel directly related to channel structure. The model accurately replicates ionic and gating currents with many rates obtained directly from experimental data. The Peters-Ruben model predicts that the E1784K mutant primarily modifies the rates of fast inactivation, a finding confirmed with recordings in fast inactivation-deficient channels.

Understanding the mechanism by which E1784K alters channel gating may also act as a general indicator for how C-terminal sodium channel mutants lead to disease. The sodium channel C-terminus contains many other Brugada and LQT3 linked mutants including the 1795insD founder mutant (268). Understanding the pathophysiology of the C-terminal mutants may allow for more specific drug targeting capable of treating both the increases in persistent current and decreases in peak current which occur in these mutants. In the subsequent chapter I investigate which properties of residue 1784 are important for normal fast inactivation.

Chapter 4. Residue 1784 Mutants Disrupt Fast Inactivation Through Two Separate Mechanisms

4.1. Introduction

Voltage-gated sodium channels are heterotetrameric channels formed by 24 transmembrane segments split into 4 domains (DI-DIV) (37). Voltage-gated sodium channels open in response to membrane depolarization and pass an inward sodium current, which further depolarizes cells. This inward sodium current is transient as the channel undergoes a process termed fast inactivation during which the pore of the channel is occluded (5). The fast inactivation voltage-sensor is the fourth transmembrane segment in the fourth domain (DIVS4) and the inactivation particle is a conserved sequence of 4 amino acids (IFMT) in the DIII-DIV intracellular linker (20,62). Upon depolarization, DIVS4 moves outward and allows for binding of the IFMT to the underside of the channel, occluding the pore.

These two movements are subject to modification by other channel regions. One of the key regulators of channel fast inactivation is the C-terminus of the channel. Mutants in the C-terminus of sodium channels alter the voltage-dependence, rate, and stability of the fast-inactivated state (146,268). In the cardiac sodium channel, Nav1.5, many disease-causing mutations occur within the C-terminus, including the most prevalent Brugada syndrome and Long QT syndrome (LQT3) mutant, E1784K (134). The E1784K mutant alters almost all aspects of channel gating. E1784K depolarizes the voltage-dependence of conductance, hyperpolarizes the voltage-dependence of fast inactivation, accelerates fast inactivation onset and recovery, and increases the fraction of non-inactivating current (2,133,134,146,178,243). In the previous chapter I showed that the E1784K-dependent depolarization of the conductance-voltage relationship is not due to depolarization of the voltage-sensors responsible for channel activation. Rather the DIVS4 voltage-sensor moves at more hyperpolarized membrane potentials in E1784K. The corresponding hyperpolarization and accelerated onset of fast inactivation are

sufficient to cause the depolarization of the conductance voltage-relationship. What is not known, however, is whether E1784K acts directly on DIVS4, the DIII-DIV linker, or both.

Many structural and functional studies have suggested an interaction between the C-terminus of the sodium channel and the DIII-DIV linker (9,46,77,83,84). This interaction may be calcium and calmodulin-dependent; however, studies show that mutants in the C-terminus are capable of modifying inactivation in the absence of calmodulin or changes to intracellular calcium concentration (2,77,79,133). To these data was recently added the first crystal structures of a heterotetrameric eukaryotic voltage-gated sodium channel. The cryo-EM structure of the cockroach NavPaS shows extensive interactions between the proximal C-terminus and not only the DIII-DIV linker, but also the intracellular linkers of DIV (9). Interestingly, many of the negatively-charged residues in the C-terminus are conserved between human voltage-gated sodium channels and NavPaS despite only 36-43 % overall homology. E1784 is conserved between Nav1.5 and NavPaS (E1423) and is located within the proximal C-terminus. Given that E1784K alters almost all aspects of fast inactivation, it potentially may disrupt interactions with both the DIII-DIV linker and the intracellular linkers of DIV.

One way to test the existence of two interactions is to see if different mutants at position E1784 can separately alter fast inactivation voltage-dependence and completeness. I measured ionic and gating currents from 8 different constructs: E1784, E1784D, E1784A, E1784Q, E1784V, E1784W, E1784R, and E1784K at pH 7.4, pH 7.0, and pH 6.0. These experiments show that large disruptions of fast inactivation rates and voltage-dependence can occur without increasing the fraction of non-inactivating current. I also show the effect of protons on peak and persistent currents differ between mutants in a manner consistent with our theories in the previous chapters. From these data, I propose that the E1784K mutant disrupts two separate interactions of the C-terminus. I hypothesize that disrupting the interaction between the C-terminus and the DIII-DIV linker decreases the stability of the fast-inactivated state causing non-inactivating current. Meanwhile, disrupting the interactions between the C-terminus and the intracellular linkers of DIV modifies the rate and voltage-dependence of fast inactivation.

4.2. Methods

4.2.1. DNA Constructs

The C373F and the C373F/E1784K constructs in pPol1 were used in a previous study from our lab. The E1784A point mutant was made by Ziwei Ding (Simon Fraser University). The other mutants at position 1784 were introduced into the C373F pPol1 construct using a QuikChange Lightning kit.

All DNA constructs were cloned in 10 β *E. coli* cells, purified using a Qiagen Midi-prep kit and sequenced by either Eurofin MWG Operon sequencing service or Genewiz sequencing service. I used NotI to linearize all constructs. Transcription was performed using a T7 mMESSAGING mMACHINE high yield capped RNA transcription kit.

4.2.2. Oocyte Preparation

The *Xenopus laevis* oocyte preparation has been published previously (235). All animal surgery and animal care procedures were performed in accordance with the policies of the Simon Fraser Animal Care Committee and the Canadian Council of Animal Care.

4.2.3. Data Acquisition and Protocols

All equipment, solutions, data acquisition procedures, and protocols are the same as those previously published (3).

4.2.4. Data Analysis

All statistical analysis was performed using JMP statistical software. Comparisons of means were made using a 2 factor repeated measures analysis of variance where the main factors analyzed were mutant (nominal variable) and pH (repeated, scalar variable). A significant interaction between mutant and pH was interpreted as a difference in the proton effect on the dependent variable on at least one

mutant relative to the others. Pairwise comparisons between mutants were not tested and P-values reported are those of the main factors or interaction factor from the full ANOVA test. For comparisons of time constants, the log of the time constants was compared. Statistical significance was measured at $\alpha < 0.05$. All midpoint measurements are means and measurements of error listed are standard error of the mean. For measurements of correlation, the Pearson correlation coefficient is given. The test for a significant correlation was against the null hypothesis that the Pearson correlation coefficient is 0.

4.2.5. Homology Models

Molecular graphics and analyses were performed with the UCSF Chimera package. Chimera is developed by the Resource for Biocomputing, Visualization, and Informatics (RBVI) at the University of California, San Francisco (supported by NIGMS P41-GM103311) (44). The Homology model of the Nav1.5 sequence on the NavPaS structure was constructed using MODELLER software run at RBVI.

4.3. Results

The source data for figures in this chapter, including means, standard error of the mean, and number of independent recordings are found in Appendix D.

4.3.1. Conductance

I measured conductance from macroscopic inward sodium currents at membrane potentials between -100 mV and +40 mV. Sample current traces for each mutant are shown in Figure 4.1 *A1-A8*. There is a significant mutant dependent effect on the midpoint of the conductance voltage (GV) relationship ($P=0.0007$) (Figure 4.1*B*). The E1784W GV curve is the most hyperpolarized, while E1784V is the most depolarized. There is also a significant pH dependent effect on the midpoint of the GV curve ($P<0.0001$) (Figure 4.1*C*). Lowering extracellular pH depolarizes the midpoint of the GV curve in all cases. Decreasing extracellular pH also significantly reduces the maximal conductance in all mutants ($P<0.0001$) (Figure 4.1*D*). The proton-dependent block of

maximal conductance is significantly different between channel variants, ranging from 24 % to 48 % at pH 6.0 ($P=0.0016$).

4.3.2. Fast Inactivation

I measured the voltage-dependence of fast inactivation using 500 ms prepulses to membrane potentials between -150 mV and -10 mV followed by a test pulse to -10 mV. There is a significant mutant-dependent shift in the midpoint of the fast inactivation voltage-dependence ($P<0.0001$) (Figure 4.2A). The most hyperpolarized midpoint of fast inactivation voltage-dependence is in the E1784K mutant while the most depolarized midpoint occurs in the E1784W mutant. Decreasing extracellular pH causes a significant depolarization of the midpoint of the fast inactivation voltage-dependence in all mutants ($P<0.0001$).

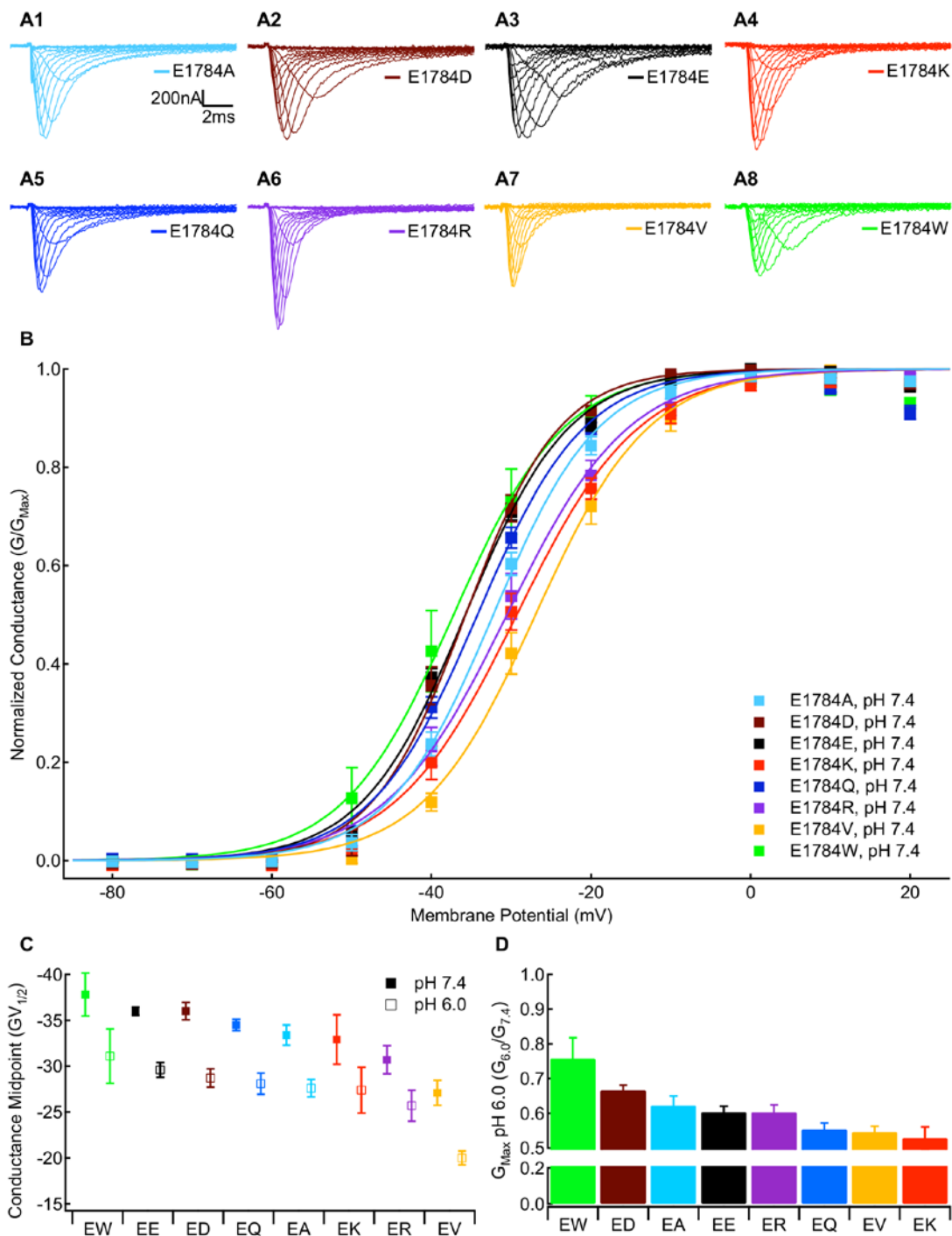


Figure 4.1. Mutants at Residue 1784 in Nav1.5 Alter the Voltage-dependence of Conductance and Proton Block of Maximal Conductance

A1-A8: Sample macroscopic sodium currents recorded in residue 1784 mutants at extracellular pH 7.4. **B:** Normalized conductance-voltage relationships of residue 1784 mutants at extracellular pH 7.4. **C:** Average midpoints of the conductance-voltage relationships for residue 1784 mutants at extracellular pH 7.4 and pH 6.0. **D:** Fraction of conductance remaining at extracellular pH 6.0 in residue 1784 mutants.

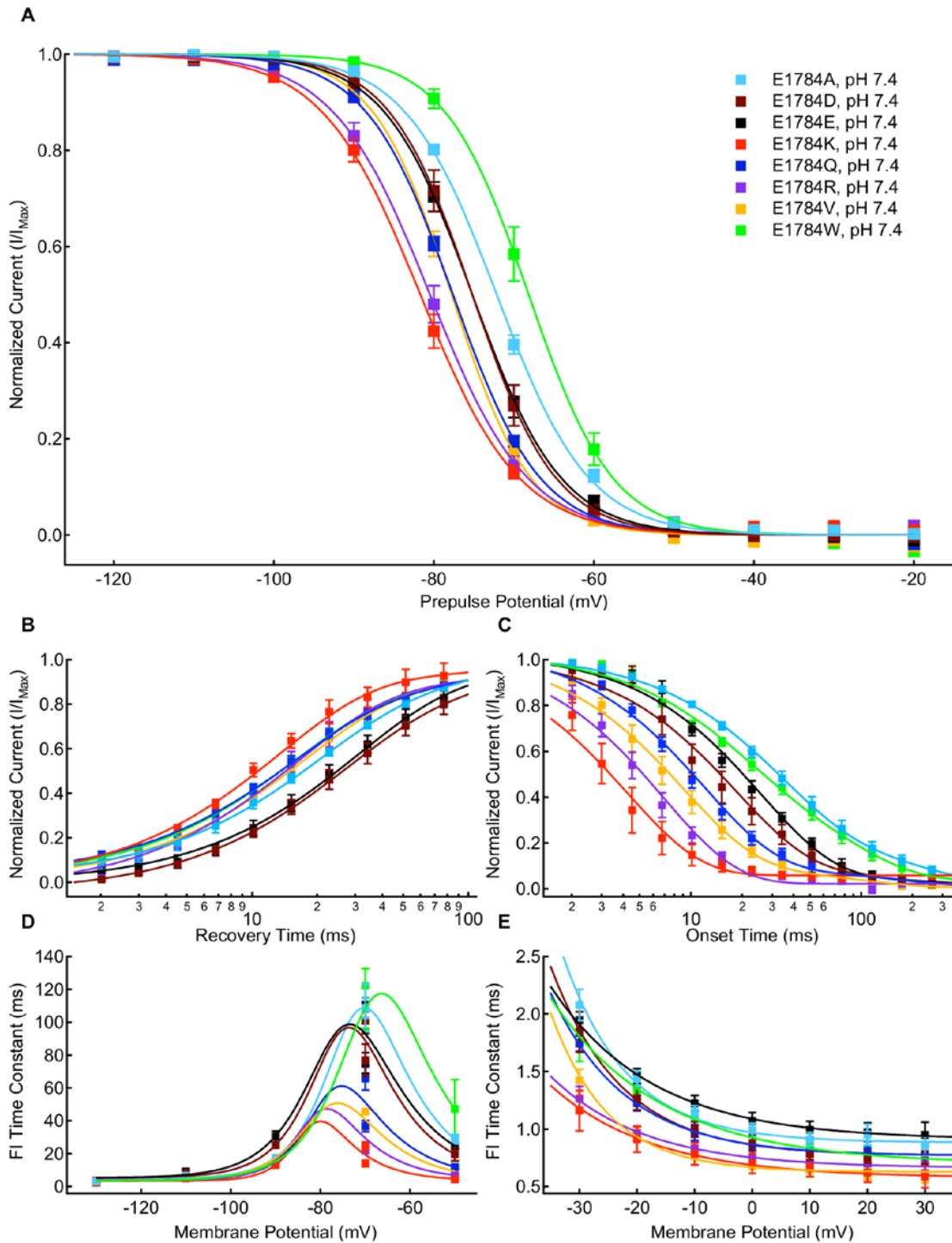


Figure 4.2. Mutants at Residue 1784 in Na_v1.5 Alter the Rates and Voltage-Dependence of Fast Inactivation

A: Average voltage-dependence of fast inactivation in residue 1784 mutants at extracellular pH 7.4. **B:** Average time course of fast inactivation recovery at -90 mV in residue 1784 mutants at extracellular pH

7.4. **C:** Average time course of fast inactivation onset at -50 mV in residue 1784 mutants at extracellular pH 7.4. **D:** Average time constants of fast inactivation recovery and closed-state onset plotted versus voltage for residue 1784 mutants at extracellular pH 7.4. **D:** Average time constants of open-state fast inactivation onset plotted versus voltage for residue 1784 mutants at extracellular pH 7.4.

The rates of fast inactivation recovery and closed-state fast inactivation onset were measured using double pulse protocols. Time courses of fast inactivation recovery at -90 mV are shown for all mutants in Figure 4.2B. Time courses of closed state fast inactivation onset are shown for all mutants at -50 mV in Figure 4.2C. The fast time constant of recovery or onset was determined from double exponential fits to recovery or onset time courses, the exception being the -70 mV recovery where only a single exponent could be fit. The fast time constants are plotted versus voltage in Fig 4.2D. There was a significant mutant effect on the fast time constant of fast inactivation recovery and onset at all membrane potentials ($P < 0.0001$ at all membrane potentials). There is also a significant proton-dependent acceleration of fast inactivation recovery or slowing of fast inactivation onset at all membrane potentials ($P < 0.0001$ at all membrane potentials). There is a significant interaction between extracellular pH and the mutant at -70 mV for both onset and recovery of fast inactivation ($P \leq 0.0306$). This likely reflects that at -70 mV a different fraction of channels will onset or recover from inactivation in each mutant. As decreasing extracellular pH slows inactivation onset and speeds recovery, the effect of decreasing pH on a given mutant will depend on the fraction of channels which recover from inactivation versus onset into the inactive state.

I measured the rate of open-state fast inactivation by fitting macroscopic current decay at membrane potentials between -30 mV and +30 mV with a single exponential equation. The time constants of open-state fast inactivation are plotted versus voltage for all mutants in Figure 4.2E. There is a significant mutant-dependent effect ($P \leq 0.0046$) and pH-dependent effect ($P \leq 0.0003$) on the time constant of open-state fast inactivation at all membrane potentials. The 3 fastest inactivating mutants were E1784K, E1784R, and E1784V, while E1784E and E1784A typically showed the slowest inactivation. As with the data in chapter 2, lowering extracellular pH slows open-state fast inactivation.

4.3.3. Gating Charge Activation and Deactivation

I measured the voltage-dependence of gating charge activation (QV) by integrating the outward gating current during 20 ms depolarizations from a holding potential of -150 mV to membrane potentials between -150 mV and +40 mV. This was followed by a 20 ms repolarization to -150 mV. Sample outward currents are shown in Figure 4.3A. I measured the voltage-dependence of gating current deactivation using 20 ms repolarizations between 20 mV and -150 mV after a 20 ms depolarization to +50 mV. The amount of returning charge was assessed by integrating the outward gating currents during subsequent depolarizing pulses to +50 mV. Sample deactivating gating currents are shown in Figure 4.3B. There are significant mutant-dependent shifts in the midpoint of the activation QV relationship (Figure 4.3C) and deactivation-voltage relationship (Figure 4.3D) ($P < 0.0001$). Notably the ordering of mutants differs between gating current activation and deactivation (Figure 4.3E). The E1784K mutant activates at the most hyperpolarized potentials, but has the third most depolarized voltage-dependence of deactivation. In contrast, the E1784A mutant has the second most depolarized voltage-dependence of gating current activation and the most hyperpolarized gating charge deactivation. Thus, while the E1784K mutant has approximately 7 mV of hysteresis between gating charge activation and deactivation, the E1784A mutant has approximately 30 mV of hysteresis. Decreasing extracellular pH significantly depolarizes the voltage-dependence of gating charge activation and deactivation ($P < 0.0001$). The effects of decreasing extracellular pH did not significantly differ between mutants for either gating charge activation or deactivation ($P \geq 0.330$).

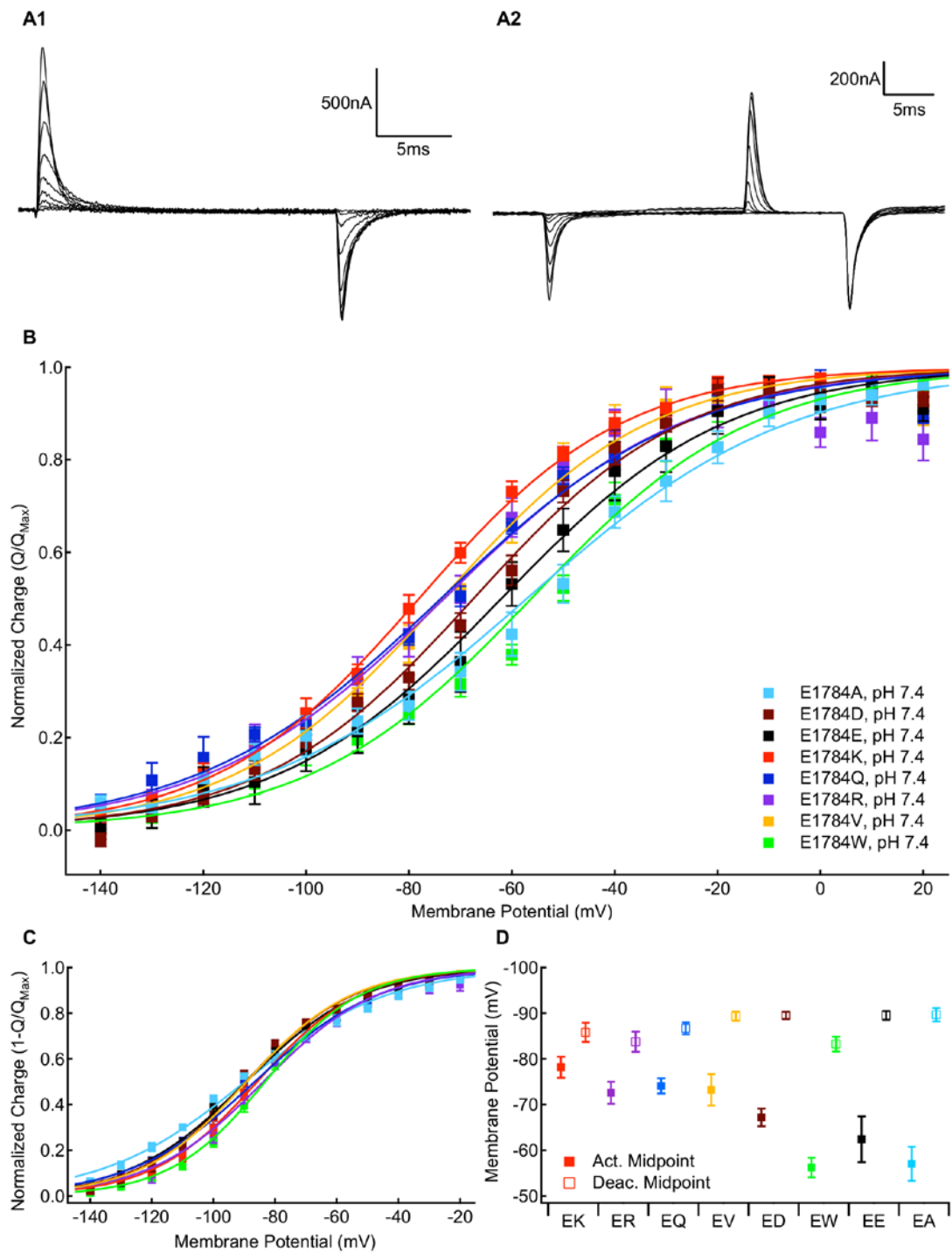


Figure 4.3. Mutants at Residue 1784 Alter Gating Current Voltage-Dependence
A1: Sample gating currents recorded with the activation protocol described in the text. **A2:** Sample gating currents recorded with the deactivation protocol described in the text. **B:** Average voltage-dependence of gating charge activation for residue 1784 mutants recorded at extracellular pH 7.4. **C:** Average voltage-dependence of gating charge deactivation for residue 1784 mutants recorded at extracellular pH 7.4. **D:** Average midpoints of gating charge activation and deactivation for residue 1784 mutants at extracellular pH 7.4.

4.3.4. Non-inactivating Current

I measured non-inactivating sodium current at the end of 100 ms depolarizations to membrane potentials between -30 mV and 0 mV. 5 traces were averaged for each recording. Sample non-inactivating currents from cells with similar peak current amplitudes are compared for all mutants in Figure 4.4A. There is a significant mutant-dependent effect on the normalized persistent current at all measured membrane potentials ($P < 0.0001$ in all cases) (Figure 4.4B). At all membrane potentials, the E1784K mutant has the largest fraction of non-inactivating current. The fraction of non-inactivating sodium current is similar in all other mutants except E1784R. The E1784Q mutant had no discernable non-inactivating sodium current in many recordings. There is a significant interaction between decreasing extracellular pH and mutant at all membrane potentials ($P \leq 0.0160$). The fraction of non-inactivating current is increased most in E1784K and E1784R channels by decreasing extracellular pH (Figure 4.4C). This is not the case for the other mutants.

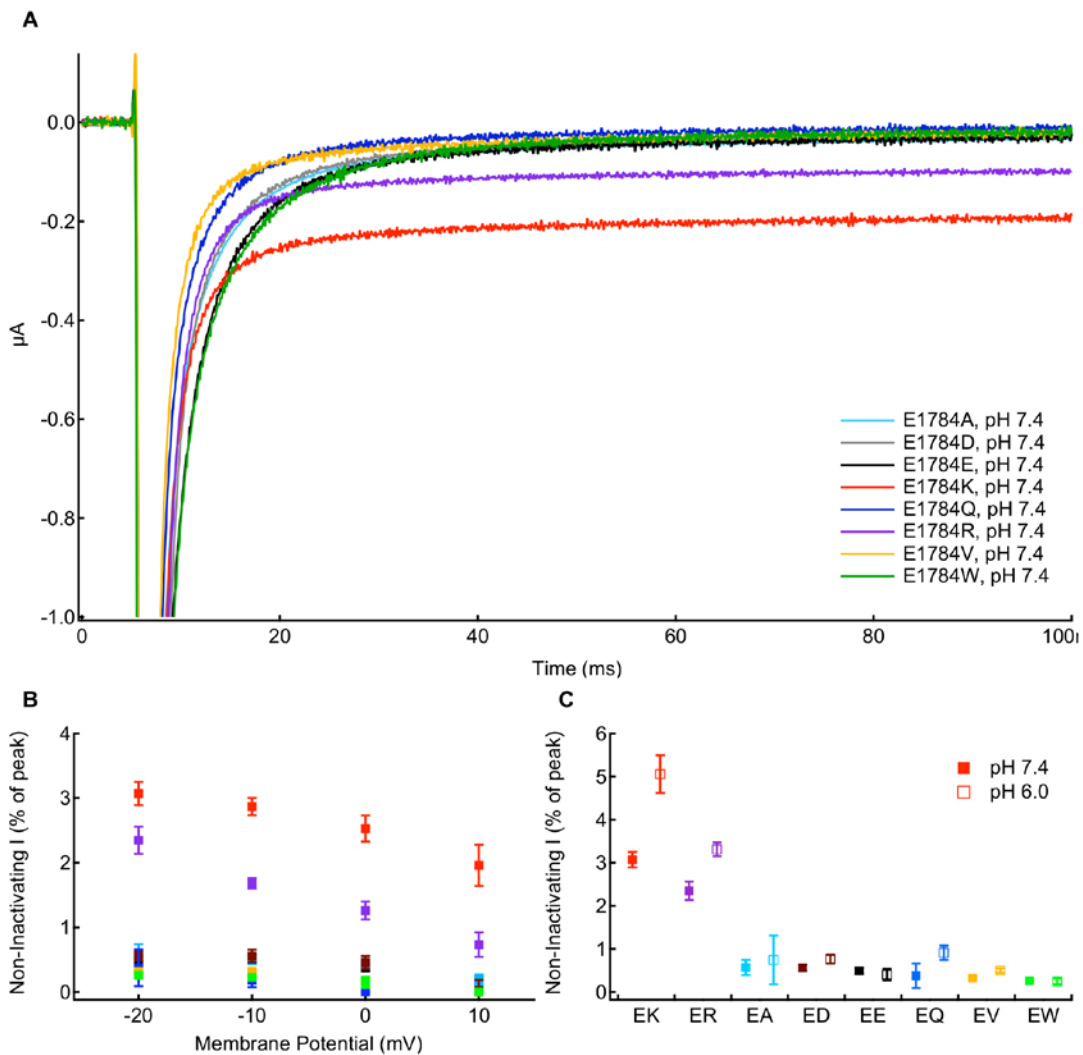


Figure 4.4. Positively Charged Mutants at Residue 1784 Increase Non-Inactivating Current

A: Sample currents recorded at -10 mV from residue 1784 mutants with similar size peak currents at extracellular pH 7.4. **B:** Average non-inactivating current as a percent of peak current for residue 1784 mutants recorded between -30 mV and 0 mV at extracellular pH 7.4. **C:** Average non-inactivating current at -30 mV as a percent of peak current for residue 1784 mutants at extracellular pH 7.4 and pH 6.0

4.3.5. Correlations

In the previous chapter, I showed that the hyperpolarization of the gating charge activation voltage-dependence in E1784K is due to the hyperpolarized movement of the DIVS4 voltage-sensor. As the DIVS4 acts as the voltage-sensor for fast inactivation, so long as the shifts in the DI-DIII voltage-sensors are minimal, the midpoint of our activation QV curve should correlate to the midpoint of fast inactivation voltage-

dependence. From most hyperpolarized to most depolarized the midpoints of fast inactivation voltage-dependence and gating charge activation at pH 7.4 were: $K < R < Q < V < D < E < A < W$ for fast inactivation and $K < Q < V < R < D < E < A < W$ for gating charge activation (Figure 4.5B). There was a significant correlation between the midpoint of the fast inactivation voltage-dependence curve and the QV curve at pH 7.4 ($R = 0.92$, $P = 0.0011$). Notably, the midpoint of the conductance voltage-relationship and QV curve did not correlate ($P = 0.1438$) (Figure 4.5A).

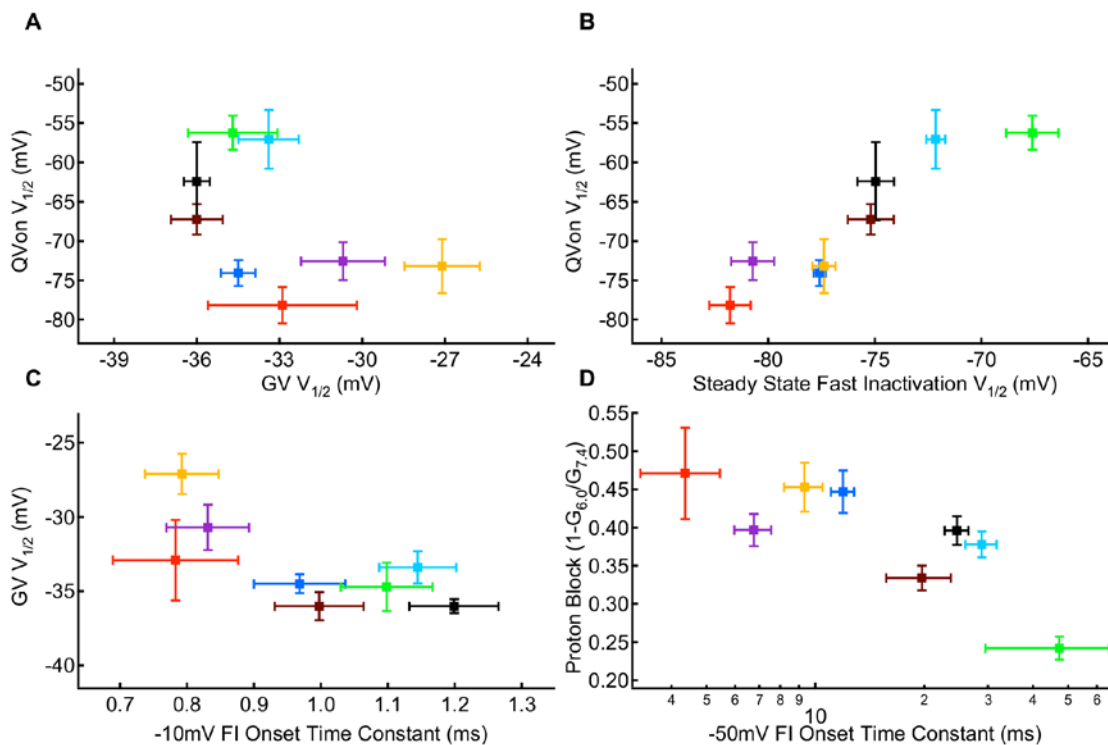


Figure 4.5. The Voltage-Dependence of Gating Charge Movement Correlates to the Voltage-Dependence of Fast Inactivation but not Conductance

A: Midpoint of the conductance-voltage relationship for residue 1784 mutants plotted versus the midpoint of the charge-voltage relationship. **B:** Midpoint of the voltage-dependence of fast inactivation for residue 1784 mutants plotted versus the midpoint of the charge-voltage relationship. **C:** Midpoint of the conductance-voltage relationship for residue 1784 mutants plotted versus the time constant of open state fast inactivation at -10 mV. **D:** Fraction of maximal conductance blocked by decreasing extracellular pH to pH 6.0 for residue 1784 mutants plotted versus the time constant of closed-state inactivation onset at -50 mV.

In the previous chapters, I showed that the depolarized midpoint of the conductance-voltage relationship in E1784K is due to the altered fast inactivation. Thus, the midpoint of the conductance voltage-relationship should correlate to fast inactivation

parameters. At pH 7.4 there is a significant correlation between the midpoint of the conductance curve and the time constants of open state fast inactivation at -20 mV, -10 mV, 0 mV, and 10 mV (Figure 4.5C) ($R \geq 0.71$, $P \leq 0.0468$). Similarly, the proton block of maximal conductance at pH 6.0 is correlated with the rate of closed state fast inactivation at -70 mV and -50 mV ($R = 0.79$, $P = 0.0201$, at -70 mV; $R = 0.73$, $P = 0.0398$, at -50 mV) (Figure 4.5D).

4.4. Discussion

The data presented show how different mutants at position 1784 in the cardiac sodium channel, Nav1.5, alter ionic and gating currents. The E1784K mutant is the most prevalent Brugada syndrome and LQT3 mutant in Nav1.5 and alters almost all aspects of channel gating (134,146). In the previous chapters, I showed that the E1784K mutant hyperpolarizes the movement of DIVS4 and that this hyperpolarized movement is responsible for hyperpolarization of the voltage-dependence of the outward gating currents. I also showed that the hyperpolarization and acceleration of fast inactivation in the E1784K mutant is responsible for depolarization of the conductance-voltage relationship. The data presented here support these findings while also suggesting that the E1784K mutant acts through two mechanisms. I hypothesize these two mechanisms are (1) a disrupted interaction between the C-terminus and the DIII-DIV linker, and (2) a disrupted interaction between the C-terminus and the DIVS4-S5 linker.

4.4.1. E1784 Mutants Destabilize Two Fast Inactivation Interactions

The proximal C-terminus is a key regulator of sodium channel function and expression. Approximately one third of the initial 30 amino acids of the C-terminus are negatively charged glutamates or aspartates. Mutants of these negative charges disrupt the voltage-dependence, rate, and completeness of fast inactivation (134,145,146,268,270). Data in the preceding chapters show that the E1784K mutant alters the movement of DIVS4 and increases the fraction of non-inactivating currents. What is not known is whether these two effects occur due to a single disruption or whether the mutant disrupts multiple interactions. I sought to assess this possibility by

testing multiple mutants at position 1784 and measuring whether a given mutant can alter only one property.

Our data suggest that the E1784K mutant destabilizes two separate interactions, one of which is responsible for changes to the voltage-dependence and rate of fast inactivation, and one of which is responsible for the increase in non-inactivating current. As with the experiments in the preceding chapters, these data show that the E1784K mutant hyperpolarizes and accelerates fast inactivation compared to E1784 Nav1.5. The E1784R mutant exerts a similar effect to the E1784K mutant, while E1784V and E1784Q both have a lower magnitude of effect. In contrast, the E1784W mutant depolarizes the voltage-dependence of fast inactivation compared to E1784 Nav1.5. The E1784K mutant also causes a large fraction of non-inactivating sodium current. The E1784R mutant increases the fraction of non-inactivating current, but to a lesser extent compared to E1784K. Notably, despite inducing shifts in the voltage-dependence and rates of fast inactivation, none of the E1784V, E1784Q, or E1784W change the fraction of non-inactivating sodium current. E1784V, in particular, exerts a similar magnitude of effect as E1784R in many protocols, yet does not increase the fraction of non-inactivating current.

Overall, these data suggest that non-inactivating current is conferred by the presence of a positive charge at position 1784. Neutralization of E1784 does not induce a non-inactivating current, although previous work suggests neutralizing 4 successive glutamate residues in this region (E1773Q/E1780Q/E1781Q/E1784Q) is sufficient (133). Interestingly, the E1784R mutant confers a significantly smaller fraction of non-inactivating current compared to E1784K. This may be due to the positive charge on arginine being split between three nitrogens, while on lysine the positive charge is localized on a single nitrogen. A similar effect can be seen in the sodium channel selectivity filter where K1419R mutant abolishes selectivity for sodium over potassium (56). This suggests that E1784 may be close in proximity to a positive charge that would be more strongly repelled by lysine than arginine.

In contrast to increases in non-inactivating current, disruptions of the rate and voltage-dependence of fast inactivation can seemingly be conferred by any large disruption at position 1784. The recently-solved structure of the NavPaS eukaryotic sodium channel shows C-terminal interactions with the DIVS4-S5 linker just downstream of the position homologous to residue 1784 (9). Mutants at position 1784 might, therefore, disrupt the structure of this region and alter this interaction. The data presented show that E1784R, E1784K, E1784V, E1784Q, and E1784W alter the voltage-dependence and/or rates of fast inactivation. Substitution of residue 1784 with any of lysine, arginine, valine, or glutamine accelerates fast inactivation. Conversely, the E1784W mutant decelerates fast inactivation and depolarizes the voltage-dependence of fast inactivation. A possible model is that a C-terminal interaction with the DIVS4-S5 linker normally stabilizes the deactive conformation of DIVS4 and restricts the movement of DIVS4. The E1784K mutant disrupts overall conformation of the C-terminus, in doing so it disrupts the interaction with the DIVS4-S5 linker. This removes the restrictions on DIVS4 movement and allows for accelerated movement. An interesting aspect of the data presented is that E1784W stabilizes the deactive conformation of DIVS4. Tryptophan is rich in pi-electrons, allowing it to form stable interactions with cations, C-H groups, aromatic residues, and adjacent prolines (271–274). Residue 1784 is adjacent to P1785 and, as discussed below, I predict residue 1784 normally interacts with a lysine in the DIII-DIV linker. Thus, E1784W may form stable interactions with both residues.

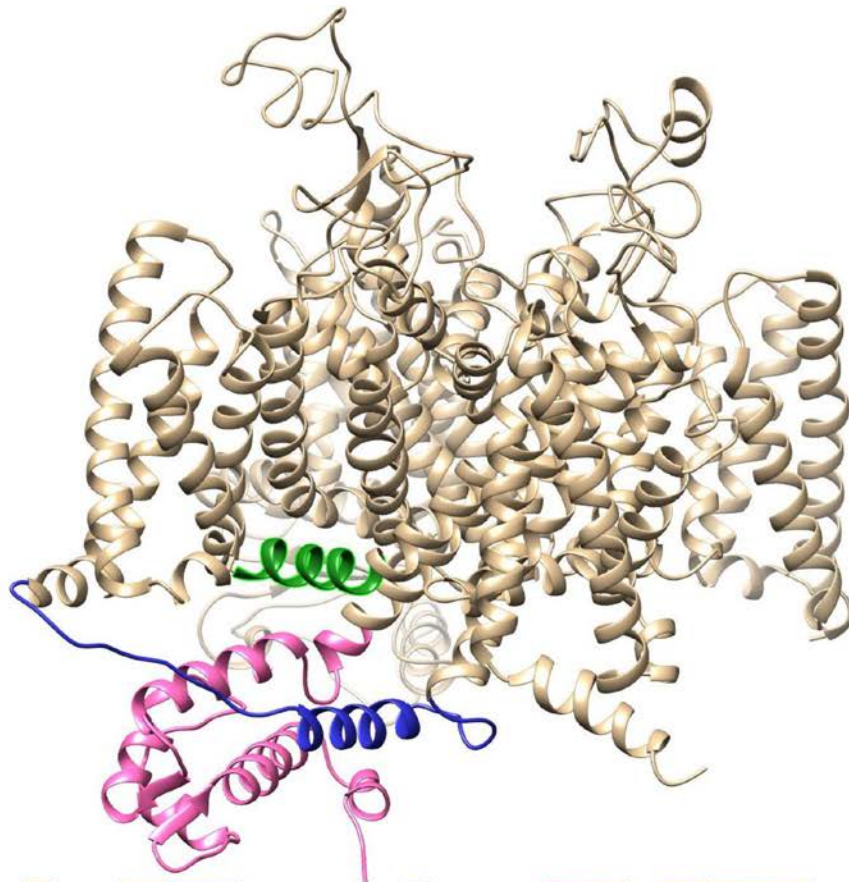
4.4.2. Rapid Fast Inactivation Increases Proton Block of Conductance

These data suggest that more rapid inactivation allows for greater proton-dependent block of peak channel conductance. In the previous chapters I showed that decreasing extracellular pH preferentially decreases conductance in the E1784K mutant compared to E1784 Nav1.5. Given that E1784 is an intracellular residue and the data presented above show that intracellular pH doesn't change in our recordings, this interaction is confusing. The data in this chapter suggest that the proton block of conductance is partially dependent on the fast inactivation rate of the channel. There is a

significant correlation between proton block of channel conductance and the rate of closed state fast inactivation.

Protons slow channel activation by decelerating and depolarizing the movement of the voltage-sensors. Accelerated fast inactivation may cause larger decreases in peak current when activation is slowed by protons, similar to how accelerated fast inactivation decreases peak current through E1784K and depolarizes the GV curve. Therefore, it seems likely that preferential effects of protons will occur in other mutants with accelerated fast inactivation. The list of sodium channel mutants with accelerated inactivation onset includes many of the mixed Brugada syndrome and LQT3 mutants, such as deltaKPQ and deltaK1500 (137,143). Preferential block or depolarization of conductance would further decrease peak sodium current in these channels and exacerbate Brugada syndrome symptoms. Thus, decreasing extracellular pH may be a risk factor for Brugada syndrome-related arrhythmias in many Nav1.5 mutant carriers.

A



B

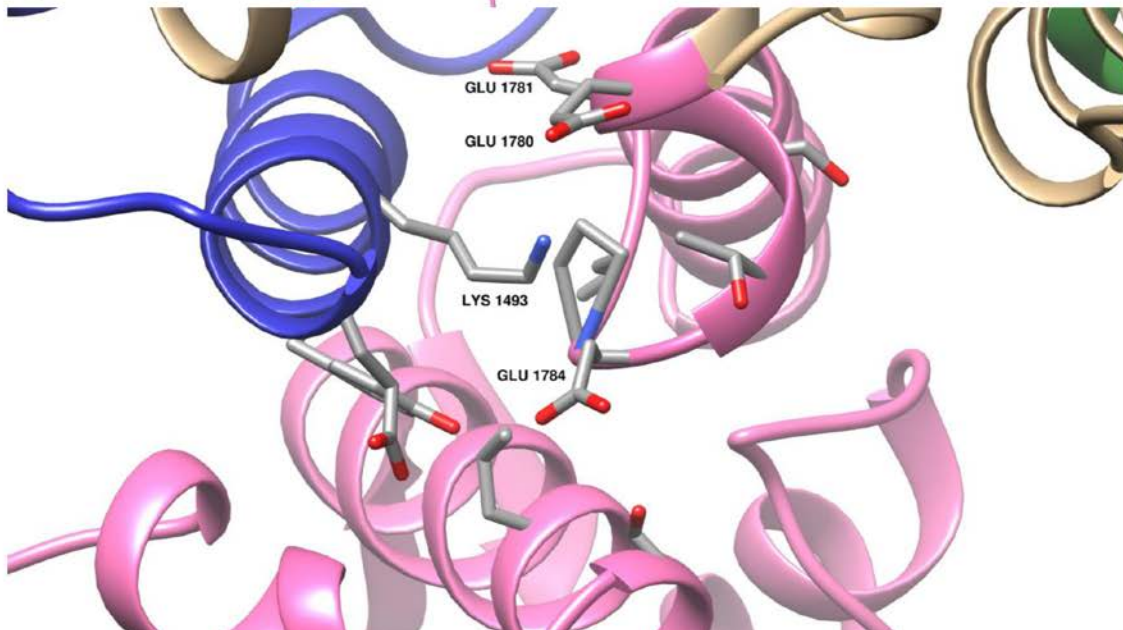


Figure 4.6 A Homology model of Nav1.5 Suggests E1784 Associates With K1493 in the DIII-DIV Linker

A: Homology model of the Nav1.5 sequence on the NavPaS structure. The C-terminus, DIII-DIV linker, and DIVS4-S5 linker are colored pink, blue, and green, respectively. **B:** In the homology model of Nav1.5,

residue E1784 comes within 5 Å of residue K1493 in the DIII-DIV linker. All residues with atoms within 5 Å of E1784 are shown as sticks (PDB ID: 5X0M) (9).

4.4.3. E1784 May Interact with K1493 in the DIII-DIV linker

The C-terminus of Nav1.5 is thought to interact with the DIII-DIV linker either directly, as is shown in the NavPaS structure, or through a calmodulin-mediated interaction (9,46). The proximal C-terminus contains approximately 30 % negative glutamate and aspartate residues, while the DIII-DIV linker contains 12 positively charged residues. Neutralization of the positive charges in the DIII-DIV linker or negative residues in the proximal C-terminus increases the fraction of non-inactivating sodium current (133,275). The E1784K and E1784R charge reversal mutants increase the fraction of non-inactivating sodium current. Given these data, I hypothesize that E1784 normally interacts with a positively charged residue in the DIII-DIV linker. Charge reversal mutants at position 1784 repel the positively charged residue in the DIII-DIV linker, disrupting this interaction and increasing the non-inactivating current. As arginine has a more diffuse charge than lysine, the E1784R mutant causes less of an effect than E1784K.

I constructed a homology model of the Nav1.5 sequence on the NavPaS structure using the MODELLER program run at the University of California San Francisco RBVI (276). This model places residue E1784 within 5 Å of residue K1493 in the DIII-DIV linker. A model constructed on the SWISS-MODEL server shows similar results (277–279). The K1493 residue was previously neutralized along with 6 other lysines in the DIII-DIV linker (275). Neutralization of these 7 lysines increased the fraction of non-inactivating current. Furthermore, the delK1493 mutant is associated with conduction diseases of the heart and drastically decreases channel expression (280).

In our experiments, neutralization of E1784 did not produce non-inactivating currents; however, neutralization of E1773, E1780, E1781, and E1784 in the proximal C-terminus does (133). In the homology model K1493 also comes within 5 Å of E1780 and E1781. Thus, neutralization of E1784 may not be sufficient to disrupt the interaction of K1493 with this pocket of glutamate residues, and a direct repulsion may be necessary.

A future experiment to test this hypothesis would be to make the K1493E/E1784K double mutant and test whether the E1784K-dependent increases in the fraction of non-inactivating current are mitigated.

4.4.4. Conclusion

I have shown that the E1784K-dependent increases in non-inactivating current are dependent on a positive charge at position 1784. Conversely, disruptions of fast inactivation voltage-dependence and rates can occur with changes to size and hydrophobicity. Mutants at position 1784 can alter fast inactivation voltage-dependence and rates without affecting the fraction of non-inactivating current. This is supported by the recent structure of NavPaS that shows the C-terminus interacting with both the DIII-DIV linker and the DIVS4-S5 linker (9). The data presented here also support our previous suggestions that E1784K-dependent shifts in the voltage-dependence of fast inactivation are mirrored in the QV relationship and that E1784K alters channel conductance through changes to fast inactivation. Finally, these data suggest that proton block of maximal conductance is increased by accelerated fast inactivation. As many mixed LQT3 and Brugada syndrome mutants show acceleration of fast inactivation, protons may be an arrhythmogenic trigger in other mutants.

Chapter 5. Conclusion

5.1. Interactions of Residue 1784 in Nav1.5

The data in the previous chapters show that E1784K, the most common Brugada syndrome and LQT3 mixed mutant, modifies channel gating through changes to fast inactivation. Although the conductance-voltage relationship is depolarized in E1784K, the gating charge movement is shifted to more hyperpolarized potentials. This is due to a hyperpolarization of the movement of DIVS4 that also hyperpolarizes the voltage-dependence of fast inactivation. Hyperpolarized and accelerated fast inactivation decreases the peak sodium current and is responsible for the apparent shift in the conductance-voltage relationship.

Ionic and gating current recordings of multiple mutants at residue 1784 suggest that rates and voltage-dependence of fast inactivation can be altered without changing the fraction of non-inactivating current. Non-inactivating current is conferred by a positive charge at position 1784, while changes to the fast inactivation voltage-dependence and rates are sensitive to other amino acid properties. This suggests that the C-terminus has at least two separate mechanisms by which it regulates channel fast inactivation.

The structure of the cockroach sodium channel NavPaS supports previous pull-down assays showing that the C-terminus of the sodium channel directly interacts with the DIII-DIV linker (9,83). Notably, in this structure the C-terminus forms separate interactions with the DIII-DIV linker and with the DIVS4-S5 linker. The proximal C-terminus contains a high concentration of acidic glutamates and aspartates. Conversely the DIII-DIV linker contains several basic lysines and the DIVS4-S5 linker contains 3 basic residues close to the cytoplasmic end of DIVS4. Mutants that neutralize or reverse these charged residues are associated with altered inactivation gating and increases in non-inactivating current (70,77,133,134,270,275). These data suggest that paired

negative and positive amino acids may be the interacting partners between these channel regions.

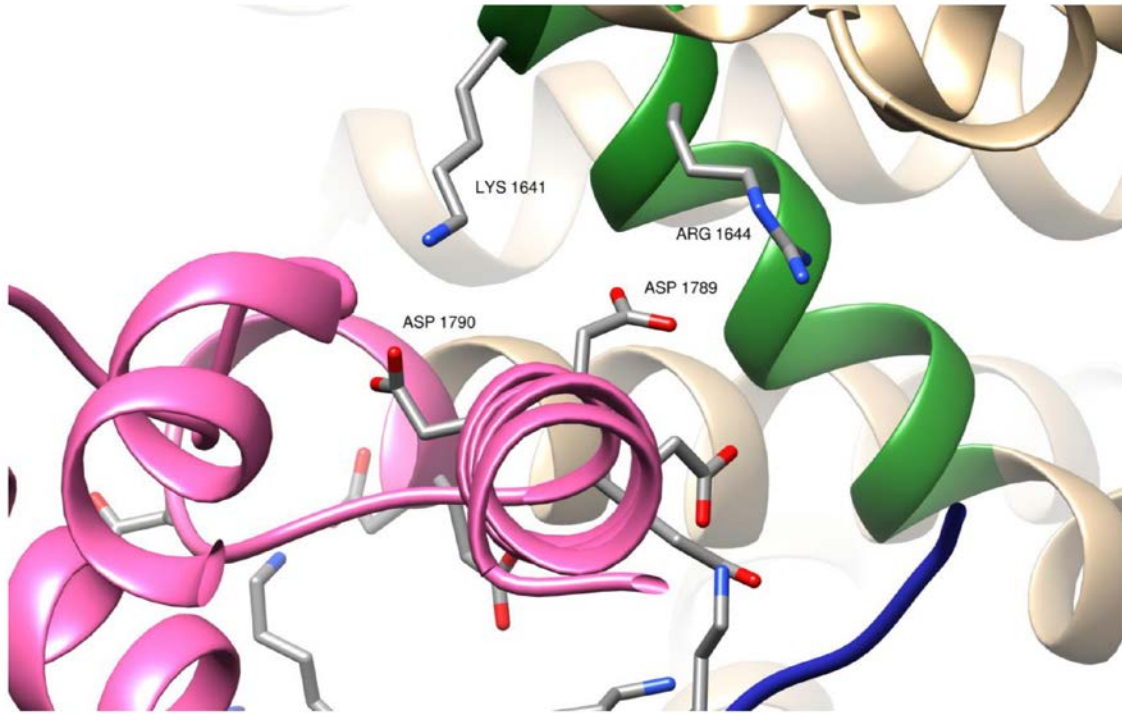


Figure 5.1. A Homology Model of the Nav1.5 C-Terminus Interacting with the DIVS4-S5 linker

Homology model of the Nav1.5 sequence on the NavPaS structure (PDB ID: 5X0M) (281). The C-terminus and DIVS4-S5 linker are colored pink and green, respectively. D1789 in the C-terminus is within 5 Å of R1644 in the DIVS4-S5 linker and D1790 is within 5 Å of K1641.

I used the NavPaS structure as a template for a homology model of Nav1.5. This homology model of the Nav1.5 sequence and the NavPaS structure suggests that two of the basic residues in the DIVS4-S5 linker, K1641 and R1644, are in close proximity to two acidic residues in the C-terminus, D1790 and D1789, respectively (Figure 5.1). Of these residues the R1644H mutant increases the fraction of non-inactivating current and is associated with LQT3 (70); the R1644C mutant depolarizes the conductance voltage relationship, has accelerated fast inactivation recovery, and causes Brugada syndrome (282); and The D1790G mutant increases the fraction of non-inactivating current, hyperpolarizes the voltage-dependence of fast inactivation, accelerates the onset and recovery of fast inactivation, depolarizes the conductance-voltage relationship, and causes LQT3 (160,270).

In this homology model, the DIII-DIV linker is near the C-terminus from residue E1489 to P1509 (Figure 5.2). Of these 21 residues, 13 have been implicated in LQT3 or Brugada syndrome (140,283–285) (see: <http://www.uniprot.org/uniprot/Q14524>). There are 7 basic residues within this span of which 5 are within 5 Å of residues in the proximal C-terminus: K1493, K1500, K1504, K1505, and K1508. The K1493R mutant increases the fraction of non-inactivating current, depolarizes the voltage-dependence of fast inactivation, and is associated with LQT3 and atrial fibrillation (286). The delK1493 mutant decreases channel trafficking, accelerates fast inactivation recovery, slows onset of an intermediate slow inactivation with a time constant of approximately 1s, and is associated with conduction block (280). The delK1500 mutant hyperpolarizes the voltage-dependence of fast inactivation, depolarizes the conductance-voltage relationship, accelerates fast inactivation, increases the fraction of non-inactivating current, and causes Brugada syndrome and LQT3 (137). K1505 is the first residue in the deltaKPQ1505-1507 mutant that hyperpolarizes the voltage-dependence of fast inactivation, depolarizes the conductance-voltage relationship, accelerates fast inactivation onset and recovery, increases the fraction of non-inactivating current, and causes LQT3 and Brugada syndrome (69,70,75,131,132,143,144). K1508 is the second residue in the deltaQKP1507-1509 mutant which increases the fraction of non-inactivating current and causes LQT3 (287).

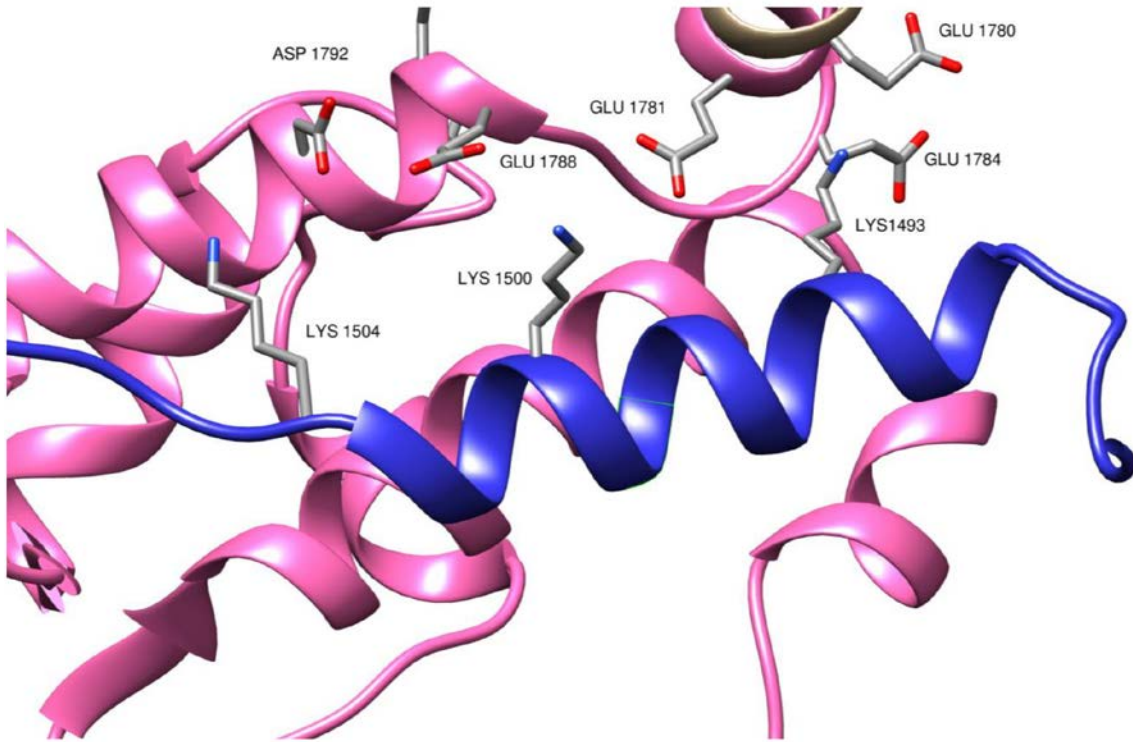


Figure 5.2. Predicted Interactions Between the C-Terminus and the DIII-DIV Linker.

Homology model of the $\text{Na}_v1.5$ sequence on the Na_vPaS structure (PDB ID: 5X0M) (9). The C-terminus and DIII-DIV linker are colored pink and blue, respectively. Acidic residue in the DIII-DIV linker that face the proximal C-terminus are shown as sticks as are basic residue in the proximal C-terminus that face the DIII-DIV linker.

In addition to clinical studies, this region of the channel was studied in a series of experiments from Dr. William Catterall's lab that culminated in the identification of IFMT as the fast inactivation particle (275). Deleting the residues homologous to 1493-1502 resulted in non-functional channels, while deleting residues 1503-1512 severely impairs fast inactivation. Neutralizing the 7 lysines and 2 glutamates within this region increases the fraction of non-inactivating current.

Based on the data in the previous chapters, the homology model presented, and these previously published reports, I suggest that the E1784K mutant disrupts charge-dependent interactions between the C-terminus and the DIII-DIV linker, specifically by repelling K1493. Disrupting this interaction destabilizes the fast-inactivated state and increases the fraction of non-inactivating current through the channel. The E1784Q mutant does not show an increase in non-inactivating current, which suggests removal of

a negative charge is not sufficient to disrupt this interaction and that repulsion by a positive charge at position 1784 is necessary. This may be due to the coordination of K1493 by other C-terminal residues in the area. In our homology model, K1493 is within 5 Å of two other C-terminal glutamates: E1780 and E1781. The E1773Q/E1780Q/E1781Q/E1784Q mutants increase the non-inactivating sodium current to a similar extent as E1784K (133).

Given that mutants can alter fast inactivation rates and voltage-dependence without increasing the fraction of non-inactivating channels, I suggest that modifications at position 1784 can also disrupt the overall structure of this region of the C-terminus, thereby altering the movement of DIVS4. The two neutral residues that most alter channel fast inactivation are valine and tryptophan. The E1784V mutant accelerates both recovery and onset of fast inactivation and hyperpolarizes the fast inactivation voltage-dependence. This may be due to valine being one of the most hydrophobic amino acids. This hydrophobicity may disrupt the overall architecture or stability of the C-terminus and through that alter the fast inactivation process. Conversely, the E1784W mutant depolarizes the fast inactivation voltage-dependence and decelerates the onset of fast inactivation. Despite being an aromatic amino acid, tryptophan is relatively hydrophilic and can participate in hydrogen bonds. The large number of Pi electrons in tryptophan may act to stabilize this region leading to an opposite effect of E1784V (271–274).

My proposed model for the C-terminus is that it binds both the DIII-DIV linker and the DIVS4-S5 linker as suggested by the NavPaS structure. An interaction with the DIII-DIV linker stabilizes the binding of the IFMT, which leads to a channel that inactivates fully. The interaction with the DIVS4-S5 linker stabilizes the deactivated state of the DIVS4. I propose that mutants which disrupt the interaction with the DIII-DIV linker, like E1784K, increase the fraction of non-inactivating current, and mutants that disrupt the interaction with the DIVS4-S5 linker allow the DIVS4 to activate more rapidly and at more hyperpolarized membrane potentials.

5.2. Role of Protons in E1784K Arrhythmia

These studies confirm my earlier results showing protons have large effects on the E1784K channel. As with my study in Chinese Hamster Ovary cells, increasing extracellular protons causes larger depolarizations of conductance, block of peak conductance, and increases in non-inactivating current in E1784K channels compared to WT (2). These effects would be expected to exacerbate symptoms of both Brugada syndrome and LQT3, which are characterized by decreased peak sodium currents and increased non-inactivating sodium currents, respectively. Given that many conditions associated with arrhythmia and sudden cardiac death involve acidemia, this supports the hypothesis that acidemia may act as an arrhythmogenic trigger in those with Brugada syndrome or LQT3 mutants.

Contrary to my initial expectation, the effect of protons on Nav1.5 gating currents was not amplified by the E1784K mutant. Decreasing extracellular pH causes a similar depolarization of voltage-sensor activation and deactivation in the presence of the E1784K mutant. This suggests that the amplified effect of protons on conductance are due to a synergistic effect of protons and the E1784K mutant. I suggest that the increased depolarization of conductance and increased proton block of maximal conductance in E1784K are due to the proton slowing of activation in the presence of accelerated fast inactivation. In the presence of the rapid fast inactivation of the E1784K mutant, the channels have less time to activate before fast inactivation occurs. This accelerated inactivation prematurely attenuates current. When activation is slowed by extracellular protons, the effects of this accelerated fast inactivation are amplified, leading to an even larger shift in the conductance-voltage relationship and a larger block of peak channel conductance. This hypothesis is supported by recordings of fast inactivation-deficient channels that show protons depolarize conductance to an equal extent in IFM/QQQ and IFM/QQQ/E1784K channels.

5.3. Future Directions

My theories about how E1784K alters gating and protons sensitivity may be applicable to other disease-causing mutants within this region of the channel. Many of the mixed Brugada syndrome and LQT3 mutants occur in the channel structures underlying fast inactivation and cause similar effects on channel gating. All of 1795insD, deltaKPQ1505-1507, delF1617, and deltaK1500 cause acceleration of fast inactivation, hyperpolarization of the voltage-dependence of fast inactivation, and increased non-inactivating sodium current (70,75,137,138,143,145,268,288). Proton-induced slowing of activation could cause similar preferential effects on conductance in these mutants. A reasonable future project is, therefore, to see whether these effects are generalizable to other mutants. Testing the effects of protons on ionic currents through other mixed syndrome mutants, and the effects of these mutants on gating charge movement may show that mixed syndrome mutants share common impairments. This would allow for more targeted drug development to treat mixed syndrome patients.

One type of drug that may play an important role in these patients is arylsulfonamides. A recent study showed that an Nav1.7-specific small molecule agonist acts by binding one of the gating charges in the DIVS4 (49). This binding effectively traps the voltage-sensor in the upward conformation and slows recovery from inactivation. Similar compounds may be useful in the treatment of mutants which alter channel fast inactivation. A drug which targets DIVS4 and slows both the outward and inward movements may counteract the accelerated rate of fast inactivation in these mutants. Another potentially productive direction would be to investigate voltage-sensor trapping by toxins. ATXII is a neurotoxin derived from the venom of *Anemonia sulcata* and is used at high concentrations as a model of LQT3 (159). At high concentrations ATXII induces a large non-inactivating sodium current which elongates the action potential and may cause afterdepolarizations (289,290). Interestingly at concentrations as low as 1nM, ATXII slows inactivation onset of sodium channels (289). Although many toxins are potentially fatal and, therefore, not feasible treatment options, these types of fast inactivation specific modifiers may be useful in designing drugs to specifically target DIVS4.

A less clinically-oriented study is to find interacting partners of E1784K. I have predicted that E1784 interacts with a lysine in the DIII-DIV linker, possibly K1493, but as this prediction is based on a homology model, it should be tested in Nav1.5. An experiment in which the lysines in the DIII-DIV linker are serially mutated to glutamates in the presence of the E1784K mutant could determine the exact pairing. Mutation of the DIII-DIV linker partner lysine to a glutamate should restore some interaction with E1784K, thus reducing the non-inactivating current compared to E1784K. Conversely, mutating the partner lysine to glutamate in the normal E1784 channel should disrupt this interaction and produce a small non-inactivating current. Our preliminary experiments on this residue indicate that the K1493E mutant causes a non-inactivating current (Figure 5.3); however, the K1493E/E1784K double mutant has a similar level of non-inactivating current compared to wild-type channels. These data support the hypothesis that E1784 normally interacts with residue K1493, the E1784K mutant disrupts this interaction, and the K1493E/E1784K double mutant restores this interaction.

Of interest will be whether the double glutamate channel also has altered fast inactivation voltage-dependence or kinetics. If not, this would further suggest two separate interactions that are disrupted by the E1784K mutant. However, if the double glutamate mutant altered fast inactivation, this would imply that destabilizing a C-terminal DIII-DIV linker interaction is sufficient to also alter DIVS4 movement. If two interactions are suggested by this experiment, the E1784I and E1784L mutant could be used to test whether hydrophobicity is indeed the key factor in modifications of channel gating by E1784V.

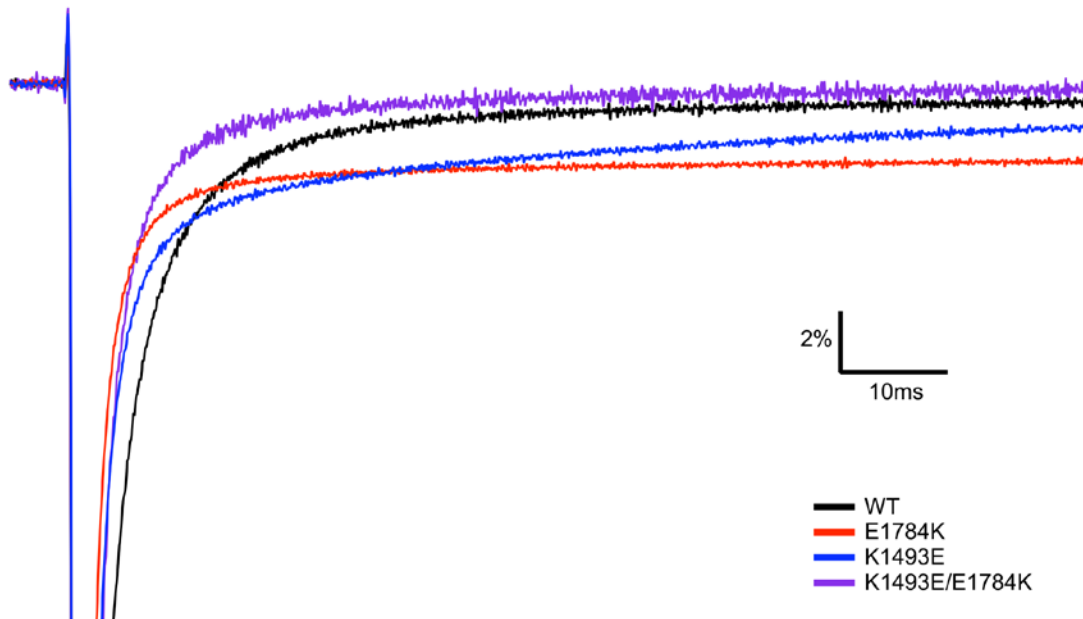


Figure 5.3 Non-Inactivating Current of the K1493E/E1784K $Na_v1.5$ Mutant

Normalized sample currents recorded at -20mV from wild-type, K1493E, E1784K, and K1493E/E1784K $Na_v1.5$ at extracellular pH 7.4. The E1784K and K1493E mutants both appear to increase the fraction of non-inactivating current. The K1493E/E1784K double mutant has similar amounts of non-inactivating current to wild-type channels.

5.4. Limitations

One of the primary limitations of these studies is shared with many others: the use of a heterologous expression system. All the experiments were performed in *Xenopus* oocytes, which do not fully recapitulate the channel in native cardiac tissue. In ventricular cardiomyocytes, the voltage-gated sodium is modulated by numerous cytoskeletal proteins and accessory subunits (291). Experiments in ventricular myocytes, therefore best recapitulate the function of the cardiac sodium channel in its native environment. However, experiments in cardiomyocytes also have drawbacks compared to expression systems. To accurately measure the current through the voltage-gated sodium channel, a cornucopia of drugs must be applied to block the other currents in the tissue. Additionally, using cardiomyocytes would not allow for gating current and voltage-sensor fluorescence measurements, which require channel overexpression. The *Xenopus laevis* expression system was used in these experiments as I wished to perform a

biophysical characterization rather than a clinical one and expression systems allow for better characterization of individual currents.

A more clinically-oriented follow-up project could test the effects of decreasing extracellular pH on cardiomyocytes expressing E1784K Nav1.5. The best model would be cardiomyocytes from the explanted heart of an E1784K patient, however these may be difficult to obtain. A more feasible project would be to create a human induced pluripotent stem cell (hiPSC) line from an E1784K carrier and then differentiate these cells to cardiomyocytes. The action potential characteristics of these cells could then be compared to cardiomyocytes derived from wildtype hiPSCs. Or if patient tissue is completely unavailable, use CRISPR-Cas9 to introduce the E1784K mutant into a normal hiPSC line.

A limitation of the Peters-Ruben model is that the simulations presented in chapter 3 shows a small depolarization in the charge voltage relationship. The algorithm used to fit DIIS4 activation and deactivation rates originally hyperpolarized the DIIS4 movement substantially more than the hyperpolarization used in the model for this chapter. At the time this model was constructed, the only fluorescence data available was from Nav1.4 in which the DIIS4 is hyperpolarized by <20 mV compared to DIS4 and DIIS4 (53). The more recent fluorescence data from Nav1.5 show that while the midpoints of DIS4 and DIIS4 activation are hyperpolarized by 20-30 mV compared to the conductance-voltage relationship, the DIIS4 is hyperpolarized by 70 mV (68). When an additional 30 mV hyperpolarization is included for DIIS4 movement in our model, the simulated QV curve and GV curve provide better fits to the experimental data (Figure 5.4).

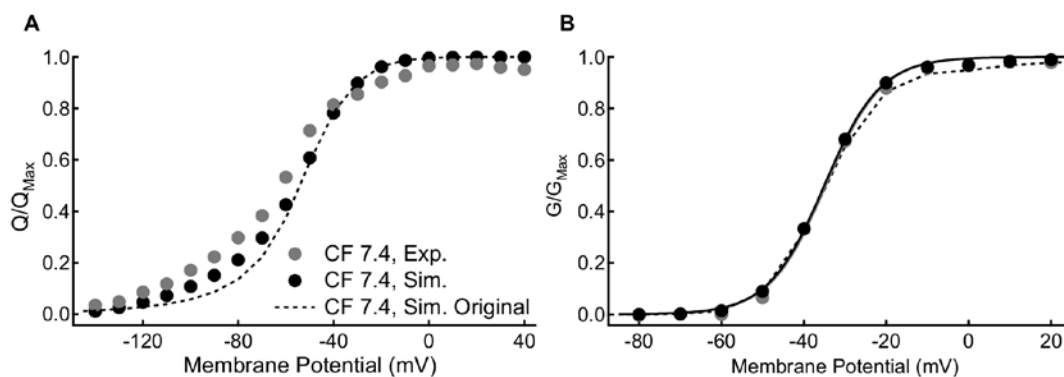


Figure 5.4. Hyperpolarizing DIIS4 Movement in the Peters-Ruben Model Improves the Fit to Experimental Data.

A: Simulated voltage-dependence of C373F Nav1.5 gating charge activation plotted against experimental data from chapter 2. Black circles are simulated using the Peters-Ruben model with the rates of DIIS4 activation and deactivation hyperpolarized by 30 mV, while the black dotted line is simulated with the original parameters in chapter 3. **B:** Simulated voltage-dependence of C373F Nav1.5 conductance plotted against experimental data from chapter 2. Black circles are simulated using the Peters-Ruben model with the rates of DIIS4 activation and deactivation hyperpolarized by 30 mV, while the black dotted line is simulated with the original parameters in chapter 3

Unfortunately, these studies were also hampered by a lack of structural data. These three studies were all designed and many of the experiments were carried out prior to the publication of the first two eukaryotic sodium channel structures earlier this year (10,281). Even with these structures, my structural inferences should be treated with caution. The channel C-terminus is not resolved in the eel structure, which shares a higher sequence homology with mammalian channels, thus I was forced to use the NavPaS structure for homology modelling and predictions. The NavPaS structure shares only 40 % homology with human sodium channels, although the negative charges in the proximal C-terminus are relatively well conserved. This introduces error into our predictions of C-terminal structure and it would not be surprising if E1784 was positioned differently in the C-terminal structure in mammalian channels. This limitation, unfortunately will not be fully resolved until a structure of a channel with higher sequence homology is resolved.

5.5. Clinical Significance

The data presented here provide a model of how mixed syndrome mutants alter seemingly all aspects of channel gating. The finding that E1784K acts primarily through alterations to the fast inactivation machinery may be generalizable to other mixed syndrome mutants, which show similar alterations to gating and occur in regions of the channel associated with fast inactivation. These data may allow for more targeted drug design to treat both the gain-of-function and loss-of-function effects of these mutants. Currently implantable cardio defibrillators are the only proven treatment for Brugada syndrome (292,293). The website [Brugadadrugs.org](https://www.brugadadrugs.org) lists drugs with potential anti-arrhythmic effects for Brugada syndrome patients including Quinidine, Isoproterenol, and Bepridil (<https://www.brugadadrugs.org/>). Of these, Quinidine and Isoproterenol are contraindicated in LQTS and Bepridil is no longer sold in the USA. The first-line pharmaceutical for LQT3 is mexiletine, which may have mixed effects. Mexiletine hyperpolarizes fast inactivation and exerts both a tonic and use-dependent block of Nav1.5 channels in heterologous expression systems (294); However, mexiletine is not associated with ST-segment elevation in Brugada syndrome patients (295). Mexiletine may rescue trafficking in some Brugada syndrome mutants thereby increasing peak sodium current (296,297). In one case, rescue of trafficking further prolonged QT interval in a patient with the F1473S LQT3 mutant by increasing the number of non-inactivating channels trafficked to the cell membrane (298). This case illustrates that mexiletine may not be effective for all mutants, particularly those altering peak and non-inactivating current (167).

The data presented also highlight the effects of protons on mutant sodium channels. In combination with other studies from our lab this suggests that triggers for arrhythmia may be mutant specific and lifestyle modifications may differ based on this (75,243). In many LQT3 carriers, arrhythmia occurs during sleep (163). This does not apply to all patients. Studies on LQT3 mutants show that increased intracellular calcium, which occurs during exercise induced tachycardia, reduces non-inactivating currents (75,76). Thus, exercise may be therapeutic. In other patients exercise acts as a trigger which unmasks a type I Brugada syndrome ECG (205,208,209). In the E1784K mutant

in particular, intracellular calcium was not found to reduce non-inactivating currents (75). In conjunction with temperature and proton-dependent increases in non-inactivating current, exercise may be pro-arrhythmic in E1784K carriers (243).

5.6. Concluding Remarks

Research from the past two decades has shown that diseases of sodium channels show a high degree of overlap. Underscoring the difficulty of treating these diseases is the fact that single missense mutants may alter channel activation, fast inactivation, slow inactivation, and non-inactivating current. Using a reductionist technique of modelling, gating current measurements, and voltage-sensor measurements in addition to standard ionic current measurements allowed me to ascertain that E1784K interferes with key interactions in the channel inactivation machinery. This disruption of fast inactivation is responsible for the loss-of-function effects that cause Brugada syndrome and the gain-of-function effects that cause LQT3. Given the similarity in biophysics between E1784K and other mixed syndrome mutants, this may be a common mechanism for dysfunction and a possible target site for future therapeutics.

References

1. Peters CH, Ruben PC. Introduction to sodium channels. *Handb Exp Pharmacol*. 2014;221:1–6.
2. Peters CH, Abdelsayed M, Ruben PC. Triggers for arrhythmogenesis in the Brugada and long QT 3 syndromes. *Prog Biophys Mol Biol*. 2016 Jan;120(1–3):77–88.
3. Peters CH, Yu A, Zhu W, Silva JR, Ruben PC. Depolarization of the conductance-voltage relationship in the NaV1.5 mutant, E1784K, is due to altered fast inactivation. *PLOS ONE* [Internet]. 2017 Sep 12 [cited 2017 Oct 17];12(9):e0184605. Available from: <http://journals.plos.org/plosone/article?id=10.1371/journal.pone.0184605>
4. Catterall WA, Goldin AL, Waxman SG. International Union of Pharmacology. XLVII. Nomenclature and structure-function relationships of voltage-gated sodium channels. *Pharmacol Rev*. 2005 Dec;57(4):397–409.
5. Hodgkin AL, Huxley AF. The dual effect of membrane potential on sodium conductance in the giant axon of Loligo. *J Physiol* [Internet]. 1952 Apr 28;116(4):497–506. Available from: <https://www.ncbi.nlm.nih.gov/pmc/articles/PMC1392212/>
6. Hodgkin AL, Huxley AF. Currents carried by sodium and potassium ions through the membrane of the giant axon of Loligo. *J Physiol* [Internet]. 1952 Apr 28;116(4):449–72. Available from: <https://www.ncbi.nlm.nih.gov/pmc/articles/PMC1392213/>
7. Hodgkin AL, Huxley AF. The components of membrane conductance in the giant axon of Loligo. *J Physiol* [Internet]. 1952 Apr 28;116(4):473–96. Available from: <https://www.ncbi.nlm.nih.gov/pmc/articles/PMC1392209/>
8. Hodgkin AL, Huxley AF. A quantitative description of membrane current and its application to conduction and excitation in nerve. *J Physiol* [Internet]. 1952 Aug 28 [cited 2015 Apr 9];117(4):500–44. Available from: <http://www.ncbi.nlm.nih.gov/pmc/articles/PMC1392413/>
9. Shen H, Zhou Q, Pan X, Li Z, Wu J, Yan N. Structure of a eukaryotic voltage-gated sodium channel at near-atomic resolution. *Science* [Internet]. 2017 Mar 3 [cited 2017 Apr 5];355(6328):eaal4326. Available from: <http://science.sciencemag.org/content/355/6328/eaal4326>

10. Yan Z, Zhou Q, Wang L, Wu J, Zhao Y, Huang G, et al. Structure of the Nav1.4- β 1 Complex from Electric Eel. *Cell*. 2017 Jul 27;170(3):470–482.e11.
11. Bernstein J. Untersuchungen zur Thermodynamik der bioelektrischen Ströme. *Arch Für Gesamte Physiol Menschen Tiere* [Internet]. 1902 Nov 1 [cited 2017 Oct 19];92(10–12):521–62. Available from: <https://link-springer-com.proxy.lib.sfu.ca/article/10.1007/BF01790181>
12. Cole KS, Curtis HJ. ELECTRIC IMPEDANCE OF THE SQUID GIANT AXON DURING ACTIVITY. *J Gen Physiol*. 1939 May 20;22(5):649–70.
13. Hodgkin AL, Huxley AF, Katz B. Measurement of current-voltage relations in the membrane of the giant axon of *Loligo*. *J Physiol* [Internet]. 1952 Apr 28;116(4):424–48. Available from: <https://www.ncbi.nlm.nih.gov/pmc/articles/PMC1392219/>
14. Huxley AF. Hodgkin and the action potential 1935–1952. *J Physiol* [Internet]. 2002 Jan 1;538(Pt 1):2. Available from: <https://www.ncbi.nlm.nih.gov/pmc/articles/PMC2290015/>
15. Armstrong CM, Bezanilla F. Currents related to movement of the gating particles of the sodium channels. *Nature*. 1973 Apr 13;242(5398):459–61.
16. Armstrong CM, Bezanilla F. Charge movement associated with the opening and closing of the activation gates of the Na channels. *J Gen Physiol* [Internet]. 1974 [cited 2015 Apr 24];63(5):533–552. Available from: <http://jgp.rupress.org/content/63/5/533.short>
17. Yang N, Horn R. Evidence for voltage-dependent S4 movement in sodium channels. *Neuron* [Internet]. 1995 Jul 1;15(1):213–8. Available from: <http://www.sciencedirect.com/science/article/pii/0896627395900780>
18. Kontis KJ, Rounaghi A, Goldin AL. Sodium Channel Activation Gating Is Affected by Substitutions of Voltage Sensor Positive Charges in All Four Domains. *J Gen Physiol* [Internet]. 1997 Oct 1 [cited 2016 Jun 24];110(4):391–401. Available from: <http://www.ncbi.nlm.nih.gov/pmc/articles/PMC2229375/>
19. Yarov-Yarovoy V, DeCaen PG, Westenbroek RE, Pan C-Y, Scheuer T, Baker D, et al. Structural basis for gating charge movement in the voltage sensor of a sodium channel. *Proc Natl Acad Sci U S A*. 2012 Jan 10;109(2):E93–102.
20. Capes DL, Goldschen-Ohm MP, Arcisio-Miranda M, Bezanilla F, Chanda B. Domain IV voltage-sensor movement is both sufficient and rate limiting for fast inactivation in sodium channels. *J Gen Physiol* [Internet]. 2013 Jul 29 [cited 2015 Apr 24];142(2):101–12. Available from: <http://www.jgp.org/cgi/doi/10.1085/jgp.201310998>

21. Heinemann SH, Terlau H, Imoto K. Molecular basis for pharmacological differences between brain and cardiac sodium channels. *Pflüg Arch* [Internet]. 1992 Oct 1 [cited 2015 Apr 25];422(1):90–2. Available from: <http://link.springer.com/article/10.1007/BF00381519>
22. Satin J, Kyle JW, Chen M, Bell P, Cribbs LL, Fozzard HA, et al. A mutant of TTX-resistant cardiac sodium channels with TTX-sensitive properties. *Science*. 1992 May 22;256(5060):1202–5.
23. Backx PH, Yue DT, Lawrence JH, Marban E, Tomaselli GF. Molecular localization of an ion-binding site within the pore of mammalian sodium channels. *Science*. 1992 Jul 10;257(5067):248–51.
24. Gosselin-Badaroudine P, Keller DI, Huang H, Pouliot V, Chatelier A, Osswald S, et al. A proton leak current through the cardiac sodium channel is linked to mixed arrhythmia and the dilated cardiomyopathy phenotype. *PloS One*. 2012;7(5):e38331.
25. Chandler NJ, Greener ID, Tellez JO, Inada S, Musa H, Molenaar P, et al. Molecular architecture of the human sinus node: insights into the function of the cardiac pacemaker. *Circulation*. 2009 Mar 31;119(12):1562–75.
26. Verkerk AO, Remme CA, Schumacher CA, Scicluna BP, Wolswinkel R, de Jonge B, et al. Functional Nav1.8 channels in intracardiac neurons: the link between SCN10A and cardiac electrophysiology. *Circ Res*. 2012 Jul 20;111(3):333–43.
27. Haufe V, Cordeiro JM, Zimmer T, Wu YS, Schiccitano S, Benndorf K, et al. Contribution of neuronal sodium channels to the cardiac fast sodium current INa is greater in dog heart Purkinje fibers than in ventricles. *Cardiovasc Res*. 2005 Jan 1;65(1):117–27.
28. Westenbroek RE, Bischoff S, Fu Y, Maier SKG, Catterall WA, Scheuer T. Localization of sodium channel subtypes in mouse ventricular myocytes using quantitative immunocytochemistry. *J Mol Cell Cardiol*. 2013 Nov;64:69–78.
29. Facer P, Punjabi PP, Abrari A, Kaba RA, Severs NJ, Chambers J, et al. Localisation of SCN10A gene product Na(v)1.8 and novel pain-related ion channels in human heart. *Int Heart J*. 2011;52(3):146–52.
30. van den Boogaard M, Smemo S, Burnicka-Turek O, Arnolds DE, van de Werken HJG, Klous P, et al. A common genetic variant within SCN10A modulates cardiac SCN5A expression. *J Clin Invest*. 2014 Apr;124(4):1844–52.
31. Hu D, Barajas-Martínez H, Pfeiffer R, Dezi F, Pfeiffer J, Buch T, et al. Mutations in SCN10A are responsible for a large fraction of cases of Brugada syndrome. *J Am Coll Cardiol*. 2014 Jul 8;64(1):66–79.

32. Black JA, Liu S, Tanaka M, Cummins TR, Waxman SG. Changes in the expression of tetrodotoxin-sensitive sodium channels within dorsal root ganglia neurons in inflammatory pain. *Pain* [Internet]. 2004 Apr 1;108(3):237–47. Available from: <http://www.sciencedirect.com/science/article/pii/S0304395904000028>
33. Huang X, Mao Q, Lin Y, Feng J, Jiang J. Expression of Voltage-Gated Sodium Channel Nav1.3 Is Associated with Severity of Traumatic Brain Injury in Adult Rats. *J Neurotrauma* [Internet]. 2013 Jan 1;30(1):39–46. Available from: <https://www.ncbi.nlm.nih.gov/pmc/articles/PMC3530945/>
34. Yanni J, Tellez JO, Maczewski M, Mackiewicz U, Beresewicz A, Billeter R, et al. Changes in ion channel gene expression underlying heart failure-induced sinoatrial node dysfunction. *Circ Heart Fail*. 2011 Jul;4(4):496–508.
35. Goldin AL. Diversity of Mammalian Voltage-Gated Sodium Channels. *Ann N Y Acad Sci* [Internet]. 1999 Apr 1 [cited 2016 Aug 31];868(1):38–50. Available from: <http://onlinelibrary.wiley.com/doi/10.1111/j.1749-6632.1999.tb11272.x/abstract>
36. Ahmed CM, Ware DH, Lee SC, Patten CD, Ferrer-Montiel AV, Schinder AF, et al. Primary structure, chromosomal localization, and functional expression of a voltage-gated sodium channel from human brain. *Proc Natl Acad Sci U S A* [Internet]. 1992 Sep [cited 2017 Oct 19];89(17):8220–4. Available from: <http://europepmc.org/abstract/MED/1325650>
37. Noda M, Shimizu S, Tanabe T, Takai T, Kayano T, Ikeda T, et al. Primary structure of *Electrophorus electricus* sodium channel deduced from cDNA sequence. *Nature* [Internet]. 1984 Nov 8 [cited 2016 Jun 24];312(5990):121–7. Available from: <http://www.nature.com/nature/journal/v312/n5990/abs/312121a0.html>
38. Payandeh J, Scheuer T, Zheng N, Catterall WA. The crystal structure of a voltage-gated sodium channel. *Nature* [Internet]. 2011 Jul 21 [cited 2017 Jul 28];475(7356):353–8. Available from: <https://www.nature.com/nature/journal/v475/n7356/full/nature10238.html>
39. Bezanilla F. Voltage Sensor Movements. *J Gen Physiol* [Internet]. 2002 Oct;120(4):465–73. Available from: <https://www.ncbi.nlm.nih.gov/pmc/articles/PMC2229527/>
40. Hirschberg B, Rovner A, Lieberman M, Patlak J. Transfer of twelve charges is needed to open skeletal muscle Na⁺ channels. *J Gen Physiol*. 1995 Dec;106(6):1053–68.
41. Aggarwal SK, MacKinnon R. Contribution of the S4 segment to gating charge in the Shaker K⁺ channel. *Neuron*. 1996 Jun;16(6):1169–77.

42. Catterall WA. Ion Channel Voltage Sensors: Structure, Function, and Pathophysiology. *Neuron* [Internet]. 2010 Sep 23;67(6):915–28. Available from: <https://www.ncbi.nlm.nih.gov/pmc/articles/PMC2950829/>
43. Detta N, Frisso G, Salvatore F. The multi-faceted aspects of the complex cardiac Nav1.5 protein in membrane function and pathophysiology. *Biochim Biophys Acta BBA - Proteins Proteomics* [Internet]. 2015 Oct 1;1854(10, Part A):1502–9. Available from: <http://www.sciencedirect.com/science/article/pii/S1570963915002022>
44. Pettersen EF, Goddard TD, Huang CC, Couch GS, Greenblatt DM, Meng EC, et al. UCSF Chimera--a visualization system for exploratory research and analysis. *J Comput Chem*. 2004 Oct;25(13):1605–12.
45. Chagot B, Potet F, Balsler JR, Chazin WJ. Solution NMR Structure of the C-terminal EF-hand Domain of Human Cardiac Sodium Channel NaV1.5. *J Biol Chem* [Internet]. 2009 Mar 6 [cited 2015 Apr 25];284(10):6436–45. Available from: <http://www.jbc.org/content/284/10/6436>
46. Sarhan MF, Tung C-C, Petegem FV, Ahern CA. Crystallographic basis for calcium regulation of sodium channels. *Proc Natl Acad Sci* [Internet]. 2012 Feb 28 [cited 2015 Apr 26];109(9):3558–63. Available from: <http://www.pnas.org/content/109/9/3558>
47. Wang C, Chung BC, Yan H, Lee S-Y, Pitt GS. Crystal structure of the ternary complex of a Nav C-terminal domain, a fibroblast growth factor homologous factor, and calmodulin. *Struct Lond Engl* 1993 [Internet]. 2012 Jul 3;20(7):1167–76. Available from: <https://www.ncbi.nlm.nih.gov/pmc/articles/PMC3610540/>
48. Payandeh J, Gamal El-Din TM, Scheuer T, Zheng N, Catterall WA. Crystal structure of a voltage-gated sodium channel in two potentially inactivated states. *Nature*. 2012 Jun 7;486(7401):135–9.
49. Ahuja S, Mukund S, Deng L, Khakh K, Chang E, Ho H, et al. Structural basis of Nav1.7 inhibition by an isoform-selective small-molecule antagonist. *Science*. 2015 Dec 18;350(6267):aac5464.
50. Groome JR, Winston V. S1–S3 counter charges in the voltage sensor module of a mammalian sodium channel regulate fast inactivation. *J Gen Physiol* [Internet]. 2013 May;141(5):601–18. Available from: <https://www.ncbi.nlm.nih.gov/pmc/articles/PMC3639575/>
51. Yarov-Yarovoy V, DeCaen PG, Westenbroek RE, Pan C-Y, Scheuer T, Baker D, et al. Structural basis for gating charge movement in the voltage sensor of a sodium

- channel. Proc Natl Acad Sci U S A [Internet]. 2012 Jan 10;109(2):E93–102. Available from: <https://www.ncbi.nlm.nih.gov/pmc/articles/PMC3258622/>
52. Catterall WA. Structure and Function of Voltage-Gated Sodium Channels at Atomic Resolution. Exp Physiol [Internet]. 2014 Jan;99(1). Available from: <https://www.ncbi.nlm.nih.gov/pmc/articles/PMC3885250/>
 53. Chanda B. Tracking Voltage-dependent Conformational Changes in Skeletal Muscle Sodium Channel during Activation. J Gen Physiol [Internet]. 2002 Oct 29 [cited 2015 Apr 24];120(5):629–45. Available from: <http://www.jgp.org/cgi/doi/10.1085/jgp.20028679>
 54. Rayner MD, Starkus JG, Ruben PC, Alicata DA. Voltage-sensitive and solvent-sensitive processes in ion channel gating. Kinetic effects of hyperosmolar media on activation and deactivation of sodium channels. Biophys J [Internet]. 1992 Jan 1 [cited 2016 Sep 9];61(1):96–108. Available from: <http://www.sciencedirect.com/science/article/pii/S0006349592818192>
 55. Sun YM, Favre I, Schild L, Moczydlowski E. On the structural basis for size-selective permeation of organic cations through the voltage-gated sodium channel. Effect of alanine mutations at the DEKA locus on selectivity, inhibition by Ca²⁺ and H⁺, and molecular sieving. J Gen Physiol. 1997 Dec;110(6):693–715.
 56. Favre I, Moczydlowski E, Schild L. On the structural basis for ionic selectivity among Na⁺, K⁺, and Ca²⁺ in the voltage-gated sodium channel. Biophys J. 1996 Dec;71(6):3110–25.
 57. Lipkind GM, Fozzard HA. Voltage-gated Na channel selectivity: the role of the conserved domain III lysine residue. J Gen Physiol. 2008 Jun;131(6):523–9.
 58. Heinemann SH, Terlau H, Stühmer W, Imoto K, Numa S. Calcium channel characteristics conferred on the sodium channel by single mutations. Nature. 1992 Apr 2;356(6368):441–3.
 59. Terlau H, Heinemann SH, Stühmer W, Pusch M, Conti F, Imoto K, et al. Mapping the site of block by tetrodotoxin and saxitoxin of sodium channel II. FEBS Lett. 1991 Nov 18;293(1–2):93–6.
 60. Fozzard HA, Lipkind GM. The Tetrodotoxin Binding Site Is within the Outer Vestibule of the Sodium Channel. Mar Drugs [Internet]. 2010 Feb 1;8(2):219–34. Available from: <https://www.ncbi.nlm.nih.gov/pmc/articles/PMC2852835/>
 61. Armstrong CM, Bezanilla F, Rojas E. Destruction of sodium conductance inactivation in squid axons perfused with pronase. J Gen Physiol [Internet]. 1973 [cited 2015 Apr 24];62(4):375–391. Available from: <http://jgp.rupress.org/content/62/4/375.abstract>

62. West JW, Patton DE, Scheuer T, Wang Y, Goldin AL, Catterall WA. A cluster of hydrophobic amino acid residues required for fast Na⁺-channel inactivation. *Proc Natl Acad Sci* [Internet]. 1992 [cited 2015 Apr 25];89(22):10910–10914. Available from: <http://www.pnas.org/content/89/22/10910.short>
63. McPhee JC, Ragsdale DS, Scheuer T, Catterall WA. A critical role for the S4-S5 intracellular loop in domain IV of the sodium channel alpha-subunit in fast inactivation. *J Biol Chem*. 1998 Jan 9;273(2):1121–9.
64. Smith MR, Goldin AL. Interaction between the sodium channel inactivation linker and domain III S4-S5. *Biophys J* [Internet]. 1997 Oct;73(4):1885–95. Available from: <https://www.ncbi.nlm.nih.gov/pmc/articles/PMC1181089/>
65. Goldin AL. Mechanisms of sodium channel inactivation. *Curr Opin Neurobiol*. 2003 Jun;13(3):284–90.
66. Bezanilla F, Armstrong CM. Inactivation of the sodium channel. I. Sodium current experiments. *J Gen Physiol*. 1977 Nov;70(5):549–66.
67. Cota G, Armstrong CM. Sodium channel gating in clonal pituitary cells. The inactivation step is not voltage dependent. *J Gen Physiol* [Internet]. 1989 [cited 2015 Apr 24];94(2):213–232. Available from: <http://jgp.rupress.org/content/94/2/213.abstract>
68. Varga Z, Zhu W, Schubert AR, Pardieck JL, Krumholz A, Hsu EJ, et al. Direct Measurement of Cardiac Na⁺ Channel Conformations Reveals Molecular Pathologies of Inherited Mutations. *Circ Arrhythm Electrophysiol* [Internet]. 2015 Oct 1 [cited 2017 Feb 22];8(5):1228–39. Available from: <http://circep.ahajournals.org/content/8/5/1228>
69. Wang Q, Shen J, Splawski I, Atkinson D, Li Z, Robinson JL, et al. SCN5A mutations associated with an inherited cardiac arrhythmia, long QT syndrome. *Cell*. 1995 Mar 10;80(5):805–11.
70. Wang DW, Yazawa K, George AL, Bennett PB. Characterization of human cardiac Na⁺ channel mutations in the congenital long QT syndrome. *Proc Natl Acad Sci* [Internet]. 1996 Nov 12 [cited 2015 Sep 11];93(23):13200–5. Available from: <http://www.pnas.org/content/93/23/13200>
71. Armstrong CM, Bezanilla F. Inactivation of the sodium channel. II. Gating current experiments. *J Gen Physiol* [Internet]. 1977 [cited 2015 Apr 24];70(5):567–590. Available from: <http://jgp.rupress.org/content/70/5/567.short>
72. Cha A, Ruben PC, George AL, Fujimoto E, Bezanilla F. Voltage sensors in domains III and IV, but not I and II, are immobilized by Na⁺ channel fast inactivation. *Neuron*. 1999 Jan;22(1):73–87.

73. Jones DK, Claydon TW, Ruben PC. Extracellular protons inhibit charge immobilization in the cardiac voltage-gated sodium channel. *Biophys J*. 2013 Jul 2;105(1):101–7.
74. Van Petegem F, Lobo PA, Ahern CA. Seeing the forest through the trees: towards a unified view on physiological calcium regulation of voltage-gated sodium channels. *Biophys J*. 2012 Dec 5;103(11):2243–51.
75. Abdelsayed M, Baruteau A-E, Gibbs K, Sanatani S, Krahn AD, Probst V, et al. Differential calcium sensitivity in NaV 1.5 mixed syndrome mutants. *J Physiol*. 2017 Sep 15;595(18):6165–86.
76. Potet F, Beckermann TM, Kunic JD, George AL. Intracellular Calcium Attenuates Late Current Conducted by Mutant Human Cardiac Sodium Channels. *Circ Arrhythm Electrophysiol* [Internet]. 2015 Aug;8(4):933–41. Available from: <http://www.ncbi.nlm.nih.gov/pmc/articles/PMC4545406/>
77. Wingo TL, Shah VN, Anderson ME, Lybrand TP, Chazin WJ, Balse JR. An EF-hand in the sodium channel couples intracellular calcium to cardiac excitability. *Nat Struct Mol Biol* [Internet]. 2004 Mar [cited 2015 Apr 25];11(3):219–25. Available from: <http://www.nature.com/nsmb/journal/v11/n3/full/nsmb737.html>
78. Wang C, Chung BC, Yan H, Wang H-G, Lee S-Y, Pitt GS. Structural analyses of Ca²⁺/CaM interaction with NaV channel C-termini reveal mechanisms of calcium-dependent regulation. *Nat Commun* [Internet]. 2014 Sep 18 [cited 2015 Apr 26];5. Available from: <http://www.nature.com/ncomms/2014/140918/ncomms5896/abs/ncomms5896.html>
79. Yan H, Wang C, Marx SO, Pitt GS. Calmodulin limits pathogenic Na⁺ channel persistent current. *J Gen Physiol* [Internet]. 2017 Feb 1 [cited 2017 Sep 18];149(2):277–93. Available from: <http://jgp.rupress.org/content/149/2/277>
80. Babitch JA, Anthony FA. Grasping for calcium binding sites in sodium channels with an EF hand. *J Theor Biol*. 1987 Aug 21;127(4):451–9.
81. Mori M, Konno T, Ozawa T, Murata M, Imoto K, Nagayama K. Novel interaction of the voltage-dependent sodium channel (VDSC) with calmodulin: does VDSC acquire calmodulin-mediated Ca²⁺-sensitivity? *Biochemistry (Mosc)*. 2000 Feb 15;39(6):1316–23.
82. Gabelli SB, Boto A, Kuhns VH, Bianchet MA, Farinelli F, Aripirala S, et al. Regulation of the NaV1.5 cytoplasmic domain by calmodulin. *Nat Commun*. 2014;5:5126.

83. Motoike HK, Liu H, Glaaser IW, Yang A-S, Tateyama M, Kass RS. The Na⁺ Channel Inactivation Gate Is a Molecular Complex. *J Gen Physiol* [Internet]. 2004 Feb;123(2):155–65. Available from: <https://www.ncbi.nlm.nih.gov/pmc/articles/PMC2217430/>
84. Shah VN, Wingo TL, Weiss KL, Williams CK, Balsler JR, Chazin WJ. Calcium-dependent regulation of the voltage-gated sodium channel hH1: intrinsic and extrinsic sensors use a common molecular switch. *Proc Natl Acad Sci U S A*. 2006 Mar 7;103(10):3592–7.
85. Schauf CL, Pencek TL, Davis FA. Slow sodium inactivation in *Myxicola* axons. Evidence for a second inactive state. *Biophys J* [Internet]. 1976 Jul 1 [cited 2016 Aug 31];16(7):771–8. Available from: <http://www.sciencedirect.com/science/article/pii/S000634957685727X>
86. Richmond JE, Featherstone DE, Hartmann HA, Ruben PC. Slow inactivation in human cardiac sodium channels. *Biophys J* [Internet]. 1998 [cited 2015 Apr 24];74(6):2945–2952. Available from: <http://www.sciencedirect.com/science/article/pii/S0006349598780014>
87. Xiong W, Farukhi YZ, Tian Y, DiSilvestre D, Li RA, Tomaselli GF. A conserved ring of charge in mammalian Na⁺ channels: a molecular regulator of the outer pore conformation during slow inactivation. *J Physiol* [Internet]. 2006 Nov 1;576(Pt 3):739–54. Available from: <http://www.ncbi.nlm.nih.gov/pmc/articles/PMC1890405/>
88. Silva JR, Goldstein SAN. Voltage-sensor movements describe slow inactivation of voltage-gated sodium channels I: wild-type skeletal muscle Na(V)1.4. *J Gen Physiol*. 2013 Mar;141(3):309–21.
89. Silva JR, Goldstein SAN. Voltage-sensor movements describe slow inactivation of voltage-gated sodium channels II: a periodic paralysis mutation in Na(V)1.4 (L689I). *J Gen Physiol*. 2013 Mar;141(3):323–34.
90. Vilin YY, Makita N, George AL, Ruben PC. Structural determinants of slow inactivation in human cardiac and skeletal muscle sodium channels. *Biophys J* [Internet]. 1999 [cited 2015 Apr 24];77(3):1384–1393. Available from: <http://www.sciencedirect.com/science/article/pii/S0006349599769870>
91. Villalba-Galea CA, Sandtner W, Starace DM, Bezanilla F. S4-based voltage sensors have three major conformations. *Proc Natl Acad Sci* [Internet]. 2008 [cited 2015 Apr 24];105(46):17600–17607. Available from: <http://www.pnas.org/content/105/46/17600.short>

92. Labro AJ, Lacroix JJ, Villalba-Galea CA, Snyders DJ, Bezanilla F. Molecular mechanism for depolarization-induced modulation of Kv channel closure. *J Gen Physiol* [Internet]. 2012 Nov 1 [cited 2015 Apr 25];140(5):481–93. Available from: <http://jgp.rupress.org/content/140/5/481>
93. Featherstone DE, Richmond JE, Ruben PC. Interaction between fast and slow inactivation in Skm1 sodium channels. *Biophys J*. 1996 Dec;71(6):3098–109.
94. Richmond JE, Featherstone DE, Hartmann HA, Ruben PC. Slow inactivation in human cardiac sodium channels. *Biophys J*. 1998 Jun;74(6):2945–52.
95. Capes DL, Arcisio-Miranda M, Jarecki BW, French RJ, Chanda B. Gating transitions in the selectivity filter region of a sodium channel are coupled to the domain IV voltage sensor. *Proc Natl Acad Sci* [Internet]. 2012 Feb 14 [cited 2015 Apr 24];109(7):2648–53. Available from: <http://www.pnas.org/cgi/doi/10.1073/pnas.1115575109>
96. Isom LL, De Jongh KS, Patton DE, Reber BF, Offord J, Charbonneau H, et al. Primary structure and functional expression of the beta 1 subunit of the rat brain sodium channel. *Science*. 1992 May 8;256(5058):839–42.
97. Yarbrough TL, Lu T, Lee H-C, Shibata EF. Localization of Cardiac Sodium Channels in Caveolin-Rich Membrane Domains: Regulation of Sodium Current Amplitude. *Circ Res* [Internet]. 2002 Mar 8 [cited 2017 Sep 30];90(4):443–9. Available from: <http://circres.ahajournals.org/content/90/4/443>
98. Vatta M, Ackerman MJ, Ye B, Makielski JC, Ughanze EE, Taylor EW, et al. Mutant caveolin-3 induces persistent late sodium current and is associated with long-QT syndrome. *Circulation*. 2006 Nov 14;114(20):2104–12.
99. Goldfarb M, Schoorlemmer J, Williams A, Diwakar S, Wang Q, Huang X, et al. Fibroblast Growth Factor Homologous Factors Control Neuronal Excitability through Modulation of Voltage-Gated Sodium Channels. *Neuron* [Internet]. 2007 Aug 2 [cited 2017 Oct 19];55(3):449–63. Available from: [http://www.cell.com/neuron/abstract/S0896-6273\(07\)00525-9](http://www.cell.com/neuron/abstract/S0896-6273(07)00525-9)
100. Ben-Johny M, Yang PS, Niu J, Yang W, Joshi-Mukherjee R, Yue DT. Conservation of Ca²⁺/Calmodulin Regulation across Na and Ca²⁺ channels. *Cell* [Internet]. 2014 Jun 19 [cited 2017 Mar 17];157(7):1657–70. Available from: <http://www.ncbi.nlm.nih.gov/pmc/articles/PMC4349408/>
101. Goldfarb M. Voltage-gated sodium channel-associated proteins and alternative mechanisms of inactivation and block. *Cell Mol Life Sci CMLS*. 2012 Apr;69(7):1067–76.

102. Calhoun JD, Isom LL. The role of non-pore-forming β subunits in physiology and pathophysiology of voltage-gated sodium channels. *Handb Exp Pharmacol*. 2014;221:51–89.
103. Das S, Gilchrist J, Bosmans F, Petegem FV. Binary architecture of the Nav1.2- β 2 signaling complex. *eLife* [Internet]. 2016 Feb 19 [cited 2017 Sep 29];5:e10960. Available from: <https://elifesciences.org/articles/10960>
104. Ko S-H, Lenkowski PW, Lee HC, Mounsey JP, Patel MK. Modulation of Nav1.5 by β 1- and β 3-subunit co-expression in mammalian cells. *Pflüg Arch* [Internet]. 2005 Jan 1 [cited 2017 Sep 29];449(4):403–12. Available from: <https://link.springer.com/article/10.1007/s00424-004-1348-4>
105. Zhu W, Voelker TL, Varga Z, Schubert AR, Nerbonne JM, Silva JR. Mechanisms of noncovalent β subunit regulation of NaV channel gating. *J Gen Physiol* [Internet]. 2017 Jul 18 [cited 2017 Sep 29];jgp.201711802. Available from: <http://jgp.rupress.org/content/early/2017/07/17/jgp.201711802>
106. Lopez-Santiago LF, Meadows LS, Ernst SJ, Chen C, Malhotra JD, McEwen DP, et al. Sodium channel Scn1b null mice exhibit prolonged QT and RR intervals. *J Mol Cell Cardiol*. 2007 Nov;43(5):636–47.
107. Liu C, Dib-Hajj SD, Renganathan M, Cummins TR, Waxman SG. Modulation of the cardiac sodium channel Nav1.5 by fibroblast growth factor homologous factor 1B. *J Biol Chem*. 2003 Jan 10;278(2):1029–36.
108. Wang H, Yang Z, Zhang Y, Yang J, Liu Y, Li C. Beta-receptor activation increases sodium current in guinea pig heart. *Acta Pharmacol Sin* [Internet]. 2009 Aug;30(8):1115–22. Available from: <https://www.ncbi.nlm.nih.gov/pmc/articles/PMC4217312/>
109. Kirstein M, Eickhorn R, Langenfeld H, Kochsiek K, Antoni H. Influence of beta-adrenergic stimulation on the fast sodium current in the intact rat papillary muscle. *Basic Res Cardiol*. 1991 Oct;86(5):441–8.
110. Matsuda JJ, Lee H, Shibata EF. Enhancement of rabbit cardiac sodium channels by beta-adrenergic stimulation. *Circ Res*. 1992 Jan;70(1):199–207.
111. Zhou J, Yi J, Hu N, George AL, Murray KT. Activation of Protein Kinase A Modulates Trafficking of the Human Cardiac Sodium Channel in *Xenopus* Oocytes. *Circ Res* [Internet]. 2000 Jul 7 [cited 2017 Nov 2];87(1):33–8. Available from: <http://circres.ahajournals.org/content/87/1/33>
112. Ono K, Fozzard HA, Hanck DA. Mechanism of cAMP-dependent modulation of cardiac sodium channel current kinetics. *Circ Res*. 1993 Apr;72(4):807–15.

113. Frohnwieser B, Chen LQ, Schreibmayer W, Kallen RG. Modulation of the human cardiac sodium channel alpha-subunit by cAMP-dependent protein kinase and the responsible sequence domain. *J Physiol* [Internet]. 1997 Jan 15;498(Pt 2):309–18. Available from: <https://www.ncbi.nlm.nih.gov/pmc/articles/PMC1159202/>
114. Riuró H, Campuzano O, Arbelo E, Iglesias A, Batlle M, Pérez-Villa F, et al. A missense mutation in the sodium channel β 1b subunit reveals SCN1B as a susceptibility gene underlying long QT syndrome. *Heart Rhythm* [Internet]. 2014 Jul [cited 2017 Nov 2];11(7):1202–9. Available from: <http://europemc.org/abstract/med/24662403>
115. Watanabe H, Darbar D, Kaiser DW, Jiramongkolchai K, Chopra S, Donahue BS, et al. Mutations in Sodium Channel Beta1 and Beta2 Subunits Associated with Atrial Fibrillation. *Circ Arrhythm Electrophysiol* [Internet]. 2009 Jun;2(3):268–75. Available from: <https://www.ncbi.nlm.nih.gov/pmc/articles/PMC2727725/>
116. Valdivia CR, Medeiros-Domingo A, Ye B, Shen W-K, Algiers TJ, Ackerman MJ, et al. Loss-of-function mutation of the SCN3B-encoded sodium channel β 3 subunit associated with a case of idiopathic ventricular fibrillation. *Cardiovasc Res* [Internet]. 2010 Jun 1;86(3):392–400. Available from: <https://www.ncbi.nlm.nih.gov/pmc/articles/PMC2868175/>
117. Medeiros-Domingo A, Kaku T, Tester DJ, Iturralde-Torres P, Itty A, Ye B, et al. SCN4B-encoded sodium channel beta4 subunit in congenital long-QT syndrome. *Circulation*. 2007 Jul 10;116(2):134–42.
118. Watanabe H, Koopmann TT, Le Scouarnec S, Yang T, Ingram CR, Schott J-J, et al. Sodium channel β 1 subunit mutations associated with Brugada syndrome and cardiac conduction disease in humans. *J Clin Invest*. 2008 Jun;118(6):2260–8.
119. Catterall WA. Sodium Channel Mutations and Epilepsy. In: Noebels JL, Avoli M, Rogawski MA, Olsen RW, Delgado-Escueta AV, editors. *Jasper's Basic Mechanisms of the Epilepsies* [Internet]. 4th ed. Bethesda (MD): National Center for Biotechnology Information (US); 2012. Available from: <http://www.ncbi.nlm.nih.gov/books/NBK98185/>
120. Estacion M, Gasser A, Dib-Hajj SD, Waxman SG. A sodium channel mutation linked to epilepsy increases ramp and persistent current of Nav1.3 and induces hyperexcitability in hippocampal neurons. *Exp Neurol*. 2010 Aug;224(2):362–8.
121. Vanoye CG, Gurnett CA, Holland KD, George AL, Kearney JA. Novel SCN3A variants associated with focal epilepsy in children. *Neurobiol Dis*. 2014 Feb;62:313–22.

122. Patel RR, Barbosa C, Brustovetsky T, Brustovetsky N, Cummins TR. Aberrant epilepsy-associated mutant Nav1.6 sodium channel activity can be targeted with cannabidiol. *Brain J Neurol*. 2016 Aug;139(Pt 8):2164–81.
123. Wallace RH, Wang DW, Singh R, Scheffer IE, George AL, Phillips HA, et al. Febrile seizures and generalized epilepsy associated with a mutation in the Na⁺-channel beta1 subunit gene SCN1B. *Nat Genet*. 1998 Aug;19(4):366–70.
124. Egri C, Vilin YY, Ruben PC. A thermoprotective role of the sodium channel β 1 subunit is lost with the β 1 (C121W) mutation. *Epilepsia*. 2012 Mar;53(3):494–505.
125. George AL. Inherited disorders of voltage-gated sodium channels. *J Clin Invest* [Internet]. 2005 Aug 1;115(8):1990–9. Available from: <https://www.ncbi.nlm.nih.gov/pmc/articles/PMC1180550/>
126. Chen Q, Kirsch GE, Zhang D, Brugada R, Brugada J, Brugada P, et al. Genetic basis and molecular mechanism for idiopathic ventricular fibrillation. *Nature* [Internet]. 1998 Mar 19 [cited 2015 Apr 24];392(6673):293–6. Available from: <http://www.nature.com/nature/journal/v392/n6673/full/392293a0.html>
127. Peters C, Rosch RE, Hughes E, Ruben PC. Temperature-dependent changes in neuronal dynamics in a patient with an *SCN1A* mutation and hyperthermia induced seizures. *Sci Rep* [Internet]. 2016 Sep 1 [cited 2017 Oct 31];6:srep31879. Available from: <https://www.nature.com/articles/srep31879>
128. Ghovanloo M-R, Abdelsayed M, Peters CH, Ruben PC. A Mixed Periodic Paralysis & Myotonia Mutant, P1158S, Imparts pH Sensitivity in Skeletal Muscle Voltage-gated Sodium Channels. *bioRxiv* [Internet]. 2017 Jul 17 [cited 2017 Jul 26];164988. Available from: <http://www.biorxiv.org/content/early/2017/07/17/164988>
129. Webb J, Cannon SC. Cold-induced defects of sodium channel gating in atypical periodic paralysis plus myotonia. *Neurology*. 2008 Mar 4;70(10):755–61.
130. Bezzina C, Veldkamp MW, Berg MP van den, Postma AV, Rook MB, Viersma J-W, et al. A Single Na⁺ Channel Mutation Causing Both Long-QT and Brugada Syndromes. *Circ Res* [Internet]. 1999 Dec 3 [cited 2017 Sep 27];85(12):1206–13. Available from: <http://circres.ahajournals.org/content/85/12/1206>
131. Priori SG, Napolitano C, Schwartz PJ, Bloise R, Crotti L, Ronchetti E. The elusive link between LQT3 and Brugada syndrome: the role of flecainide challenge. *Circulation*. 2000 Aug 29;102(9):945–7.
132. Zareba W, Sattari MN, Rosero S, Couderc JP, Moss AJ. Altered atrial, atrioventricular, and ventricular conduction in patients with the long QT syndrome caused by the Δ KPQ SCN5A sodium channel gene mutation. *Am J*

- Cardiol [Internet]. 2001 Dec 1 [cited 2017 Sep 27];88(11):1311–4. Available from: [http://www.ajconline.org/article/S0002-9149\(01\)02097-5/abstract](http://www.ajconline.org/article/S0002-9149(01)02097-5/abstract)
133. Wei J, Wang DW, Alings M, Fish F, Wathen M, Roden DM, et al. Congenital Long-QT Syndrome Caused by a Novel Mutation in a Conserved Acidic Domain of the Cardiac Na⁺ Channel. *Circulation* [Internet]. 1999 Jun 22 [cited 2015 Apr 25];99(24):3165–71. Available from: <http://circ.ahajournals.org/content/99/24/3165>
 134. Makita N, Behr E, Shimizu W, Horie M, Sunami A, Crotti L, et al. The E1784K mutation in SCN5A is associated with mixed clinical phenotype of type 3 long QT syndrome. *J Clin Invest*. 2008 Jun;118(6):2219–29.
 135. Remme CA, Verkerk AO, Nuyens D, Ginneken ACG van, Brunschot S van, Belterman CNW, et al. Overlap Syndrome of Cardiac Sodium Channel Disease in Mice Carrying the Equivalent Mutation of Human SCN5A-1795insD. *Circulation* [Internet]. 2006 Dec 12 [cited 2015 Nov 19];114(24):2584–94. Available from: <http://circ.ahajournals.org/content/114/24/2584>
 136. Takahashi K, Shimizu W, Miyake A, Nabeshima T, Nakayashiro M, Ganaha H. High prevalence of the SCN5A E1784K mutation in school children with long QT syndrome living on the Okinawa islands. *Circ J Off J Jpn Circ Soc*. 2014;78(8):1974–9.
 137. Grant AO, Carboni MP, Neplioueva V, Starmer CF, Memmi M, Napolitano C, et al. Long QT syndrome, Brugada syndrome, and conduction system disease are linked to a single sodium channel mutation. *J Clin Invest* [Internet]. 2002 Oct 15;110(8):1201–9. Available from: <http://www.ncbi.nlm.nih.gov/pmc/articles/PMC150793/>
 138. Chen T, Inoue M, Sheets MF. Reduced voltage dependence of inactivation in the SCN5A sodium channel mutation delF1617. *Am J Physiol - Heart Circ Physiol* [Internet]. 2005 Jun 1 [cited 2017 Sep 27];288(6):H2666–76. Available from: <http://ajpheart.physiology.org/content/288/6/H2666>
 139. Kanters JK, Yuan L, Hedley PL, Stoevring B, Jons C, Thomsen PEB, et al. Flecainide Provocation Reveals Concealed Brugada Syndrome in a Long QT Syndrome Family With a Novel L1786Q Mutation in SCN5A. *Circ J*. 2014;78(5):1136–43.
 140. Splawski I, Shen J, Timothy KW, Lehmann MH, Priori S, Robinson JL, et al. Spectrum of Mutations in Long-QT Syndrome Genes: KVLQT1, HERG, SCN5A, KCNE1, and KCNE2. *Circulation* [Internet]. 2000 Sep 5 [cited 2017 Sep 27];102(10):1178–85. Available from: <http://circ.ahajournals.org/content/102/10/1178>

141. Liang P, Liu W, Hu D, Li C, Tao W, Li L. [Novel SCN5A gene mutations associated with Brugada syndrome: V95I, A1649V and delF1617]. *Zhonghua Xin Xue Guan Bing Za Zhi*. 2006 Jul;34(7):616–9.
142. Gui J, Wang T, Jones RPO, Trump D, Zimmer T, Lei M. Multiple Loss-of-Function Mechanisms Contribute to SCN5A-Related Familial Sick Sinus Syndrome. *PLoS ONE* [Internet]. 2010 Jun 7;5(6). Available from: <http://www.ncbi.nlm.nih.gov/pmc/articles/PMC2881866/>
143. Chandra R, Starmer CF, Grant AO. Multiple effects of KPQ deletion mutation on gating of human cardiac Na⁺ channels expressed in mammalian cells. *Am J Physiol - Heart Circ Physiol* [Internet]. 1998 May 1 [cited 2017 Sep 27];274(5):H1643–54. Available from: <http://ajpheart.physiology.org/content/274/5/H1643>
144. Ghovanloo M-R, Abdelsayed M, Ruben PC. Effects of Amiodarone and N-desethylamiodarone on Cardiac Voltage-Gated Sodium Channels. *Front Pharmacol* [Internet]. 2016 [cited 2017 Nov 2];7. Available from: <https://www.frontiersin.org/articles/10.3389/fphar.2016.00039/full>
145. Veldkamp MW, Viswanathan PC, Bezzina C, Baartscheer A, Wilde AA, Balsler JR. Two distinct congenital arrhythmias evoked by a multidysfunctional Na⁽⁺⁾ channel. *Circ Res*. 2000 May 12;86(9):E91-97.
146. Deschênes I, Baroudi G, Berthet M, Barde I, Chalvidan T, Denjoy I, et al. Electrophysiological characterization of SCN5A mutations causing long QT (E1784K) and Brugada (R1512W and R1432G) syndromes. *Cardiovasc Res* [Internet]. 2000 Apr 1 [cited 2015 Apr 25];46(1):55–65. Available from: <http://cardiovascres.oxfordjournals.org/content/46/1/55>
147. Reed GJ, Boczek NJ, Etheridge SP, Ackerman MJ. CALM3 mutation associated with long QT syndrome. *Heart Rhythm* [Internet]. 2015 Feb 1 [cited 2015 Nov 3];12(2):419–22. Available from: <http://www.heartrhythmjournal.com/article/S1547527114012521/abstract>
148. Altmann HM, Tester DJ, Will ML, Middha S, Evans JM, Eckloff BW, et al. Homozygous/Compound Heterozygous Triadin Mutations Associated with Autosomal Recessive Long QT Syndrome and Pediatric Sudden Cardiac Arrest: Elucidation of Triadin Knockout Syndrome. *Circulation* [Internet]. 2015 Apr 28 [cited 2015 Nov 3];CIRCULATIONAHA.115.015397. Available from: <http://circ.ahajournals.org/content/early/2015/04/28/CIRCULATIONAHA.115.015397>
149. Nakano Y, Shimizu W. Genetics of long-QT syndrome. *J Hum Genet* [Internet]. 2015 Jun 25 [cited 2015 Nov 3]; Available from: <http://www.nature.com/jhg/journal/vaop/ncurrent/full/jhg201574a.html>

150. Napolitano C, Priori SG, Schwartz PJ, Bloise R, Ronchetti E, Nastoli J, et al. Genetic testing in the long QT syndrome: development and validation of an efficient approach to genotyping in clinical practice. *JAMA*. 2005 Dec 21;294(23):2975–80.
151. Jervell A, Lange-Nielsen F. Congenital deaf-mutism, functional heart disease with prolongation of the Q-T interval and sudden death. *Am Heart J*. 1957 Jul;54(1):59–68.
152. MEISSNER FL. Taubstummheit, und Taubstummenbildung. Beobachtungen und Erfahrungen, nebst einer Geschichte der Leipziger Taubstummen-Anstalt, etc. 1856. 410 p.
153. Tranebjærg L, Samson RA, Green GE. Jervell and Lange-Nielsen Syndrome. In: Pagon RA, Adam MP, Ardinger HH, Wallace SE, Amemiya A, Bean LJ, et al., editors. GeneReviews(®) [Internet]. Seattle (WA): University of Washington, Seattle; 1993 [cited 2015 Sep 11]. Available from: <http://www.ncbi.nlm.nih.gov/books/NBK1405/>
154. Romano C, Gemme G, Pongiglione R. [RARE CARDIAC ARRHYTHMIAS OF THE PEDIATRIC AGE. II. SYNCOPAL ATTACKS DUE TO PAROXYSMAL VENTRICULAR FIBRILLATION. (PRESENTATION OF 1ST CASE IN ITALIAN PEDIATRIC LITERATURE)]. *Clin Pediatr (Bologna)*. 1963 Sep;45:656–83.
155. Ward OC. A NEW FAMILIAL CARDIAC SYNDROME IN CHILDREN. *J Ir Med Assoc*. 1964 Apr;54:103–6.
156. Wang Q, Curran ME, Splawski I, Burn TC, Millholland JM, VanRaay TJ, et al. Positional cloning of a novel potassium channel gene: KVLQT1 mutations cause cardiac arrhythmias. *Nat Genet*. 1996 Jan;12(1):17–23.
157. Curran ME, Splawski I, Timothy KW, Vincent GM, Green ED, Keating MT. A molecular basis for cardiac arrhythmia: HERG mutations cause long QT syndrome. *Cell*. 1995 Mar 10;80(5):795–803.
158. Roden DM, Viswanathan PC. Genetics of acquired long QT syndrome. *J Clin Invest* [Internet]. 2005 Aug 1;115(8):2025–32. Available from: <https://www.ncbi.nlm.nih.gov/pmc/articles/PMC1180553/>
159. Shimizu W, Antzelevitch C. Cellular basis for long QT, transmural dispersion of repolarization, and torsade de pointes in the long QT syndrome. *J Electrocardiol*. 1999;32 Suppl:177–84.
160. Wehrens XHT, Abriel H, Cabo C, Benhorin J, Kass RS. Arrhythmogenic Mechanism of an LQT-3 Mutation of the Human Heart Na⁺ Channel α -Subunit : A Computational Analysis. *Circulation* [Internet]. 2000 Aug 1 [cited 2017 Oct 5];102(5):584–90. Available from: <http://circ.ahajournals.org/content/102/5/584>

161. Undrovinas NA, Maltsev VA, Belardinelli L, Sabbah HN, Undrovinas A. Late Sodium Current Contributes to Diastolic Cell Ca²⁺ Accumulation in Chronic Heart Failure. *J Physiol Sci JPS* [Internet]. 2010 Jul;60(4):245–57. Available from: <https://www.ncbi.nlm.nih.gov/pmc/articles/PMC2891122/>
162. Schwartz PJ, Priori SG, Locati EH, Napolitano C, Cantù F, Towbin JA, et al. Long QT Syndrome Patients With Mutations of the SCN5A and HERG Genes Have Differential Responses to Na⁺ Channel Blockade and to Increases in Heart Rate : Implications for Gene-Specific Therapy. *Circulation* [Internet]. 1995 Dec 15 [cited 2017 Nov 2];92(12):3381–6. Available from: <http://circ.ahajournals.org/content/92/12/3381>
163. Schwartz PJ, Priori SG, Spazzolini C, Moss AJ, Vincent GM, Napolitano C, et al. Genotype-Phenotype Correlation in the Long-QT Syndrome Gene-Specific Triggers for Life-Threatening Arrhythmias. *Circulation* [Internet]. 2001 Jan 2 [cited 2015 Aug 18];103(1):89–95. Available from: <http://circ.ahajournals.org/content/103/1/89>
164. Clancy CE, Tateyama M, Kass RS. Insights into the molecular mechanisms of bradycardia-triggered arrhythmias in long QT-3 syndrome. *J Clin Invest* [Internet]. 2002 Nov 1 [cited 2017 Nov 2];110(9):1251–62. Available from: <https://www-jci-org.proxy.lib.sfu.ca/articles/view/15928>
165. Baartscheer A, Schumacher CA, Belterman CNW, Coronel R, Fiolet JWT. SR calcium handling and calcium after-transients in a rabbit model of heart failure. *Cardiovasc Res* [Internet]. 2003 Apr 1 [cited 2017 Nov 2];58(1):99–108. Available from: <https://academic.oup.com/cardiovascres/article/58/1/99/295816>
166. Schwartz PJ. The congenital long QT syndromes from genotype to phenotype: clinical implications. *J Intern Med* [Internet]. 2006 Jan 1;259(1):39–47. Available from: <http://onlinelibrary.wiley.com/doi/10.1111/j.1365-2796.2005.01583.x/abstract>
167. Ruan Y, Liu N, Bloise R, Napolitano C, Priori SG. Gating properties of SCN5A mutations and the response to mexiletine in long-QT syndrome type 3 patients. *Circulation*. 2007 Sep 4;116(10):1137–44.
168. Brugada P, Brugada J. Right bundle branch block, persistent ST segment elevation and sudden cardiac death: A distinct clinical and electrocardiographic syndrome: A multicenter report. *J Am Coll Cardiol* [Internet]. 1992 Nov 15 [cited 2015 Apr 24];20(6):1391–6. Available from: <http://www.sciencedirect.com/science/article/pii/073510979290253J>
169. Antzelevitch C, Brugada P, Borggrefe M, Brugada J, Brugada R, Corrado D, et al. Brugada Syndrome: Report of the Second Consensus Conference Endorsed by the

- Heart Rhythm Society and the European Heart Rhythm Association. *Circulation* [Internet]. 2005 Feb 8 [cited 2015 Apr 24];111(5):659–70. Available from: <http://circ.ahajournals.org/content/111/5/659>
170. Meregalli PG, Wilde AAM, Tan HL. Pathophysiological mechanisms of Brugada syndrome: Depolarization disorder, repolarization disorder, or more? *Cardiovasc Res* [Internet]. 2005 Aug 15 [cited 2015 Sep 11];67(3):367–78. Available from: <http://cardiovascres.oxfordjournals.org/content/67/3/367>
171. Wilde AAM, Postema PG, Di Diego JM, Viskin S, Morita H, Fish JM, et al. The pathophysiological mechanism underlying Brugada syndrome. *J Mol Cell Cardiol* [Internet]. 2010 Oct 1 [cited 2015 Nov 19];49(4):543–53. Available from: <http://www.jmmc-online.com/article/S0022282810002762/abstract>
172. Mizusawa Y, Wilde AAM. Brugada Syndrome. *Circ Arrhythm Electrophysiol* [Internet]. 2012 Jun 1 [cited 2015 Nov 19];5(3):606–16. Available from: <http://circep.ahajournals.org/content/5/3/606>
173. Yan GX, Antzelevitch C. Cellular basis for the Brugada syndrome and other mechanisms of arrhythmogenesis associated with ST-segment elevation. *Circulation*. 1999 Oct 12;100(15):1660–6.
174. Antzelevitch C. Brugada syndrome. *Pacing Clin Electrophysiol PACE*. 2006 Oct;29(10):1130–59.
175. Coronel R, Casini S, Koopmann TT, Wilms-Schopman FJG, Verkerk AO, de Groot JR, et al. Right ventricular fibrosis and conduction delay in a patient with clinical signs of Brugada syndrome: a combined electrophysiological, genetic, histopathologic, and computational study. *Circulation*. 2005 Nov 1;112(18):2769–77.
176. Probst V, Wilde AAM, Barc J, Sacher F, Babuty D, Mabo P, et al. SCN5A Mutations and the Role of Genetic Background in the Pathophysiology of Brugada Syndrome. *Circ Cardiovasc Genet* [Internet]. 2009 Dec 1 [cited 2015 Nov 19];2(6):552–7. Available from: <http://circgenetics.ahajournals.org/content/2/6/552>
177. Juang J-MJ, Horie M. Genetics of Brugada syndrome. *J Arrhythmia* [Internet]. 2016 Oct 1;32(5):418–25. Available from: <http://www.sciencedirect.com/science/article/pii/S1880427616301004>
178. Veltmann C, Barajas-Martinez H, Wolpert C, Borggrefe M, Schimpf R, Pfeiffer R, et al. Further Insights in the Most Common SCN5A Mutation Causing Overlapping Phenotype of Long QT Syndrome, Brugada Syndrome, and Conduction Defect. *J Am Heart Assoc* [Internet]. 2016 Jul 1 [cited 2017 Feb 21];5(7):e003379. Available from: <http://jaha.ahajournals.org/content/5/7/e003379>

179. Papadatos GA, Wallerstein PMR, Head CEG, Ratcliff R, Brady PA, Benndorf K, et al. Slowed conduction and ventricular tachycardia after targeted disruption of the cardiac sodium channel gene *Scn5a*. *Proc Natl Acad Sci U S A* [Internet]. 2002 Apr 30 [cited 2015 Nov 19];99(9):6210–5. Available from: <http://www.ncbi.nlm.nih.gov/pmc/articles/PMC122928/>
180. Martin CA, Zhang Y, Grace AA, Huang CL-H. Increased Right Ventricular Repolarization Gradients Promote Arrhythmogenesis in a Murine Model of Brugada Syndrome. *J Cardiovasc Electrophysiol* [Internet]. 2010 Oct [cited 2015 Apr 25];21(10):1153–9. Available from: <http://www.ncbi.nlm.nih.gov/pmc/articles/PMC3084998/>
181. Royer A, Veen TAB van, Bouter SL, Marionneau C, Griol-Charhbil V, Léoni A-L, et al. Mouse Model of SCN5A-Linked Hereditary Lenègre’s Disease Age-Related Conduction Slowing and Myocardial Fibrosis. *Circulation* [Internet]. 2005 Apr 12 [cited 2015 Nov 19];111(14):1738–46. Available from: <http://circ.ahajournals.org/content/111/14/1738>
182. Veen TAB van, Stein M, Royer A, Quang KL, Charpentier F, Colledge WH, et al. Impaired Impulse Propagation in *Scn5a*-Knockout Mice Combined Contribution of Excitability, Connexin Expression, and Tissue Architecture in Relation to Aging. *Circulation* [Internet]. 2005 Sep 27 [cited 2015 Nov 19];112(13):1927–35. Available from: <http://circ.ahajournals.org/content/112/13/1927>
183. van Hoorn F, Campian ME, Spijkerboer A, Blom MT, Planken RN, van Rossum AC, et al. SCN5A Mutations in Brugada Syndrome Are Associated with Increased Cardiac Dimensions and Reduced Contractility. *PLoS ONE* [Internet]. 2012 Aug 2 [cited 2015 Nov 20];7(8):e42037. Available from: <http://dx.doi.org/10.1371/journal.pone.0042037>
184. Shy D, Gillet L, Abriel H. Cardiac sodium channel NaV1.5 distribution in myocytes via interacting proteins: the multiple pool model. *Biochim Biophys Acta*. 2013 Apr;1833(4):886–94.
185. Park DS, Cerrone M, Morley G, Vasquez C, Fowler S, Liu N, et al. Genetically engineered SCN5A mutant pig hearts exhibit conduction defects and arrhythmias. *J Clin Invest*. 2015 Jan;125(1):403–12.
186. Banasiak KJ, Burenkova O, Haddad GG. Activation of voltage-sensitive sodium channels during oxygen deprivation leads to apoptotic neuronal death. *Neuroscience*. 2004;126(1):31–44.
187. Dravet C. The core Dravet syndrome phenotype. *Epilepsia* [Internet]. 2011 Apr 1;52:3–9. Available from: <http://onlinelibrary.wiley.com/doi/10.1111/j.1528-1167.2011.02994.x/abstract>

188. Dumaine R, Towbin JA, Brugada P, Vatta M, Nesterenko DV, Nesterenko VV, et al. Ionic mechanisms responsible for the electrocardiographic phenotype of the Brugada syndrome are temperature dependent. *Circ Res*. 1999 Oct 29;85(9):803–9.
189. Mok N-S, Priori SG, Napolitano C, Chan N-Y, Chahine M, Baroudi G. A newly characterized SCN5A mutation underlying Brugada syndrome unmasked by hyperthermia. *J Cardiovasc Electrophysiol*. 2003 Apr;14(4):407–11.
190. Sugiura Y, Aoki T, Sugiyama Y, Hida C, Ogata M, Yamamoto T. Temperature-sensitive sodium channelopathy with heat-induced myotonia and cold-induced paralysis. *Neurology [Internet]*. 2000 Jun 13 [cited 2017 Sep 28];54(11):2179–81. Available from: <http://www.neurology.org/content/54/11/2179>
191. Yeh Y-T, Tu C-M, Wu Y-W. Mesenteric Ischemia Mimicking ST-Segment Elevation Myocardial Infarction. *N Engl J Med [Internet]*. 2015 Aug 20;373(8):780–1. Available from: <http://dx.doi.org/10.1056/NEJMc1506103>
192. Kagiya Y, Hill JL, Gettes LS. Interaction of acidosis and increased extracellular potassium on action potential characteristics and conduction in guinea pig ventricular muscle. *Circ Res [Internet]*. 1982 Nov 1 [cited 2015 Aug 18];51(5):614–23. Available from: <http://circres.ahajournals.org/content/51/5/614>
193. Kenigsberg DN, Khanal S, Kowalski M, Krishnan SC. Prolongation of the QTc interval is seen uniformly during early transmural ischemia. *J Am Coll Cardiol*. 2007 Mar 27;49(12):1299–305.
194. Manning AS, Hearse DJ. Reperfusion-induced arrhythmias: mechanisms and prevention. *J Mol Cell Cardiol*. 1984 Jun;16(6):497–518.
195. McClelland VM, Bakalinova DB, Hendriksz C, Singh RP. Glutaric aciduria type 1 presenting with epilepsy. *Dev Med Child Neurol*. 2009 Mar;51(3):235–9.
196. Haberlandt E, Canestrini C, Brunner-Krainz M, Möslinger D, Mussner K, Plecko B, et al. Epilepsy in patients with propionic acidemia. *Neuropediatrics*. 2009 Jun;40(3):120–5.
197. Ma X, Zhang Y, Yang Y, Liu X, Yang Z, Bao X, et al. Epilepsy in children with methylmalonic acidemia: electroclinical features and prognosis. *Brain Dev*. 2011 Oct;33(9):790–5.
198. Baranchuk A, Nguyen T, Ryu MH, Femenía F, Zareba W, Wilde AAM, et al. Brugada Phenocopy: New Terminology and Proposed Classification. *Ann Noninvasive Electrocardiol [Internet]*. 2012 Oct 1 [cited 2015 Aug 20];17(4):299–314. Available from: <http://onlinelibrary.wiley.com/doi/10.1111/j.1542-474X.2012.00525.x/abstract>

199. Genaro NR, Anselm DD, Cervino N, Estevez AO, Perona C, Villamil AM, et al. Brugada phenocopy clinical reproducibility demonstrated by recurrent hypokalemia. *Ann Noninvasive Electrocardiol Off J Int Soc Holter Noninvasive Electrocardiol Inc.* 2014 Jul;19(4):387–90.
200. Ortega-Carnicer J, Bertos-Polo J, Gutiérrez-Tirado C. Aborted sudden death, transient Brugada pattern, and wide QRS dysrhythmias after massive cocaine ingestion. *J Electrocardiol.* 2001 Oct;34(4):345–9.
201. Littmann L, Monroe MH, Svenson RH. Brugada-type electrocardiographic pattern induced by cocaine. *Mayo Clin Proc.* 2000 Aug;75(8):845–9.
202. Anselm DD, Evans JM, Baranchuk A. Brugada phenocopy: A new electrocardiogram phenomenon. *World J Cardiol [Internet].* 2014 Mar 26 [cited 2015 Apr 26];6(3):81–6. Available from: <http://www.ncbi.nlm.nih.gov/pmc/articles/PMC3964189/>
203. Agrawal S, Stevens S, Shirani J, Garg J, Nanda S. Ischemia-induced Brugada phenocopy. *J Electrocardiol.* 2015 Oct;48(5):815–7.
204. Zhang N, Liu T, Tse G, Yu S, Fu H, Xu G, et al. Brugada phenocopy in a patient with acute pulmonary embolism presenting with recurrent syncope. *Oxf Med Case Rep [Internet].* 2017 May 1 [cited 2017 Nov 2];2017(5). Available from: <https://academic.oup.com/omcr/article/2017/5/omx014/3858726>
205. Amin AS, de Groot EAA, Ruijter JM, Wilde AAM, Tan HL. Exercise-induced ECG changes in Brugada syndrome. *Circ Arrhythm Electrophysiol.* 2009 Oct;2(5):531–9.
206. Cheng J, Tester DJ, Tan B-H, Valdivia CR, Kroboth S, Ye B, et al. The common African American polymorphism SCN5A-S1103Y interacts with mutation SCN5A-R680H to increase late Na current. *Physiol Genomics.* 2011 May 13;43(9):461–6.
207. Doetzer AD, Sotomaior VS, Bubna MH, Raskin S. What can be done when asymptomatic patients discover they have Brugada syndrome? A case report of Brugada syndrome. *Int J Cardiol.* 2011 Aug 4;150(3):e96–97.
208. García-Borbolla M, García-Borbolla R, Valenzuela LF, Trujillo F, García-Borbolla M, García-Borbolla R, et al. Ventricular Tachycardia Induced by Exercise Testing in a Patient With Brugada Syndrome. *Rev Esp Cardiol [Internet].* 2007 Jan 9 [cited 2015 Apr 26];60(9):993–4. Available from: <http://www.revespcardiol.org/en/ventricular-tachycardia-induced-by-exercise/articulo/13114120/>
209. Makimoto H, Nakagawa E, Takaki H, Yamada Y, Okamura H, Noda T, et al. Augmented ST-segment elevation during recovery from exercise predicts cardiac

- events in patients with Brugada syndrome. *J Am Coll Cardiol*. 2010 Nov 2;56(19):1576–84.
210. Skinner JR, Chung S-K, Montgomery D, McCulley CH, Crawford J, French J, et al. Near-miss SIDS due to Brugada syndrome. *Arch Dis Child* [Internet]. 2005 May 1 [cited 2015 Apr 26];90(5):528–9. Available from: <http://adc.bmj.com/content/90/5/528>
211. Vatta M, Dumaine R, Varghese G, Richard TA, Shimizu W, Aihara N, et al. Genetic and biophysical basis of sudden unexplained nocturnal death syndrome (SUNDS), a disease allelic to Brugada syndrome. *Hum Mol Genet*. 2002 Feb 1;11(3):337–45.
212. Hoffman RS. Treatment of patients with cocaine-induced arrhythmias: bringing the bench to the bedside. *Br J Clin Pharmacol* [Internet]. 2010 May [cited 2015 Sep 11];69(5):448–57. Available from: <http://www.ncbi.nlm.nih.gov/pmc/articles/PMC2856045/>
213. Masrur S, Memon S, Thompson PD. Brugada syndrome, exercise, and exercise testing. *Clin Cardiol*. 2015 May;38(5):323–6.
214. Dewar LJ, Alcaide M, Fornika D, D’Amato L, Shafaatalab S, Stevens CM, et al. Investigating the Genetic Causes of Sudden Unexpected Death in Children Through Targeted Next-Generation Sequencing Analysis CLINICAL PERSPECTIVE. *Circ Cardiovasc Genet* [Internet]. 2017 Aug 1 [cited 2017 Sep 28];10(4):e001738. Available from: <http://circgenetics.ahajournals.org/content/10/4/e001738>
215. Cobbe SM, Poole-Wilson PA. The time of onset and severity of acidosis in myocardial ischaemia. *J Mol Cell Cardiol*. 1980 Aug;12(8):745–60.
216. El Banani H, Bernard M, Baetz D, Cabanes E, Cozzone P, Lucien A, et al. Changes in intracellular sodium and pH during ischaemia-reperfusion are attenuated by trimetazidine. Comparison between low- and zero-flow ischaemia. *Cardiovasc Res*. 2000 Sep;47(4):688–96.
217. Kolocassides KG, Seymour AM, Galiñanes M, Hearse DJ. Paradoxical effect of ischemic preconditioning on ischemic contracture? NMR studies of energy metabolism and intracellular pH in the rat heart. *J Mol Cell Cardiol*. 1996 May;28(5):1045–57.
218. Allam S, Noble JS. Cocaine-excited delirium and severe acidosis. *Anaesthesia*. 2001 Apr;56(4):385–6.
219. Constantinou JE, Gillis J, Ouvrier RA, Rahilly PM. Hypoxic-ischaemic encephalopathy after near miss sudden infant death syndrome. *Arch Dis Child* [Internet]. 1989 May 1 [cited 2015 Aug 13];64(5):703–8. Available from: <http://adc.bmj.com/content/64/5/703>

220. Hick JL, Smith SW, Lynch MT. Metabolic acidosis in restraint-associated cardiac arrest: a case series. *Acad Emerg Med Off J Soc Acad Emerg Med*. 1999 Mar;6(3):239–43.
221. Sullivan MJ, Knight JD, Higginbotham MB, Cobb FR. Relation between central and peripheral hemodynamics during exercise in patients with chronic heart failure. Muscle blood flow is reduced with maintenance of arterial perfusion pressure. *Circulation [Internet]*. 1989 Oct 1 [cited 2015 Aug 13];80(4):769–81. Available from: <http://circ.ahajournals.org/content/80/4/769>
222. Fleet WF, Johnson TA, Graebner CA, Gettes LS. Effect of serial brief ischemic episodes on extracellular K⁺, pH, and activation in the pig. *Circulation [Internet]*. 1985 Oct 1 [cited 2015 Aug 13];72(4):922–32. Available from: <http://circ.ahajournals.org/cgi/doi/10.1161/01.CIR.72.4.922>
223. Ichihara K, Haga N, Abiko Y. Is ischemia-induced pH decrease of dog myocardium respiratory or metabolic acidosis? *Am J Physiol - Heart Circ Physiol [Internet]*. 1984 May 1 [cited 2015 Aug 13];246(5):H652–7. Available from: <http://ajpheart.physiology.org/content/246/5/H652>
224. Yan GX, Kléber AG. Changes in extracellular and intracellular pH in ischemic rabbit papillary muscle. *Circ Res*. 1992 Aug;71(2):460–70.
225. Poole-Wilson PA, Cameron IR. Intracellular pH and K⁺ of cardiac and skeletal muscle in acidosis and alkalosis. *Am J Physiol*. 1975 Nov;229(5):1305–10.
226. Adler S, Roy A, Relman AS. Intracellular Acid-Base Regulation. I. The Response of Muscle Cells to Changes in CO₂ Tension or Extracellular Bicarbonate Concentration *. *J Clin Invest [Internet]*. 1965 Jan [cited 2015 Nov 27];44(1):8–20. Available from: <http://www.ncbi.nlm.nih.gov/pmc/articles/PMC442014/>
227. Steenbergen C, Deleeuw G, Rich T, Williamson JR. Effects of acidosis and ischemia on contractility and intracellular pH of rat heart. *Circ Res*. 1977 Dec;41(6):849–58.
228. Fellenz MP, Gerweck LE. Influence of extracellular pH on intracellular pH and cell energy status: relationship to hyperthermic sensitivity. *Radiat Res*. 1988 Nov;116(2):305–12.
229. Butterworth J, Tennant MC. Postmortem Human Brain pH and Lactate in Sudden Infant Death Syndrome. *J Neurochem [Internet]*. 1989 Nov 1 [cited 2015 Aug 13];53(5):1494–9. Available from: <http://onlinelibrary.wiley.com/doi/10.1111/j.1471-4159.1989.tb08543.x/abstract>
230. Colan SD, Liberthson RR, Cahen L, Shannon DC, Kelly DH. Incidence and significance of primary abnormalities of cardiac rhythm in infants at high risk for sudden infant death syndrome. *Pediatr Cardiol*. 1984;5(4):267–71.

231. Kelly DH, Shannon DC. Periodic breathing in infants with near-miss sudden infant death syndrome. *Pediatrics*. 1979 Mar;63(3):355–60.
232. Southall DP. Role of apnea in the sudden infant death syndrome: a personal view. *Pediatrics*. 1988 Jan;81(1):73–84.
233. Tonkin S. Sudden Infant Death Syndrome: Hypothesis of Causation. *Pediatrics* [Internet]. 1975 May 1 [cited 2015 Apr 26];55(5):650–61. Available from: <http://pediatrics.aappublications.org/content/55/5/650>
234. Gebert G, Benzing H, Strohm M. Changes in the interstitial pH of dog myocardium in response to local ischemia, hypoxia, hyper- and hypocapnia, measured continuously by means of glass microelectrodes. *Pflüg Arch* [Internet]. 1971 [cited 2015 Aug 13];329(1):72–81. Available from: <http://link.springer.com/article/10.1007/BF00586901>
235. Jones DK, Peters CH, Tolhurst SA, Claydon TW, Ruben PC. Extracellular proton modulation of the cardiac voltage-gated sodium channel, Nav1.5. *Biophys J*. 2011 Nov 2;101(9):2147–56.
236. Zhang JF, Siegelbaum SA. Effects of external protons on single cardiac sodium channels from guinea pig ventricular myocytes. *J Gen Physiol*. 1991 Dec;98(6):1065–83.
237. Woodhull AM. Ionic blockage of sodium channels in nerve. *J Gen Physiol*. 1973 Jun;61(6):687–708.
238. Khan A, Romantseva L, Lam A, Lipkind G, Fozzard HA. Role of outer ring carboxylates of the rat skeletal muscle sodium channel pore in proton block. *J Physiol* [Internet]. 2002 Aug 15;543(Pt 1):71–84. Available from: <http://www.ncbi.nlm.nih.gov/pmc/articles/PMC2290475/>
239. Khan A, Kyle JW, Hanck DA, Lipkind GM, Fozzard HA. Isoform-dependent interaction of voltage-gated sodium channels with protons. *J Physiol*. 2006 Oct 15;576(Pt 2):493–501.
240. Jones DK, Peters CH, Allard CR, Claydon TW, Ruben PC. Proton sensors in the pore domain of the cardiac voltage-gated sodium channel. *J Biol Chem*. 2013 Feb 15;288(7):4782–91.
241. Shi YP, Cheng YM, Van Slyke AC, Claydon TW. External protons destabilize the activated voltage sensor in hERG channels. *Eur Biophys J EBJ*. 2014 Mar;43(2–3):59–69.

242. King JH, Huang CL-H, Fraser JA. Determinants of myocardial conduction velocity: implications for arrhythmogenesis. *Front Physiol* [Internet]. 2013 Jun 28;4. Available from: <http://www.ncbi.nlm.nih.gov/pmc/articles/PMC3695374/>
243. Abdelsayed M, Peters CH, Ruben PC. Differential thermosensitivity in mixed syndrome cardiac sodium channel mutants. *J Physiol*. 2015 Jul 1;
244. Vassilev P, Scheuer T, Catterall WA. Inhibition of inactivation of single sodium channels by a site-directed antibody. *Proc Natl Acad Sci* [Internet]. 1989 [cited 2015 Apr 25];86(20):8147–8151. Available from: <http://www.pnas.org/content/86/20/8147.short>
245. Schwartz PJ, Crotti L, Insolia R. Long-QT Syndrome From Genetics to Management. *Circ Arrhythm Electrophysiol* [Internet]. 2012 Aug 1 [cited 2016 Aug 30];5(4):868–77. Available from: <http://circep.ahajournals.org/content/5/4/868>
246. Vilin YY, Peters CH, Ruben PC. Acidosis differentially modulates inactivation in $na(v)1.2$, $na(v)1.4$, and $na(v)1.5$ channels. *Front Pharmacol*. 2012;3:109.
247. Taglialatela M, Toro L, Stefani E. Novel voltage clamp to record small, fast currents from ion channels expressed in *Xenopus* oocytes. *Biophys J*. 1992 Jan;61(1):78–82.
248. Stefani E, Bezanilla F. Cut-open oocyte voltage-clamp technique. *Methods Enzymol*. 1998;293:300–18.
249. Hu D, Veltmann C, Barajas-Martinez H, Pfeiffer R, Belardinelli L, Strupp G, et al. Abstract 19745: Brugada, Long QT and Cardiac Conduction Disease Overlap Syndrome Associated with the SCN5A-E1784K Mutation: Clinical Phenotype, Genetic Background and Potential Therapy. *Circulation* [Internet]. 2012 Nov 20 [cited 2015 Aug 13];126(21 Supplement):A19745. Available from: http://circ.ahajournals.org/cgi/content/meeting_abstract/126/21_MeetingAbstracts/A19745
250. Wijeyeratne YD, Muggenthaler M, Batchvarov V, Tanck M, Schott JJ, Kyndt F, et al. 16 Ethnicity and phenotype in the SCN5A E1784K mutation. *Europace* [Internet]. 2014 Oct 1 [cited 2015 Aug 13];16(suppl 3):iii7-iii7. Available from: http://europace.oxfordjournals.org/content/16/suppl_3/iii7.1
251. Zheng Z-J, Croft JB, Giles WH, Mensah GA. Sudden Cardiac Death in the United States, 1989 to 1998. *Circulation* [Internet]. 2001 Oct 30 [cited 2016 Aug 30];104(18):2158–63. Available from: <http://circ.ahajournals.org/content/104/18/2158>

252. Hermansen L, Osnes JB. Blood and muscle pH after maximal exercise in man. *J Appl Physiol* [Internet]. 1972 Mar 1 [cited 2015 Aug 13];32(3):304–8. Available from: <http://jap.physiology.org/content/32/3/304>
253. Osnes JB, Hermansen L. Acid-base balance after maximal exercise of short duration. *J Appl Physiol* [Internet]. 1972 Jan 1 [cited 2015 Aug 13];32(1):59–63. Available from: <http://jap.physiology.org/content/32/1/59>
254. Keynes RD, Elinder F. The screw-helical voltage gating of ion channels. *Proc R Soc B Biol Sci* [Internet]. 1999 Apr 22 [cited 2016 Sep 11];266(1421):843–52. Available from: <http://www.ncbi.nlm.nih.gov/pmc/articles/PMC1689903/>
255. Fink M, Noble D. Markov models for ion channels: versatility versus identifiability and speed. *Philos Trans R Soc Lond Math Phys Eng Sci* [Internet]. 2009 Jun 13 [cited 2017 Oct 17];367(1896):2161–79. Available from: <http://rsta.royalsocietypublishing.org/content/367/1896/2161>
256. Clancy CE, Rudy Y. Na(+) channel mutation that causes both Brugada and long-QT syndrome phenotypes: a simulation study of mechanism. *Circulation*. 2002 Mar 12;105(10):1208–13.
257. Sheets MF, Hanck DA. Molecular Action of Lidocaine on the Voltage Sensors of Sodium Channels. *J Gen Physiol* [Internet]. 2003 Feb [cited 2016 Sep 9];121(2):163–75. Available from: <http://www.ncbi.nlm.nih.gov/pmc/articles/PMC2217326/>
258. Ruben PC, Starkus JG, Rayner MD. Holding potential affects the apparent voltage-sensitivity of sodium channel activation in crayfish giant axons. *Biophys J* [Internet]. 1990 [cited 2015 Apr 24];58(5):1169. Available from: <http://www.ncbi.nlm.nih.gov/pmc/articles/PMC1281062/>
259. Armstrong CM. Na channel inactivation from open and closed states. *Proc Natl Acad Sci* [Internet]. 2006 [cited 2015 Apr 24];103(47):17991–17996. Available from: <http://www.pnas.org/content/103/47/17991.short>
260. Wang S, Liu S, Morales MJ, Strauss HC, Rasmusson RL. A quantitative analysis of the activation and inactivation kinetics of HERG expressed in *Xenopus* oocytes. *J Physiol*. 1997 Jul 1;502 (Pt 1):45–60.
261. Gurkiewicz M, Korngreen A. A Numerical Approach to Ion Channel Modelling Using Whole-Cell Voltage-Clamp Recordings and a Genetic Algorithm. *PLoS Comput Biol* [Internet]. 2007 Aug 31 [cited 2015 Apr 24];3(8):e169. Available from: <http://dx.plos.org/10.1371/journal.pcbi.0030169>
262. Rudokas MW, Varga Z, Schubert AR, Asaro AB, Silva JR. The *Xenopus* Oocyte Cut-open Vaseline Gap Voltage-clamp Technique With Fluorometry. *JoVE J Vis Exp*

- [Internet]. 2014 Mar 11 [cited 2017 Apr 4];(85):e51040–e51040. Available from: <https://www.jove.com/video/51040/the-xenopus-oocyte-cut-open-vaseline-gap-voltage-clamp-technique-with>
263. Chanda B. Coupling Interactions between Voltage Sensors of the Sodium Channel as Revealed by Site-specific Measurements. *J Gen Physiol* [Internet]. 2004 Feb 23 [cited 2015 Apr 24];123(3):217–30. Available from: <http://www.jgp.org/cgi/doi/10.1085/jgp.200308971>
264. ten Tusscher KHWJ, Noble D, Noble PJ, Panfilov AV. A model for human ventricular tissue. *Am J Physiol Heart Circ Physiol*. 2004 Apr;286(4):H1573–1589.
265. Tan PS, Perry MD, Ng CA, Vandenberg JI, Hill AP. Voltage-sensing domain mode shift is coupled to the activation gate by the N-terminal tail of hERG channels. *J Gen Physiol* [Internet]. 2012 Sep [cited 2015 Apr 9];140(3):293–306. Available from: <http://www.ncbi.nlm.nih.gov/pmc/articles/PMC3434099/>
266. Hilber K, Sandtner W, Kudlacek O, Glaaser IW, Weisz E, Kyle JW, et al. The Selectivity Filter of the Voltage-gated Sodium Channel Is Involved in Channel Activation. *J Biol Chem* [Internet]. 2001 Jul 27 [cited 2016 Sep 9];276(30):27831–9. Available from: <http://www.jbc.org/content/276/30/27831>
267. Sheets MF, Kyle JW, Hanck DA. The role of the putative inactivation lid in sodium channel gating current immobilization. *J Gen Physiol*. 2000 May;115(5):609–20.
268. Bezzina C, Veldkamp MW, van Den Berg MP, Postma AV, Rook MB, Viersma JW, et al. A single Na(+) channel mutation causing both long-QT and Brugada syndromes. *Circ Res*. 1999 Dec 3;85(12):1206–13.
269. Ruan Y, Liu N, Napolitano C, Priori SG. Therapeutic Strategies for Long-QT Syndrome Does the Molecular Substrate Matter? *Circ Arrhythm Electrophysiol* [Internet]. 2008 Oct 1 [cited 2016 Sep 9];1(4):290–7. Available from: <http://circep.ahajournals.org/content/1/4/290>
270. Baroudi G, Chahine M. Biophysical phenotypes of SCN5A mutations causing long QT and Brugada syndromes. *FEBS Lett* [Internet]. 2000 Dec 29;487(2):224–8. Available from: <http://www.sciencedirect.com/science/article/pii/S0014579300023607>
271. Gallivan JP, Dougherty DA. Cation- π interactions in structural biology. *Proc Natl Acad Sci* [Internet]. 1999 Aug 17 [cited 2017 Nov 2];96(17):9459–64. Available from: <http://www.pnas.org/content/96/17/9459>
272. Brandl M, Weiss MS, Jabs A, Sühnel J, Hilgenfeld R. C-h \cdots π -interactions in proteins. *J Mol Biol* [Internet]. 2001 Mar 16;307(1):357–77. Available from: <http://www.sciencedirect.com/science/article/pii/S0022283600944735>

273. Schwans JP, Sunden F, Lassila JK, Gonzalez A, Tsai Y, Herschlag D. Use of anion–aromatic interactions to position the general base in the ketosteroid isomerase active site. *Proc Natl Acad Sci* [Internet]. 2013 Jul 9 [cited 2017 Nov 2];110(28):11308–13. Available from: <http://www.pnas.org.proxy.lib.sfu.ca/content/110/28/11308>
274. Zondlo NJ. Aromatic–Proline Interactions: Electronically Tunable CH/ π Interactions. *Acc Chem Res* [Internet]. 2013 Apr 16;46(4):1039–49. Available from: <http://dx.doi.org/10.1021/ar300087y>
275. Patton DE, West JW, Catterall WA, Goldin AL. Amino acid residues required for fast Na (+)-channel inactivation: charge neutralizations and deletions in the III-IV linker. *Proc Natl Acad Sci* [Internet]. 1992 [cited 2015 Apr 25];89(22):10905–10909. Available from: <http://www.pnas.org/content/89/22/10905.short>
276. Sali A, Blundell TL. Comparative protein modelling by satisfaction of spatial restraints. *J Mol Biol*. 1993 Dec 5;234(3):779–815.
277. Bordoli L, Kiefer F, Arnold K, Benkert P, Battey J, Schwede T. Protein structure homology modeling using SWISS-MODEL workspace. *Nat Protoc* [Internet]. 2008 Dec [cited 2017 Nov 1];4(1):1–13. Available from: <http://www.nature.com/nprot/journal/v4/n1/abs/nprot.2008.197.html>
278. Arnold K, Bordoli L, Kopp J, Schwede T. The SWISS-MODEL workspace: a web-based environment for protein structure homology modelling. *Bioinformatics* [Internet]. 2006 Jan 15 [cited 2017 Nov 1];22(2):195–201. Available from: <https://academic.oup.com/bioinformatics/article/22/2/195/423760>
279. Biasini M, Bienert S, Waterhouse A, Arnold K, Studer G, Schmidt T, et al. SWISS-MODEL: modelling protein tertiary and quaternary structure using evolutionary information. *Nucleic Acids Res* [Internet]. 2014 Jul 1 [cited 2017 Nov 1];42(W1):W252–8. Available from: <https://academic.oup.com/nar/article/42/W1/W252/2435313>
280. Zumhagen S, Veldkamp MW, Stallmeyer B, Baartscheer A, Eckardt L, Paul M, et al. A Heterozygous Deletion Mutation in the Cardiac Sodium Channel Gene SCN5A with Loss- and Gain-of-Function Characteristics Manifests as Isolated Conduction Disease, without Signs of Brugada or Long QT Syndrome. *PLOS ONE* [Internet]. 2013 Jun 28 [cited 2017 Oct 5];8(6):e67963. Available from: <http://journals.plos.org/plosone/article?id=10.1371/journal.pone.0067963>
281. Shen H, Zhou Q, Pan X, Li Z, Wu J, Yan N. Structure of a eukaryotic voltage-gated sodium channel at near-atomic resolution. *Science* [Internet]. 2017 Feb 9 [cited 2017 Mar 22];eaal4326. Available from: <http://science.sciencemag.org/content/early/2017/02/08/science.aal4326>

282. Frustaci A, Priori SG, Pieroni M, Chimenti C, Napolitano C, Rivolta I, et al. Cardiac histological substrate in patients with clinical phenotype of Brugada syndrome. *Circulation*. 2005 Dec 13;112(24):3680–7.
283. Kapplinger JD, Tester DJ, Salisbury BA, Carr JL, Harris-Kerr C, Pollevick GD, et al. Spectrum and prevalence of mutations from the first 2,500 consecutive unrelated patients referred for the FAMILION® long QT syndrome genetic test. *Heart Rhythm* [Internet]. 2009 Sep 1;6(9):1297–303. Available from: <http://www.sciencedirect.com/science/article/pii/S1547527109005682>
284. Smits JPP, Eckardt L, Probst V, Bezzina CR, Schott JJ, Remme CA, et al. Genotype-phenotype relationship in Brugada syndrome: electrocardiographic features differentiate SCN5A-related patients from non-SCN5A-related patients. *J Am Coll Cardiol* [Internet]. 2002 Jul 17;40(2):350–6. Available from: <http://www.sciencedirect.com/science/article/pii/S0735109702019629>
285. Priori SG, Napolitano C, Gasparini M, Pappone C, Bella PD, Giordano U, et al. Natural History of Brugada Syndrome: Insights for Risk Stratification and Management. *Circulation* [Internet]. 2002 Mar 19 [cited 2017 Nov 2];105(11):1342–7. Available from: <http://circ.ahajournals.org/content/105/11/1342>
286. Li Q, Huang H, Liu G, Lam K, Rutberg J, Green MS, et al. Gain-of-function mutation of Nav1.5 in atrial fibrillation enhances cellular excitability and lowers the threshold for action potential firing. *Biochem Biophys Res Commun*. 2009 Feb 27;380(1):132–7.
287. Keller DI, Acharfi S, Delacrétaz E, Benammar N, Rotter M, Pfammatter J-P, et al. A novel mutation in SCN5A, delQKP 1507–1509, causing long QT syndrome:: Role of Q1507 residue in sodium channel inactivation. *J Mol Cell Cardiol* [Internet]. 2003 Dec 1;35(12):1513–21. Available from: <http://www.sciencedirect.com/science/article/pii/S0022282803003043>
288. Bennett PB, Yazawa K, Makita N, George AL. Molecular mechanism for an inherited cardiac arrhythmia. *Nature*. 1995 Aug 24;376(6542):683–5.
289. Chahine M, Plante E, Kallen RG. Sea Anemone Toxin (ATX II) Modulation of Heart and Skeletal Muscle Sodium Channel α -Subunits Expressed in tsA201 Cells. *J Membr Biol* [Internet]. 1996 Jul 1 [cited 2017 Oct 3];152(1):39–48. Available from: <https://link-springer-com.proxy.lib.sfu.ca/article/10.1007/s002329900083>
290. Studenik CR, Zhou Z, January CT. Differences in action potential and early afterdepolarization properties in LQT2 and LQT3 models of long QT syndrome. *Br J Pharmacol* [Internet]. 2001 Jan 1;132(1):85–92. Available from:

<http://onlinelibrary.wiley.com.proxy.lib.sfu.ca/doi/10.1038/sj.bjp.0703770/abstract>

291. Abriel H. Cardiac sodium channel Nav1.5 and interacting proteins: Physiology and pathophysiology. *J Mol Cell Cardiol* [Internet]. 2010 Jan 1;48(1):2–11. Available from: <http://www.sciencedirect.com/science/article/pii/S0022282809003678>
292. Antzelevitch C, Fish JM. Therapy for the Brugada syndrome. *Handb Exp Pharmacol* [Internet]. 2006 [cited 2017 Nov 2];(171):305–30. Available from: <http://europepmc.org/abstract/med/16610350>
293. Brugada J, Brugada R, Brugada P. Pharmacological and device approach to therapy of inherited cardiac diseases associated with cardiac arrhythmias and sudden death. *J Electrocardiol* [Internet]. 2000 Jan 1;33(Supplement 1):41–7. Available from: <http://www.sciencedirect.com/science/article/pii/S0022073600800059>
294. Wang Y, Mi J, Lu K, Lu Y, Wang K. Comparison of Gating Properties and Use-Dependent Block of Nav1.5 and Nav1.7 Channels by Anti-Arrhythmics Mexiletine and Lidocaine. *PLoS ONE* [Internet]. 2015 Jun 11;10(6). Available from: <https://www.ncbi.nlm.nih.gov/pmc/articles/PMC4465899/>
295. Shimizu W, Antzelevitch C, Suyama K, Kurita T, Taguchi A, Aihara N, et al. Effect of Sodium Channel Blockers on ST Segment, QRS Duration, and Corrected QT Interval in Patients with Brugada Syndrome. *J Cardiovasc Electrophysiol* [Internet]. 2000 Dec 1;11(12):1320–9. Available from: <http://onlinelibrary.wiley.com.proxy.lib.sfu.ca/doi/10.1046/j.1540-8167.2000.01320.x/abstract>
296. Valdivia CR, Tester DJ, Rok BA, Porter CJ, Munger TM, Jahangir A, et al. A trafficking defective, Brugada syndrome-causing SCN5A mutation rescued by drugs. *Cardiovasc Res* [Internet]. 2004 Apr 1 [cited 2017 Nov 2];62(1):53–62. Available from: <https://academic.oup.com/circres/article/62/1/53/372406>
297. Moreau A, Keller DI, Huang H, Fressart V, Schmied C, Timour Q, et al. Mexiletine Differentially Restores the Trafficking Defects Caused by Two Brugada Syndrome Mutations. *Front Pharmacol* [Internet]. 2012 [cited 2017 Nov 2];3. Available from: <https://www.frontiersin.org/articles/10.3389/fphar.2012.00062/full>
298. Ruan Y, Denegri M, Liu N, Bachetti T, Seregni M, Morotti S, et al. Trafficking defects and gating abnormalities of a novel SCN5A mutation question gene-specific therapy in long QT syndrome type 3. *Circ Res*. 2010 Apr 30;106(8):1374–83.

Appendix A. Data for Chapter 2

Table A.1. Voltage-dependence of Channel Conductance and Fast Inactivation

	G $V_{1/2}$ (mV)	G z	FI $V_{1/2}$ (mV)	FI z
CF, pH 7.4	-35.2±1.0	4.14±0.23	-75.4±1.05	-4.10±0.34
CF, pH 7.0	-33.5±1.1	4.12±0.20	-73.3±0.7	-4.45±0.25
CF, pH 6.0	-29.7±1.1	3.60±0.23	-70.4±0.6	-4.38±0.21
CF/EK, pH 7.4	-27.8±1.5	2.94±0.08	-80.4±0.6	-4.16±0.31
CF/EK, pH 7.0	-26.0±1.3	3.21±0.10	-77.8±0.8	-4.31±0.28
CF/EK, pH 6.0	-19.3±1.3	2.47±0.24	-75.1±1.1	-3.89±0.31

Where values are mean ± standard error of the mean

Where N = 8 for CF and CF/EK GVs and N = 5 and N = 6 for CF and CF/EK FI, respectively

G $V_{1/2}$: Midpoint of the conductance-voltage relationship

G z: Apparent valence of the conductance-voltage relationship

FI $V_{1/2}$: Midpoint of the steady-state fast inactivation relationship

FI z: Apparent valence of the steady-state fast inactivation relationship

Table A.2. Fast Inactivation Recovery and Closed-State Onset Time Constants

	τ_{Frec} -130 mv (ms)	τ_{Frec} -110 mv (ms)	τ_{Frec} -90 mv (ms)	τ_{Frec} -70 mv (ms)	τ_{FI} -70 mv (ms)	τ_{FI} -50 mv (ms)
CF, pH 7.4	2.98±0.17	7.52±0.70	21.6±2.7	81.5±4.4	69.2±6.4	26.5±5.6
CF, pH 7.0	3.08±0.15	7.54±0.69	20.7±1.6	79.9±4.9	72.8±7.3	25.9±6.1
CF, pH 6.0	2.77±0.32	6.15±0.48	17.4±2.5	65.2±4.7	75.2±9.2	50.6±4.8
CF/EK, pH 7.4	1.69±0.08	3.61±0.17	8.7±0.4	21.1±2.6	14.9±1.6	6.8±1.1
CF/EK, pH 7.0	1.69±0.04	3.76±0.16	9.0±0.4	22.0±1.8	16.3±1.4	6.9±1.0
CF/EK, pH 6.0	1.59±0.09	3.36±0.22	7.9±0.4	23.7±2.7	17.0±1.6	9.3±1.1

Where values are mean ± standard error of the mean

N = 6 for all cases

τ_{Frec} : Time constant of recovery from fast inactivation at a given voltage

τ_{FI} : Time constant of closed-state fast inactivation at a given voltage

Table A.3. Open State Fast Inactivation Time Constants

	τ_{FI} -30 mV (ms)	τ_{FI} -20 mV (ms)	τ_{FI} -10 mV (ms)	τ_{FI} 0 mV (ms)	τ_{FI} 10 mV (ms)	τ_{FI} 20 mV (ms)	τ_{FI} 30 mV (ms)
CF, pH 7.4	1.66±0.0 7	1.24±0.0 9	1.03±0.0 7	0.89±0.0 7	0.85±0.0 8	0.83±0.0 9	0.89±0.0 9
CF, pH 7.0	2.03±0.1 1	1.36±0.0 5	1.12±0.0 7	0.92±0.0 7	0.86±0.0 9	0.88±0.0 9	0.94±0.1 1
CF, pH 6.0	2.30±0.1 2	1.69±0.0 6	1.25±0.0 6	1.03±0.0 8	0.94±0.1 0	0.98±0.1 1	1.00±0.1 4
CF/EK, pH 7.4	1.12±0.0 9	0.90±0.0 6	0.79±0.0 4	0.70±0.0 4	0.64±0.0 4	0.63±0.0 4	0.63±0.0 5
CF/EK, pH 7.0	1.26±0.0 8	1.02±0.0 6	0.87±0.0 4	0.75±0.0 4	0.68±0.0 3	0.70±0.0 4	0.70±0.0 5
CF/EK, pH 6.0	1.47±0.0 9	1.22±0.0 6	1.07±0.0 6	0.94±0.0 5	0.86±0.0 7	0.81±0.0 7	0.80±0.0 8

Where values are mean \pm standard error of the mean

Where N = 7 or 8 for all cases

τ_{FI} : Time constant of open-state fast inactivation at a given voltage

Table A.4. Persistent Sodium Current

	$I_{\text{Nap}} -30 \text{ mV} (\%)$	$I_{\text{Nap}} 20 \text{ mV} (\%)$	$I_{\text{Nap}} -10 \text{ mV} (\%)$	$I_{\text{Nap}} 0 \text{ mV} (\%)$
CF, pH 7.4	0.36 ± 0.02	0.44 ± 0.04	0.40 ± 0.02	0.28 ± 0.03
CF, pH 7.0	0.44 ± 0.03	0.49 ± 0.04	0.50 ± 0.06	0.39 ± 0.09
CF, pH 6.0	0.37 ± 0.05	0.43 ± 0.05	0.42 ± 0.07	0.28 ± 0.12
CF/EK, pH 7.4	4.13 ± 0.43	4.02 ± 0.53	3.67 ± 0.53	3.12 ± 0.48
CF/EK, pH 7.0	4.75 ± 0.51	4.50 ± 0.57	4.03 ± 0.60	3.25 ± 0.66
CF/EK, pH 6.0	6.36 ± 0.67	6.53 ± 0.60	5.88 ± 0.65	4.85 ± 0.75

Where values are mean \pm standard error of the mean

Where N = 6 for CF and N = 8 for EK

I_{Nap} : Persistent sodium current measured as the fraction of current remaining at the end of a 100 ms depolarization to a given membrane potential.

Table A.5. Slow Inactivation Recovery Time Constants

	CF pH 7.4 (s)	CF pH 7.0 (s)	CF pH 6.0 (s)	CF/EK pH 7.4 (s)	CF/EK pH 7.0 (s)	CF/EK pH 6.0 (s)
-120 mV τ_f	0.037±0.00 9	0.042±0.01 0	0.090±0.02 7	0.060±0.00 7	0.057±0.00 7	0.046±0.01 2
-120 mV τ_s	1.55±0.37	1.80±0.20	1.27±0.11	0.681±0.05 7	0.630±0.06 2	0.361±0.06 7
-90 mV τ_f	0.336±0.07 4	0.301±0.02 8	0.699±0.44 1 ^a	0.360±0.05 0	0.324±0.06 7	0.282±0.06 2
-90 mV τ_s	5.31±0.77	6.99±0.86	6.29±1.06	2.51±0.43	3.08±1.03	1.32±0.33
-80 mV τ_f	0.276±0.02 3	0.285±0.01 3	0.250±0.01 3	0.413±0.03 4	0.434±0.02 8	0.551±0.13 1
-80 mV τ_s	4.97±0.44	7.11±0.98	5.76±0.515	3.71±0.17	4.78±0.48	4.21±0.86

All values are represented as mean ± standard error

^a The mean represented contains a single outlier which did not alter the conclusion from the statistical test, with this point removed the mean and standard error is 0.258 ± 0.032

CF: -120 mV, N = 5; -90 mV, N = 4; -80 mV, N = 5

CF/EK: -120 mV, N = 6; -90 mV, N = 5; -80 mV, N = 5

τ_f : Time constant of the fast component of slow inactivation recovery at a given membrane potential

τ_s : Time constant of the slow component of slow inactivation recovery at a given membrane potential

Table A.6. Slow Inactivation Onset Time Constants

	CF pH 7.4 (s)	CF pH 7.0 (s)	CF pH 6.0 (s)	CF/EK pH 7.4 (s)	CF/EK pH 7.0 (s)	CF/EK pH 6.0 (s)
-30 mV τ_f	1.33±0.39	1.61±0.31	1.98±0.55	1.02±0.31	1.56±0.44	1.80±0.48
-30 mV τ_s	10.4±1.24	11.4±1.07	15.4±2.44	6.74±1.14	11.6±2.09	16.2±3.79
0 mV τ_f	1.15±0.22	0.975±0.167	2.05±0.40	0.425±0.096	0.518±0.069	0.790±0.199
0 mV τ_s	9.96±0.63	11.2±1.78	14.5±1.73	5.32±0.74	6.84±0.67	10.7±1.60
30 mV τ_s a	6.14±0.28	8.35±0.37	10.5±0.69	5.48±0.55	5.03±0.22	8.10±1.17

All values are represented as mean ± standard error

^a At +30 mV only a single time constant of slow inactivation could be fit. This time constant corresponded in time scale to the slow components measured at -30 mV and 0 mV.

CF: -30 mV N = 4; 0 mV N = 5; 30 mV N = 5

CF/EK: -30 mV N = 5; 0 mV N = 5; 30 mV N = 6

τ_f : Time constant of the fast component of slow inactivation onset at a given membrane potential

τ_s : Time constant of the slow component of slow inactivation onset at a given membrane potential

Table A.7. Gating Charge Activation and Deactivation Voltage-Dependence

	$QV_{\text{On}} V_{1/2}$ (mV)	$QV_{\text{On}} z$	$QV_{\text{Deac}} V_{1/2}$ (mV)	$QV_{\text{Deac}} z$
CF, pH 7.4	-64.3±1.5	1.29±0.08	-84.9±1.1	1.73±0.07
CF, pH 6.0	-56.5±1.6	1.41±0.09	-77.4±1.6	1.69±0.06
CF/EK, pH 7.4	-75.6±1.6	1.44±0.07	-79.8±1.3	1.63±0.05
CF/EK, pH 6.0	-66.1±0.8	1.55±0.07	-69.8±1.1	1.69±0.06

Where values are mean ± standard error of the mean

Where N = 6 and N = 10 for CF and CF/EK On QVs, respectively

N = 6 and N = 8 for CF and CF/EK Off QVs, respectively

N = 6 and N = 6 for CF and CF/EK Deactivation, respectively

$QV_{\text{On}} V_{1/2}$: Midpoint of the charge-voltage relationship measured using outward gating currents

$QV_{\text{On}} z$: Apparent valence of the charge-voltage relationship measured using outward gating currents

$QV_{\text{Deac}} V_{1/2}$: Midpoint of the gating charge deactivation voltage-dependence curve

$QV_{\text{Deac}} z$: Apparent valence of the gating charge deactivation voltage-dependence curve

Table A.8. Gating Charge Deactivation Rates at -150mV

	τ_F (ms)	A_F	τ_S (ms)	A_S
CF, pH 7.4	0.583 ± 0.067	0.604 ± 0.048	3.724 ± 0.357	0.469 ± 0.044
CF, pH 6.0	0.538 ± 0.040	0.637 ± 0.053	4.183 ± 0.737	0.463 ± 0.052
CF/EK, pH 7.4	0.706 ± 0.064	0.807 ± 0.040	5.741 ± 0.793	0.266 ± 0.041
CF/EK, pH 6.0	0.738 ± 0.075	0.834 ± 0.031	4.516 ± 0.686	0.275 ± 0.053

All values are represented as mean \pm standard error

Where N = 9 for CF and N = 13 for CF/EK

τ_F : Time constant of the fast component of gating charge deactivation

τ_S : Time constant of the slow component of gating charge deactivation

A_F : Amplitude of the fast component of gating charge deactivation

A_S : Amplitude of the slow component of gating charge deactivation

Appendix B. Peters-Ruben Model Parameters

Table B.1. Transition Rates for the Peters-Ruben Model

	CF pH 7.4	CF/EK pH 7.4	CF pH 6.0	CF/EK pH 6.0
δ	2.2897	2.2897	1.922	1.922
λ	22.897	22.897	19.22	19.22
α_1	$381.14e^{V/9.657}$	$381.14e^{V/9.657}$	$371.54e^{V/7.813}$	$371.54e^{V/7.813}$
β_1	$0.3446e^{V/-78.1}$	$0.3446e^{V/-78.1}$	$0.104e^{V/-49.96}$	$0.104e^{V/-49.96}$
α_2	$381.14e^{V/9.657}$	$381.14e^{V/9.657}$	$371.54e^{V/7.813}$	$371.54e^{V/7.813}$
β_2	$0.3446e^{V/-78.1}$	$0.3446e^{V/-78.1}$	$0.104e^{V/-49.96}$	$0.104e^{V/-49.96}$
α_3	$183.94e^{V/22.4}$	$183.94e^{V/22.4}$	$134.71e^{V/10.73}$	$134.71e^{V/10.73}$
β_3	$0.3867e^{V/-38.76}$ $\times (DIII - DIVI)$	$0.3867e^{V/-38.76}$ $\times (DIII - DIVI)$	$0.1025e^{V/-30.29}$ $\times (DIII - DIVI)$	$0.1025e^{V/-30.29}$ $\times (DIII - DIVI)$
α_4	$91.93e^{V/8.417}$ $+ 48.39e^{V/11.51}$	$152e^{V/11.8}$ $+ 60.88e^{V/12.97}$	$237e^{V/7.207}$ $+ 4.99e^{V/16.01}$	$204.65e^{V/11.02}$ $+ 19.59e^{V/15.31}$
β_4	$9.273 \times 10^{-6}e^{V/-11.51}$	$3.904 \times 10^{-5}e^{V/-12.52}$	$1.432 \times 10^{-5}e^{V/-11.51}$	$1.144 \times 10^{-4}e^{V/-14}$
SI_1	9.39×10^{-5}	9.39×10^{-5}	4.278×10^{-5}	4.278×10^{-5}
SR_1	$3.874 \times 10^{-4} + 4.687$ $\times 10^{-6}e^{-V/15.06}$	$3.874 \times 10^{-4} + 4.687$ $\times 10^{-6}e^{-V/15.06}$	$3.597 \times 10^{-4} + 3.666$ $\times 10^{-6}e^{V/-14.32}$	$3.597 \times 10^{-4} + 3.666$ $\times 10^{-6}e^{V/-14.32}$
SI_2	9.39×10^{-5}	9.39×10^{-5}	4.278×10^{-5}	4.278×10^{-5}
SR_2	$3.874 \times 10^{-4} + 4.687$ $\times 10^{-6}e^{-V/15.06}$	$3.874 \times 10^{-4} + 4.687$ $\times 10^{-6}e^{-V/15.06}$	$3.597 \times 10^{-4} + 3.666$ $\times 10^{-6}e^{V/-14.32}$	$3.597 \times 10^{-4} + 3.666$ $\times 10^{-6}e^{V/-14.32}$
SI_3	3.971×10^{-5}	3.971×10^{-5}	2.716×10^{-5}	2.716×10^{-5}
SR_3	$5.199 \times 10^{-5} + 2.642$ $\times 10^{-6}e^{V/-22.47}$	$9.436 \times 10^{-5} + 2.396$ $\times 10^{-6}e^{V/-18.97}$	$3.852 \times 10^{-5} + 9.863$ $\times 10^{-7}e^{V/-17.85}$	$4.994 \times 10^{-5} + 6.335$ $\times 10^{-7}e^{V/-14.21}$
FI	1.522	2.50	1.178	1.71
FR	0.002	0.024	0.0015	0.023

V is membrane potential in mV and all rates are in ms⁻¹

Appendix C. Data for Chapter 3

Table C.1. Voltage-Dependence of Fluorescence for DIII and DIV VCF C373Y and C373Y/E1784K Channels

	F $V_{1/2}$ (mV)	F z
DIII VCF CY	-127.7 \pm 1.3	0.82 \pm 0.05
DIII VCF CY/EK	-135.3 \pm 2.0	1.22 \pm 0.09
DIV VCF CY	-56.8 \pm 6.6	1.91 \pm 0.32
DIV VCF CY/EK	-85.3 \pm 4.6	1.60 \pm 0.12

All values are represented as mean \pm standard error

Where N = 4 for all cases

F $V_{1/2}$: Midpoint of the fluorescence voltage relationship

F z: Apparent valence of the fluorescence voltage relationship

Table C.2. Voltage-Dependence of IFM/QQQ and IFM/QQQ-EK Conductance

	$G V_{1/2}$ (mV)	$G z$
IFM/QQQ, pH 7.4	-43.7 ± 1.4	4.10 ± 0.26
IFM/QQQ, pH 6.0	-36.8 ± 1.6	3.33 ± 0.24
IFM/QQQ-EK, pH 7.4	-44.6 ± 1.0	3.39 ± 0.22
IFM/QQQ -EK, pH 6.0	-37.8 ± 0.7	2.77 ± 0.13

Where values are mean \pm standard error of the mean and where N = 7 for IFM/QQQ and IFM/QQQ-EK

$G V_{1/2}$: Midpoint of the conductance-voltage relationship

$G z$: Apparent valence of the conductance-voltage relationship

Appendix D. Data for Chapter 4

Table D.1. Voltage-dependence of Channel Conductance

Mutant	G $V_{1/2}$ pH 7.4 (mV)	G $V_{1/2}$ pH 7.0 (mV)	G $V_{1/2}$ pH 6.0 (mV)	N
E1784A	-33.4±1.1	-32.3±1.2	-27.6±1.0	10
E1784D	-36.0±0.9	-34.9±1.1	-28.7±1.0	7
E1784E	-36.0±0.5	-35.2±0.8	-29.6±0.8	8
E1784K	-32.9±2.7	-30.9±3.1	-27.4±2.5	7
E1784Q	-34.5±0.6	-32.0±1.0	-28.1±1.2	9
E1784R	-30.7±1.5	-29.4±1.8	-25.7±1.7	9
E1784V	-27.1±1.4	-24.3±1.6	-20.0±0.7	5
E1784W	-37.8±2.3	-34.7±1.6	-31.1±3.0	5

Where values are mean ± standard error of the mean
G $V_{1/2}$: Midpoint of the conductance-voltage relationship

Table D.2. Voltage-dependence of Channel Fast Inactivation

Mutant	FI $V_{1/2}$ pH 7.4 (mV)	FI $V_{1/2}$ pH 7.0 (mV)	FI $V_{1/2}$ pH 6.0 (mV)	N
E1784A	-72.1±0.4	-70.1±0.4	-67.2±0.4	9
E1784D	-75.2±1.1	-73.7±0.9	-70.1±1.2	7
E1784E	-75.0±0.9	-74.2±0.8	-70.2±0.5	9
E1784K	-81.8±1.0	-79.6±1.2	-77.5±1.2	6
E1784Q	-77.6±0.3	-75.0±0.2	-71.1±0.5	8
E1784R	-80.7±1.0	-79.2±1.2	-76.4±1.2	9
E1784V	-77.4±0.5	-75.5±1.1	-72.2±0.5	5
E1784W	-67.6±1.2	-65.9±1.6	-62.6±1.4	5

Where values are mean ± standard error of the mean

FI $V_{1/2}$: Midpoint of the voltage-dependence of fast inactivation

Table D.3. Voltage-dependence of Gating Charge Activation

Mutant	Q V _{1/2} pH 7.4 (mV)	Q V _{1/2} pH 6.0 (mV)	N
E1784A	-57.1±3.7	-53.6±7.9	4
E1784D	-67.2±1.9	-56.8±1.6	6
E1784E	-62.4±5.0	-57.6±3.0	5
E1784K	-78.2±2.3	-65.5±0.7	6
E1784Q	-74.1±1.6	-73.8±5.7	4
E1784R	-72.6±3.4	-64.3±2.8	5
E1784V	-73.2±3.4	-66.8±1.5	5
E1784W	-56.2±2.2	-51.4±3.5	5

Where values are mean ± standard error of the mean

Q V_{1/2}: Midpoint of the gating charge activation-voltage relationship

Table D.4. Voltage-dependence of Gating Charge Deactivation

Mutant	Deac $V_{1/2}$ pH 7.4 (mV)	Deac $V_{1/2}$ pH 6.0 (mV)	N
E1784A	-85.4±1.5	-81.2±4.2	4
E1784D	-86.5±0.7	-79.6±1.5	5
E1784E	-85.5±1.1	-81.1±1.0	4
E1784K	-84.8±2.2	-75.6±1.3	5
E1784Q	-86.7±1.3	-80.0±2.8	4
E1784R	-79.8±2.2	-74.8±2.4	5
E1784V	-86.3±1.2	-76.3±0.8	5
E1784W	-81.5±1.5	-71.2±2.1	5

Where values are mean ± standard error of the mean

Deac $V_{1/2}$: Midpoint of the gating charge deactivation-voltage relationship

Table D.5. Normalized Non-Inactivating Current

Mutant	V _m	I _{Nap} pH 7.4 (%)	I _{Nap} pH 7.0 (%)	I _{Nap} pH 6.0 (%)	N
E1784A	-30 mV	0.57±0.17	0.62±0.21	0.74±0.57	5
	-20 mV	0.49±0.08	0.50±0.10	0.42±0.26	5
	-10 mV	0.42±0.06	0.29±0.09	0.18±0.13	5
	0 mV	0.19±0.08	0.12±0.06	0.07±0.07	5
E1784D	-30 mV	0.56±0.07	0.60±0.08	0.76±0.10	4
	-20 mV	0.55±0.10	0.55±0.08	0.52±0.10	4
	-10 mV	0.45±0.10	0.46±0.11	0.48±0.09	4
	0 mV	0.01±0.17	-0.04±0.24	0.26±0.04	4
E1784E	-30 mV	0.49±0.07	0.63±0.06	0.40±0.14	4
	-20 mV	0.52±0.06	0.66±0.06	0.55±0.06	4
	-10 mV	0.38±0.06	0.60±0.04	0.47±0.07	4
	0 mV	0.15±0.09	0.41±0.07	0.32±0.08	4
E1784K	-30 mV	3.06±0.18	3.32±0.20	5.06±0.44	4
	-20 mV	2.87±0.13	3.15±0.12	5.18±0.39	4
	-10 mV	2.53±0.20	2.85±0.19	4.46±0.27	4
	0 mV	1.96±0.32	2.38±0.26	3.71±0.24	4
E1784Q	-30 mV	0.37±0.28	0.20±0.13	0.91±0.91	4
	-20 mV	0.19±0.11	0.20±0.12	0.17±0.17	4
	-10 mV	0.00±0	0.00±0	0.00±0	4
	0 mV	0.00±0	0.00±0	0.00±0	4
E1784R	-30 mV	2.35±0.21	2.39±0.18	3.31±0.16	5
	-20 mV	1.68±0.08	1.87±0.12	2.82±0.08	5
	-10 mV	1.26±0.14	1.57±0.14	2.77±0.24	5
	0 mV	0.73±0.19	1.21±0.18	2.10±0.24	5
E1784V	-30 mV	0.32±0.03	0.39±0.04	0.50±0.05	5
	-20 mV	0.32±0.02	0.35±0.02	0.47±0.05	5
	-10 mV	0.17±0.05	0.27±0.03	0.33±0.04	5
	0 mV	-0.12±0.21	0.16±0.07	0.28±0.11	5
E1784W	-30 mV	0.26±0.03	0.25±0.04	0.25±0.07	5
	-20 mV	0.22±0.02	0.25±0.04	0.20±0.04	5
	-10 mV	0.14±0.04	0.06±0.14	0.18±0.04	5
	0 mV	-0.01±0.05	0.06±0.04	0.10±0.05	5

Where values are mean ± standard error of the mean

V_m: Membrane Potential

I_{Nap}: Persistent sodium current measured as the fraction of current remaining at the end of a 100 ms depolarization to a given membrane potential.

Table D.6. Time Constants of Fast Inactivation Recovery

Mutant	V _m	τ _{Frec} pH 7.4 (ms)	τ _{Frec} pH 7.0 (ms)	τ _{Frec} pH 6.0 (ms)	N
E1784A	-130 mV	3.1±0.2	3.0±0.2	2.7±0.1	5
	-110 mV	6.7±0.5	6.6±0.5	5.8±0.2	5
	-90 mV	17.5±1.8	20.5±2.2	13.8±0.6	5
	-70 mV	108.5±6.0	108.1±9.5	74.6±6.2	5
E1784D	-130 mV	3.6±0.1	3.6±0.1	3.4±0.2	4
	-110 mV	8.3±0.4	7.7±0.3	7.6±0.3	4
	-90 mV	25.1±1.3	23.0±1.7	18.1±0.7	4
	-70 mV	77.0±9.7	80.6±5.0	79.0±4.8	4
E1784E	-130 mV	3.6±0.2	3.7±0.2	3.4±0.1	5
	-110 mV	9.3±0.8	9.5±0.6	7.8±0.4	5
	-90 mV	30.5±3.3	30.4±2.2	21.2±1.9	5
	-70 mV	110.7±4.3	110.6±6.2	84.7±5.1	5
E1784K	-130 mV	2.2±0.2	2.2±0.1	2.0±0.2	3
	-110 mV	5.0±0.3	5.0±0.2	4.5±0.3	3
	-90 mV	13.2±1.1	12.9±0.5	11.1±0.8	3
	-70 mV	24.7±2.4	26.0±1.8	29.5±3.8	3
E1784Q	-130 mV	2.5±0.2	2.5±0.2	2.1±0.2	5
	-110 mV	5.7±0.4	6.3±0.6	4.7±0.5	5
	-90 mV	15.1±0.8	16.0±1.1	11.4±0.9	5
	-70 mV	65.8±7.1	57.1±4.6	41.5±5.5	5
E1784R	-130 mV	2.5±0.1	2.8±0.2	2.5±0.1	5
	-110 mV	5.7±0.1	6.2±0.3	5.4±0.3	5
	-90 mV	16.2±1.0	15.5±0.5	12.5±0.6	5
	-70 mV	36.9±1.9	37.6±4.8	31.7±1.1	5
E1784V	-130 mV	2.4±0.2	2.4±0.1	2.0±0.1	5
	-110 mV	5.8±0.3	6.0±0.3	4.7±0.4	5
	-90 mV	17.3±1.5	16.9±1.5	12.4±1.1	5
	-70 mV	45.6±1.6	48.1±3.1	36.8±1.7	5
E1784W	-130 mV	2.3±0.1	2.4±0.1	2.1±0.1	4
	-110 mV	5.6±0.2	5.6±0.1	4.7±0.2	4
	-90 mV	15.1±0.7	15.6±0.4	12.4±0.9	4
	-70 mV	94.6±1.5	94.2±2.2	68.4±3.1	4

Where values are mean ± standard error of the mean

V_m: Membrane Potential

τ_{Frec}: Time constant of recovery from fast inactivation at a given voltage

Table D.7. Time Constants of Closed-State Fast Inactivation

Mutant	V _m	τ _{FI} pH 7.4 (ms)	τ _{FI} pH 7.0 (ms)	τ _{FI} pH 6.0 (ms)	N
E1784A	-70 mV	108.9±14.5	119.7±10.0	160.8±29.2	5
	-50 mV	28.8±2.9	39.8±2.2	44.9±4.5	5
E1784D	-70 mV	100.9±7.8	106.6±7.2	146.0±20.2	4
	-50 mV	19.7±4.0	21.8±3.3	28.4±9.7	4
E1784E	-70 mV	75.1±6.3	92.9±8.1	143.0±8.1	5
	-50 mV	24.6±1.9	27.5±2.5	38.4±2.0	5
E1784K	-70 mV	14.1±1.9	17.1±2.7	20.6±4.9	3
	-50 mV	4.4±1.1	5.1±1.3	6.3±1.4	3
E1784Q	-70 mV	36.8±3.5	44.5±4.0	49.2±5.8	5
	-50 mV	11.9±0.9	14.8±1.2	18.8±2.1	5
E1784R	-70 mV	22.2±2.3	24.0±3.1	27.6±3.5	5
	-50 mV	6.8±0.8	7.3±0.9	9.7±1.5	5
E1784V	-70 mV	36.1±2.3	47.6±5.2	47.2±4.4	5
	-50 mV	9.3±1.1	12.9±2.4	15.7±1.8	5
E1784W	-70 mV	122.3±10.4	146.8±10.9	169.9±6.0	4
	-50 mV	47.2±17.7	60.5±12.1	66.5±13.6	4

Where values are mean ± standard error of the mean

V_m: Membrane Potential

τ_{FI}: Time constant of closed-state fast inactivation at a given voltage

Table D.8. Time Constants of Open-State Fast Inactivation

Mutant	V _m	τ _{Fon} pH 7.4 (ms)	τ _{Fon} pH 7.0 (ms)	τ _{Fon} pH 6.0 (ms)	N
E1784A	-30 mV	2.08±0.13	2.37±0.19	3.12±0.38	9
	-10 mV	1.14±0.06	1.19±0.06	1.44±0.07	9
	+10 mV	0.91±0.06	0.90±0.06	1.05±0.08	9
	+30 mV	0.85±0.08	0.85±0.10	0.95±0.09	9
E1784D	-30 mV	1.84±0.18	1.95±0.17	2.88±0.15	7
	-10 mV	1.00±0.07	1.03±0.07	1.36±0.05	7
	+10 mV	0.79±0.06	0.80±0.05	0.98±0.08	7
	+30 mV	0.78±0.09	0.83±0.07	0.91±0.08	7
E1784E	-30 mV	1.95±0.07	2.02±0.08	3.08±0.14	8
	-10 mV	1.22±0.07	1.24±0.06	1.62±0.06	8
	+10 mV	0.99±0.07	1.02±0.07	1.28±0.09	8
	+30 mV	0.95±0.11	0.97±0.09	1.16±0.11	8
E1784K	-30 mV	1.16±0.18	1.36±0.19	1.54±0.22	4
	-10 mV	0.78±0.09	0.85±0.10	1.07±0.11	4
	+10 mV	0.67±0.09	0.72±0.08	0.77±0.10	4
	+30 mV	0.59±0.10	0.56±0.10	0.62±0.12	4
E1784Q	-30 mV	1.79±0.08	2.14±0.12	3.25±0.24	9
	-10 mV	0.99±0.06	1.09±0.05	1.64±0.07	9
	+10 mV	0.82±0.10	0.81±0.06	1.16±0.08	9
	+30 mV	0.54±0.05	0.61±0.06	0.98±0.25	6
E1784R	-30 mV	1.27±0.10	1.29±0.11	1.56±0.12	9
	-10 mV	0.83±0.06	0.84±0.06	1.07±0.07	9
	+10 mV	0.70±0.07	0.72±0.06	0.88±0.07	9
	+30 mV	0.74±0.07	0.73±0.09	0.78±0.12	8
E1784V	-30 mV	1.42±0.10	1.72±0.19	2.43±0.12	5
	-10 mV	0.79±0.05	0.82±0.06	1.08±0.07	5
	+10 mV	0.64±0.05	0.64±0.04	0.77±0.05	5
	+30 mV	0.58±0.05	0.60±0.05	0.66±0.07	5
E1784W	-30 mV	1.75±0.17	1.90±0.19	2.75±0.72	5
	-10 mV	1.10±0.07	1.13±0.06	1.42±0.08	5
	+10 mV	0.89±0.07	0.90±0.05	1.02±0.05	5
	+30 mV	0.77±0.08	0.80±0.07	1.05±0.19	5

Where values are mean ± standard error of the mean

V_m: Membrane Potential

τ_{Fon}: Time constant of open-state fast inactivation at a given voltage